UNIVERSIDADE FEDERAL DO CEARÁ

CENTRO DE TECNOLOGIA

DEPARTAMENTO DE ENGENHARIA DE TELEINFORMÁTICA

PROGRAMA DE PÓS-GRADUAÇÃO EM ENGENHARIA DE TELEINFORMÁTICA

DOUTORADO EM ENGENHARIA DE TELEINFORMÁTICA

MICHEL GONZAGA DOS SANTOS

A STUDY ON THE ANGLE-OF-ARRIVAL ESTIMATION PROBLEM FROM THREE COMPLEMENTARY PERSPECTIVES: CHALLENGES, PARTICULARITIES AND APPLICATIONS

FORTALEZA

2025

MICHEL GONZAGA DOS SANTOS

A STUDY ON THE ANGLE-OF-ARRIVAL ESTIMATION PROBLEM FROM THREE COMPLEMENTARY PERSPECTIVES: CHALLENGES, PARTICULARITIES AND APPLICATIONS

Tese apresentada ao Programa de Pós-Graduação em Engenharia de Teleinformática do Centro de Tecnologia da Universidade Federal do Ceará, como requisito parcial à obtenção do título de doutor em Engenharia de Teleinformática. Área de Concentração: Sinais e Sistemas

Orientador: Prof. Dr. Walter da Cruz Freitas Júnior

FORTALEZA

2025

MICHEL GONZAGA DOS SANTOS

A STUDY ON THE ANGLE-OF-ARRIVAL ESTIMATION PROBLEM FROM THREE COMPLEMENTARY PERSPECTIVES: CHALLENGES, PARTICULARITIES AND APPLICATIONS

Tese apresentada ao Programa de Pós-Graduação em Engenharia de Teleinformática do Centro de Tecnologia da Universidade Federal do Ceará, como requisito parcial à obtenção do título de doutor em Engenharia de Teleinformática. Área de Concentração: Sinais e Sistemas

Aprovada em: 19 de dezembro de 2025

BANCA EXAMINADORA

Prof. Dr. Walter da Cruz Freitas Júnior (Orientador)
Universidade Federal do Ceará (UFC)

Prof. Dr. João César Moura Mota
Universidade Federal do Ceará

Prof. Dr. Igor Moaco Guerreiro
Universidade Federal do Ceará

Prof. Dr. Yuri Carvalho Barbosa Silva
Universidade Federal do Ceará

Prof. Dr. Vicente Angelo de Sousa Junior
Universidade Federal do Rio Grande do Norte
(UFRN)

Prof. Dr. Renato Machado
Instituto Tecnológico da Aeronáutica

ACKNOWLEDGEMENTS

First, I would like to express my heartfelt gratitude to my wonderful wife for being by my side throughout the entire process of writing this thesis. Her unwavering support, patience, and encouragement sustained me through the most challenging moments. I know that this journey was not easy for me nor for her, and I deeply appreciate her compassion, understanding, and steadfast love.

I would also like to thank my parents and my sister for being by my side from the very beginning; without their constant support, my academic path thus far would not have been possible.

I would also like to extend my sincere gratitude to my supervisor, Prof. Dr. Walter da Cruz Freitas Júnior. We have been working together since my Bachelor's degree in Telecommunication Engineering, and throughout these years, I have learned a great deal from his guidance and expertise. His continuous support and trust were indispensable to the completion and success of this Ph.D. dissertation.

I would also like to express my gratitude to Prof. Dr. Rodrigo Cavalcanti, Prof. Dr. Igor Moáco Gueiro, Prof. Dr. Yuri Carvalho, and Prof. Dr. Walter Freitas for giving me the opportunity to join the GTEL team, where I have had the chance to actively cooperate in Ericsson's projects. Thanks to the partnership between GTEL and Ericsson, I had the opportunity to pursue a Sandwich Ph.D. in Sweden under the supervision of Dr. Eleftherios Karipidis and Prof. Dr. Gabor Fodor, to whom I would also like to extend my sincere gratitude. Furthermore, I would like to show my gratitude for the financial support provided by the Conselho Nacional de Desenvolvimento Científico e Tecnológico during this period.

I also extend my acknowledgments to Prof. Dr. João César Moura Mota for his friendship and for supporting me throughout my academic path so far. Our interactions were invaluable and indispensable to my success during this PhD.

I could never forget the contribution of my brilliant colleagues from GTEL. Our valuable interactions have directly and indirectly contributed to this accomplishment.

Finally, I acknowledge the technical and financial support from FUNCAP and Ericsson Research, Sweden, and Ericsson Innovation Center, Brazil, under UFC.49, UFC.50 and UFC.52 Technical Cooperation Contracts Ericsson/UFC. Also, this study was financed in part by the Coordenação de Aperfeiçoamento de Pessoal de Nível Superior - Brasil (CAPES) - Finance Code 001.

"For if anyone thinks he is something, when he is nothing, he deceives himself."

(Galatians 6:3)

RESUMO

Esta tese de doutorado condensa os resultados dos estudos desenvolvidos ao longo deste programa de doutorado. Ela inicia com um capítulo introdutório, que apresenta o embasamento teórico necessário para sustentar os tópicos abordados ao longo do trabalho. Os demais capítulos estão interligados por meio do tema central desta tese: o problema de estimação do ângulo de chegada (AoA) em sistemas sem fio, o qual é explorado sob três perspectivas distintas, porém complementares. A principal motivação para a elaboração deste documento é sustentar o argumento de que uma compreensão clara do problema de estimação do AoA é um elemento-chave para o avanço das tecnologias previstas para a sexta geração (6G) e além, ao estabelecer uma ponte entre os domínios de comunicação e sensoriamento por radar. Nesse sentido, adquirir uma compreensão aprofundada das nuances desse problema é de grande importância, pois fornece a base para a plena exploração do potencial de ambos os serviços. Primeiramente, o problema é analisado sob uma perspectiva puramente comunicacional, na qual é proposta uma nova abordagem de estimação de AoA para o refinamento de feixes analógicos, explorando o domínio da polarização em redes de comunicação multiple-input multiple-output (MIMO) operando em altas frequências. Em seguida, o problema de estimação conjunta do AoA e frequência Doppler é investigado sob a ótica do sensoriamento. Ao considerar redes de sensoriamento biestáticas e multiestáticas, a estimação desses dois parâmetros permite capacidades de localização de alvos dentro do sistema. Nesse contexto, o Cramér-Rao lower bound (CRLB) é empregado para avaliar o desempenho dos estimadores individuais em diferentes configurações de cenário. Por fim, o problema de estimação de AoA e ângulo de partida (AoD) é examinado em uma rede biestática de sensoriamento e comunicação integrados (ISAC). Assumindo transmissão em downlink, argumenta-se que a qualidade de serviço (QoS) dos sistemas de comunicação e sensoriamento pode ser aprimorada por meio de uma alocação adequada de recursos espaço–temporais. Para esse fim, é formulado um problema de otimização com o objetivo de melhorar conjuntamente a taxa de soma média no tempo—considerando um determinado número de usuários (UEs)—e o CRLB associado ao AoA e ao AoD do alvo passivo de interesse. Além disso, as principais conclusões a cerca dos capítulos anteriores, bem como perspectivas para trabalhos futuros, são apresentadas no capítulo de conclusão.

Palavras-chave: Teoria da Estimação. MIMO. CRLB. ISAC. Sensoriamento. Comunicação

ABSTRACT

This PhD dissertation condenses the outcomes of the studies developed over the course of this doctoral program. It begins with an overview chapter that provides the theoretical background required to support the topics addressed throughout the thesis. The remaining chapters are connected through the central theme of this thesis: the angle of arrival (AoA) estimation problem in wireless systems, which is explored under three distinct yet complementary perspectives. The main motivation for writing this document is to support the argument that a clear understanding of the AoA estimation problem is a key enabler for advancing the technologies envisioned for 6th generation (6G) and beyond, by bridging the communication and radar sensing domains. Accordingly, gaining insight into the nuances of this problem is of great importance, as it provides the foundation for fully exploiting the potential of both services. First, the problem is examined from a purely communication perspective, in which a novel AoA estimation approach for analog beam refinement is proposed, exploiting the polarization domain in high-frequency multiple-input multiple-output (MIMO) communication networks. Subsequently, the joint AoA and Doppler frequency estimation problem is investigated from a sensing perspective. By considering bistatic and multistatic sensing networks, the joint estimation of these two parameters enables target localization capabilities within the system. In this context, the Cramér-Rao lower bound (CRLB) is employed to assess the performance of the individual estimators under different scenario setups. Finally, the AoA and angle of departure (AoD) estimation problem is examined in a bistatic integrated communication and sensing (ISAC) network. Assuming downlink transmission, it is argued that the quality-of-service (QoS) of both sensing and communication systems can be improved through a proper allocation of space–time resources. To this end, an optimization problem is formulated to jointly enhance the time-averaged communication sum-rate—assuming a given number of users (UEs)—and the CRLB associated with the AoA and AoD of the passive target of interest. Additionally, the main conclusions derived from these chapters, along with directions for future research, are summarized in the Conclusion chapter.

Keywords: Estimation Theory. MIMO. CRLB. ISAC. Sensing. Communication.

LIST OF FIGURES

LIST OF TABLES

LIST OF ACRONYMS

1G	1st generation
3G	3rd generation
4G	4th generation
5G	5th generation
6G	6th generation
AoA	angle of arrival
AoD	angle of departure
AP	access point
AWGN	additive Gaussian noise
BM	beam management
BPL	beam pair link
BSP	beam sweeping
CDF	cumulative distribution function
CPU	central processing unit
CRLB	Cramér-Rao lower bound
D-MIMO	distributed MIMO
DFT	discrete Fourier transform
DP-ViSA	dual-polarization virtual sub-array based AoA
emBB	enhanced mobile broadband
FIM	Fisher information matrix
GCS	global coordinate system
IID	independent and identically distributed
ISAC	integrated communication and sensing
JRC	joint radar and communication
KPI	key performance indicator
L1	layer 1
LCS	local coordinate system
LOS	line-of-sight
MIMO	multiple-input multiple-output
ML	maximum likelihood
mMTC	massive machine-type communications

mmWave	millimeter-wave
MVU	minimum variance unbiased
OFDM	orthogonal frequency division multiplexing
OFDMA	orthogonal frequency division multiple access
PDF	probability density function
QoS	quality-of-service
RCS	radar cross section
RF	radio-frequency
RS	reference signal
RSRP	reference signal received power
Rx	receiver
SINR	signal-to-interference-plus-noise ratio
SISO	single-input single-output
SLSQP	sequential linear-quadratic programming
SNR	signal-to-noise ratio
SSS	strict sense stationary
TDM	time division multiplexing
ToA	time of arrival
TSSA	target sensing service area
Tx	transmitter
UE	user
ULA	uniform linear array
URA	uniform rectangular array
URLLC	ultra-reliable low-latency communications
ViSA	virtual sub-array based AoA
WSS	wide sense stationary
ZF	zero-forcing

LIST OF SYMBOLS

$(.)^*$	Complex conjugate operator
$(.)^H$	Hermitian operator
$(.)^h$	Transpose operator
$\mathbb{E}\{.\}$	Expected value
μ	Mean
σ	Standard deviation
σ^2	Variance
$\int$	Integral
$f_X(x)$	Probability density function
$F_X(x)$	Cumulative density function
$p_{\mathbf{y}}(\mathbf{y};\theta)$	Likelihood function
$\frac{\partial}{\partial x}$	Partial derivative
$\mathbf{I}$	Indentity matrix
c	Speed of light
f_c	Carrier frequency
P_{Tx}	Transmit power
t	time
λ	Wave length
∞	Infinity

SUMMARY

1 GENERAL OVERVIEW

The ability to access the internet from mobile devices is one of the marks of the 3rd generation (3G) networks, and it enabled the rapid rise of social media platforms and streaming services. However, as data consumption increased, the network eventually became insufficient to handle the growing demand for these services. This limitation motivated the development of 4th generation (4G) (DAHLMAN *et al.*, 2010; DAHLMAN *et al.*, 2013), which was introduced in the 2010s. 4G was designed to exploit larger bandwidths, operate across multiple frequency bands, and integrate multi-antenna technologies from the outset to enhance capacity and reliability. Furthermore, 4G introduced the concept of orthogonal frequency division multiple access (OFDMA) (JIANG *et al.*, 2010), an evolution of traditional orthogonal frequency division multiplexing (OFDM) that enables the simultaneous transmission to multiple users, with their symbols multiplexed in the frequency domain over distinct subsets of orthogonal subcarriers.

Nowadays, society has been deeply impacted by the advent of 5th generation (5G) (SHAYEA *et al.*, 2020; BUZZI *et al.*, 2016). This generation not only enhanced the capabilities of services provided by its predecessors but also paved the way for emerging applications such as autonomous driving, cloud gaming, and augmented reality. The three main pillars of 5G are:

- **Enhanced mobile broadband (emBB)**, which supports high-throughput applications such as UHD video streaming and immersive XR experiences;
- **Massive machine-type communications (mMTC)**, which enables massive Internet of Things (IoT) deployments with billions of low-power devices;
- **Ultra-reliable low-latency communications (URLLC)**, which provides ultra-reliable, low-latency communication for critical applications such as remote surgery and industrial automation.

The release of 6G (TATARIA *et al.*, 2021; WANG *et al.*, 2023; JIANG *et al.*, 2024), which is expected to be commercially deployed in the early 2030s, has sparked intense discussion and motivated significant research efforts across industry and academia. Ever since 5G, there has been a growing interest in integrating sensing capabilities into communication systems—an interest further amplified by the rapid expansion of the Internet of Things (IoT), (GUO *et al.*, 2021). Traditional services such as voice, text, and mobile broadband no longer constitute the sole focus; instead, networks are envisioned to support a much broader range of applications.

Furthermore, 6G is expected to mark a paradigm shift from cellular architectures toward user-centric network designs, (DRAMPALOU *et al.*, 2024).

In this context, ISAC (LU *et al.*, 2024; LUO *et al.*, 2025) has emerged as a promising technology that has attracted increasing attention from both academia and industry. Its primary goal is to exploit the hardware commonalities between communication and radar systems to merge them within a single network architecture. This integration opens the door to novel services. For example, a base station can simultaneously serve a user (UE) while sensing the surrounding environment to detect targets of interest (LIU *et al.*, 2022), estimate their positions (JABEEN *et al.*, 2025), and even reconstruct images from the sensing results. Such capabilities can support a wide range of applications, including assisting autonomous driving systems, enhancing security and surveillance in specific areas, and enabling many other context-aware services.

1.1 Background on Statistics and Estimation Theory

This section presents a theoretical background on statistics and estimation theory necessary to support the developments of this work. A solid understanding of the underlying mathematical and statistical concepts is essential, as they form the basis for the contributions of this PhD dissertation. The section begins with a discussion on random variables, introducing the concepts of probability density function (PDF) and cumulative distribution function (CDF) (PARZEN, 1962; KOBAYASHI *et al.*, 2011), as well as key statistical moments such as expected value and variance, along with relevant operations. The discussion then extends these concepts to random processes, providing the foundation for time-varying models. In the sequence, key elements of classical estimation theory are reviewed, emphasizing results that are fundamental for performance analysis.

1.1.1 Random Variable

In the context of classical estimation theory, it is essential to first introduce the concept of random variables. According to (PAPOULIS, 1965), a random variable can be defined as:

> An **RV** x is a process of assigning a number $x(\zeta)$ to every outcome ζ. The resulting function must satisfy the following two conditions but is otherwise arbitrary:
>
> I. The set $\{x \leq \xi\}$ is an event for every x.

II. The probabilities of the events $\{x = +\infty\}$ and $\{x = -\infty\}$ equal 0:
$P(x = +\infty) = 0, \quad P(x = -\infty) = 0.$

This definition can be further extended to complex variables by making usage of the property that states that the sum of two random variables is itself a random variable. Random variables can be further classified as continuous and discrete depending on the nature of the data. For convenience, we decided to describe the theory of random variables regarding continuous-valued ones, but at this point, it should be pointed out that the properties and definitions in the sequence can be easily extended to discrete-valued random variables, without loss of generality.

After introducing the concept of random variables, our next goal is to identify patterns that enhance our understanding of them. A crucial step in this direction is defining the concept CDF, (PARZEN, 1962).

Definition 1.1.1. *Consider a random variable X, and let x be an arbitrary element of the set containing all the possible values of the sample space, $\mathscr{S}$, of a given experiment, $\mathscr{E}$. We define the CDF as the probability of $X \leq x$,*

$$F_X(x) \triangleq Pr(X \leq x). \tag{1.1}$$

for all $x \in \mathscr{S}$.

Moreover, by taking the first derivative of the CDF with respect to x, we obtained the so-called PDF. Notice, therefore, that there is a duality relationship between the PDF and the CDF, as described in (1.2).

$$\begin{aligned} F_X(x) &= \int_{-\infty}^{x} f_X(t)dt, \\ f_X(x) &\triangleq \frac{d}{dx}F(x). \end{aligned} \tag{1.2}$$

Hence, from Equations (1.1) and (1.2), it is evident that the probability of a random variable assuming a value within a subset of the sample space can be calculated using the PDF. This relationship is detailed in Equation (1.3).

$$\begin{aligned} Pr(x_1 \leq X \leq x_2) &= Pr(X \leq x_2) - Pr(X \leq x_1) \\ &= F_X(x_2) - F_X(x_1) = \int_{x_1}^{x_2} f_X(x)dx. \end{aligned} \tag{1.3}$$

Let $\mathscr{S}$ denote the sample space of a given experiment, and let X be a random variable with PDF $f_X(x)$, where $x \in \mathscr{S}$. From the discussion in the previous paragraph, the probability of

an event can be computed directly from the PDF. Therefore, it is possible to generalize several fundamental properties of probability to the PDF. In this context, some of the most important properties are summarized below.

Property 1. *Non-negativity*:

Since the CDF is a non-decreasing function, its derivative, the PDF, is always non-negative. Therefore, for all $x \in \mathscr{S}$:

$$f_X(x) \geq 0. \tag{1.4}$$

Property 2. *Total area*:

The total area under the PDF must be equal to 1, since the random variable X must take on some value in the sample space $\mathscr{S}$. Therefore:

$$\int_{\mathscr{S}} f_X(x)dx = 1. \tag{1.5}$$

Alternatively, one may be interested in evaluating the probability that two events A and B occur simultaneously. Let $P(A,B)$ denote the joint probability of events A and B, corresponding to the probability of their intersection. From our previous discussion on the relationship between probability and the PDF, it follows that $P(A,B)$ can be expressed in terms of a joint PDF. In this context, let $\mathscr{S}$ denote the sample space, and let X and Y be two random variables with joint PDF $f_{X,Y}(x,y)$, where $x,y \in \mathscr{S}$. The joint PDF satisfies the following fundamental properties:

Property 1.1. *Marginal PDFs: The marginal PDF of X, denoted by $f_X(x)$, is obtained by integrating the joint PDF $f_{X,Y}(x,y)$ with respect to y over its entire support. Similarly, the marginal PDF of Y, $f_Y(y)$, is obtained by integrating with respect to x:*

$$\begin{aligned} f_X(x) &= \int_{-\infty}^{\infty} f_{X,Y}(x,y)\,dy, \\ f_Y(y) &= \int_{-\infty}^{\infty} f_{X,Y}(x,y)\,dx. \end{aligned} \tag{1.6}$$

Property 1.2. *Joint probability: The probability that $X \geq x$ and $Y \geq y$ can be obtained by integrating the joint PDF over the corresponding region:*

$$P(X \geq x, Y \geq y) = \int_{-\infty}^{x}\int_{-\infty}^{y} f_{X,Y}(x,y)dxdy \tag{1.7}$$

Another scenario of interest arises when one wishes to evaluate the probability of an event A given that event B has occurred. In this case, one is interested in the conditional

probability $P(A|B)$. According to Bayes' theorem, the conditional probability $P(A|B)$ is related to the joint probability $P(A,B)$ and the probability of event B, $P(B)$, as

$$P(A|B) = \frac{P(A,B)}{P(B)}. \tag{1.8}$$

As expected, this theorem can be extended to conditional PDFs, such that given two two random variables X and Y with conditional PDFs $f_{X|Y}(x|y)$ and $f_{Y|X}(y|x)$, where $x, y \in \mathscr{S}$, the theorem becomes,

$$\begin{aligned} f_{X|Y}(x|y) &= \frac{f_{X,Y}(x,y)}{f_Y(y)}, \\ f_{Y|X}(y|x) &= \frac{f_{Y,X}(y,x)}{f_X(x)}. \end{aligned} \tag{1.9}$$

Moving forward in the discussion on random variables, it is essential to introduce two of their most fundamental statistical moments: the mean and the variance (PAPOULIS, 1965). Before doing so, it is useful to clarify the general concept of statistical moments. Moments can be interpreted as characteristic descriptors, or *fingerprints*, of a probability distribution. In fact, given a sufficient number of moments, it is possible to fully characterize its PDF.

The mean μ, also referred to as the expected value, of a random variable is a measure of the central tendency of its distribution, representing the value around which the PDF is most concentrated. Given a random variable X with PDF $f_X(x)$, its mean is formally defined using the expectation operator $\mathbb{E}\{.\}$, as follows:

Definition 1.1.2. *Let X be a random variable with PDF $f_X(x)$. The expected value of X, denoted by μ, is given by*

$$\mu = \mathbb{E}\{X\} = \int_{\mathscr{S}} x f_X(x)\, dx, \tag{1.10}$$

where $\mathscr{S}$ denotes the support (or sample space) of the random variable X. Note that although the density function $f_X(x)$ must be non-negative for all $x \in \mathscr{S}$, the variable x itself may assume either positive or negative values, depending on the domain specified by $\mathscr{S}$.

In this context, it is important to briefly discuss some fundamental properties of the expectation operator $\mathbb{E}\{X\}$. This chapter considers the following properties:

Property 1.3. *The mean of a Constant: Let X be a random variable with PDF $f_X(x)$ and c a constant, it follows that*

$$\mathbb{E}\{c\} = \int_{\mathscr{S}} c f_X(x) dx = c. \tag{1.11}$$

Proof.

$$\mathbb{E}\{c\} = \int_{\mathscr{S}} c f_X(x)dx = c\int_{\mathscr{S}} f_X(x)dx = c. \tag{1.12}$$

Property 1.4.

Sum of Random Variables:

Let $\{X_1, X_2, \ldots X_N\}$ be a set of N random variables, and let $f_{X_0,X_2,\ldots X_N}(x_1, x_2, \ldots x_N)$ be the joint PDF for this set, it follows that

$$\mathbb{E}\left\{\sum_{n=1}^{N} X_n\right\} = \sum_{n=1}^{N} \mathbb{E}\left\{X_n\right\}. \tag{1.13}$$

Proof.

Let $\mathscr{S} = \{\mathscr{S}_1, \mathscr{S}_2, \ldots, \mathscr{S}_N\}$ be the joint sample space, such that

$$\begin{aligned}
\mathbb{E}\left\{\sum_{n=1}^{N} X_n\right\} &= \int_{\mathscr{S}} \left(\sum_{n=1}^{N} x_n\right) f_{X_1,X_2,\ldots,X_N}(x_1, x_2, \ldots, x_N)\, d\mathbf{x} \\
&= \sum_{n=1}^{N} \int_{\mathscr{S}_n} x_n \left(\int_{\mathscr{S}\setminus\mathscr{S}_n} f_{X_1,X_2,\ldots,X_N}(x_1, x_2, \ldots, x_N)\, d\mathbf{x}'\right) dx_n \\
&= \sum_{n=1}^{N} \mathbb{E}\{X_n\}.
\end{aligned} \tag{1.14}$$

Property 1.5. *Multiplication by a Constant:*

Let X be a random variable with a PDF $f_X(x)$, and a constant c, it follows that

$$\mathbb{E}\{cX\} = c\mathbb{E}\{X\}. \tag{1.15}$$

Proof.

$$\begin{aligned}
\mathbb{E}\left\{cX\right\} &= \int_{\mathscr{S}} cx f_X(x)dx = c\int_{\mathscr{S}} x f_X(x)dx \\
&= c\mathbb{E}\{X\}.
\end{aligned} \tag{1.16}$$

The variance σ^2 of a random variable X with PDF $f_X(x)$ is a measure of dispersion, quantifying how far the values of X are spread around their mean μ. The more concentrated the distribution is around its mean, the smaller its variance σ^2 will be. The variance is also calculated using $\mathbb{E}\{.\}$ but it also depends on the previous knowledge of μ, as it is formally defined below:

Definition 1.1.3. *Let X be a random variable with PDF $f_X(x)$. The variance of X, denoted by σ^2, is given by*

$$\sigma^2 = \mathbb{E}(X - \mathbb{E}\{X\})^2 = \int_{\mathscr{S}} (x - \mathbb{E}\{X\})^2 f_X(x)dx. \tag{1.17}$$

where $\mathscr{S}$ denotes the support (or sample space) of the random variable X.

Note that these statistical moments can be naturally extended to joint and conditional distributions. Since this generalization is straightforward, it will not be discussed in detail in this document.

The properties and definitions discussed above were initially presented for scalar random variables. However, these concepts can be extended to vector-valued random variables and, more generally, to higher-dimensional arrays. To introduce this generalization, we focus on the case of random vectors, since the extension to higher-dimensional arrays follows naturally.

Let $\mathscr{X}$ be a set of N identically distributed random variables $\{x_1,\ldots,x_N\}$ arranged into the random vector $\mathbf{x}\in\mathbb{C}^{N\times 1}$. The PDF of the random vector $\mathbf{x}$, denoted by $f_{\mathbf{X}}(\mathbf{x})$, is defined as the joint PDF of its entries:

$$f_{\mathbf{X}}(\mathbf{x}) = f_{X_1,X_2,\ldots,X_N}(x_1,x_2,\ldots,x_N). \tag{1.18}$$

As expected, the PDF of a random vector satisfies the same fundamental properties as the PDF of a scalar random variable. Some of the most relevant properties are summarized below.

Property 1.6. *Non-negativity: Since de CDF is always non-negative, it follows that*

$$f_{\mathbf{X}}(\mathbf{x}) \geq 0. \tag{1.19}$$

Property 1.7. *Total area:*
If we integrate $f_{\mathbf{X}}(\mathbf{x})$ over $\mathscr{S}$, the result must be equal to 1*,*

$$\int_{\mathscr{S}} f_{\mathbf{X}}(\mathbf{x})d\mathbf{x} = 1. \tag{1.20}$$

Let $\mathbf{x}\in\mathbb{C}^{N\times 1}$ be a random vector with PDF $f_{\mathbf{X}}(\mathbf{x})$, where $x_i\in\mathscr{S}$ for $i=1,\ldots,N$. The concept of statistical moments can be naturally extended. In particular, the mean vector $\mu_{\mathbf{X}}$ is a direct generalization of the mean of a scalar random variable and is defined as,

$$\mu_{\mathbf{X}} = \mathbb{E}\{\mathbf{X}\} = \int_{\mathscr{S}} \mathbf{x}\, f_{\mathbf{X}}(\mathbf{x})\, d\mathbf{x} = \begin{bmatrix} \mathbb{E}\{X_1\} \\ \mathbb{E}\{X_2\} \\ \vdots \\ \mathbb{E}\{X_N\} \end{bmatrix}. \tag{1.21}$$

Furthermore, the covariance matrix $\mathbf{C}_{\mathbf{X}}$ is the multivariate counterpart of the variance for random vectors. It is formally defined as

$$\mathbf{C}_{\mathbf{X}} = \mathbb{E}\left[(\mathbf{X}-\mu_{\mathbf{X}})(\mathbf{X}-\mu_{\mathbf{X}})^T\right], \tag{1.22}$$

where $\mu_{\mathbf{X}} = \mathbb{E}\{\mathbf{X}\}$ is the mean vector and $(\cdot)^T$ denotes the transpose operator.

Random variables can be described according to their PDF and CDF. In this context, a random variable is said to follow a probability distribution described by a PDF $f_X(x)$. This chapter introduces two important examples: the uniform distribution (TEZUKA, 2012) and the normal distribution (PATEL; READ, 1996), which will be discussed in detail below.

The uniform distribution assumes that each outcome in the sample space is equally likely, which implies that the probability of observing any specific outcome is the same for every element in the sample space. Consider a uniform random variable $X \sim \mathscr{U}(a,b)$, such that $f_X(x) = c$ for $a \leq x \leq b$.

To determine the value of c, we use the fact that the total probability must equal 1:

$$\begin{aligned} \int_{-\infty}^{\infty} f_X(t)\,dt &= \int_a^b c\,dt = 1, \\ &= ct\big|_a^b = c(b-a) = 1, \\ \Rightarrow \quad c &= \frac{1}{b-a}. \end{aligned} \tag{1.23}$$

Thus, the PDF of a uniform random variable can be expressed as

$$f_X(x) = \begin{cases} \dfrac{1}{b-a}, & a \leq x \leq b, \\ 0, & \text{otherwise.} \end{cases} \tag{1.24}$$

Figure 1 depicts a graphical representation of this PDF.

As a consequence, the CDF of the uniform distribution can be calculated as follows,

$$\begin{aligned} F(x) &= \int_{-\infty}^{x} \frac{1}{b-a}dt = \int_a^x \frac{1}{b-a}dt \\ &= \frac{t}{b-a}\bigg|_a^x = \begin{cases} 0, & x < a \\ \frac{x-a}{b-a}, & a \leq x \leq b \\ 1, & x > b \end{cases}. \end{aligned} \tag{1.25}$$

As expected, since its PDF is constant within the closed interval $[a,b]$, the corresponding CDF is a linear function of x with positive slope in this interval, as illustrated in Figure 2.

The normal distribution, also referred to as the Gaussian distribution, is one of the most important probability distributions, with widespread applications across numerous fields. For example, it is often used to model noise in communication systems. In this context, consider a normal random variable $X \sim \mathscr{N}(\mu, \sigma^2)$. Its PDF is given by

$$f_X(x) = \frac{1}{\sqrt{2\pi\sigma^2}} \exp\left(-\frac{(x-\mu)^2}{2\sigma^2}\right). \tag{1.26}$$

Figura 1 – PDF of a uniform random variable, where $a = 1$ and $b = 3$

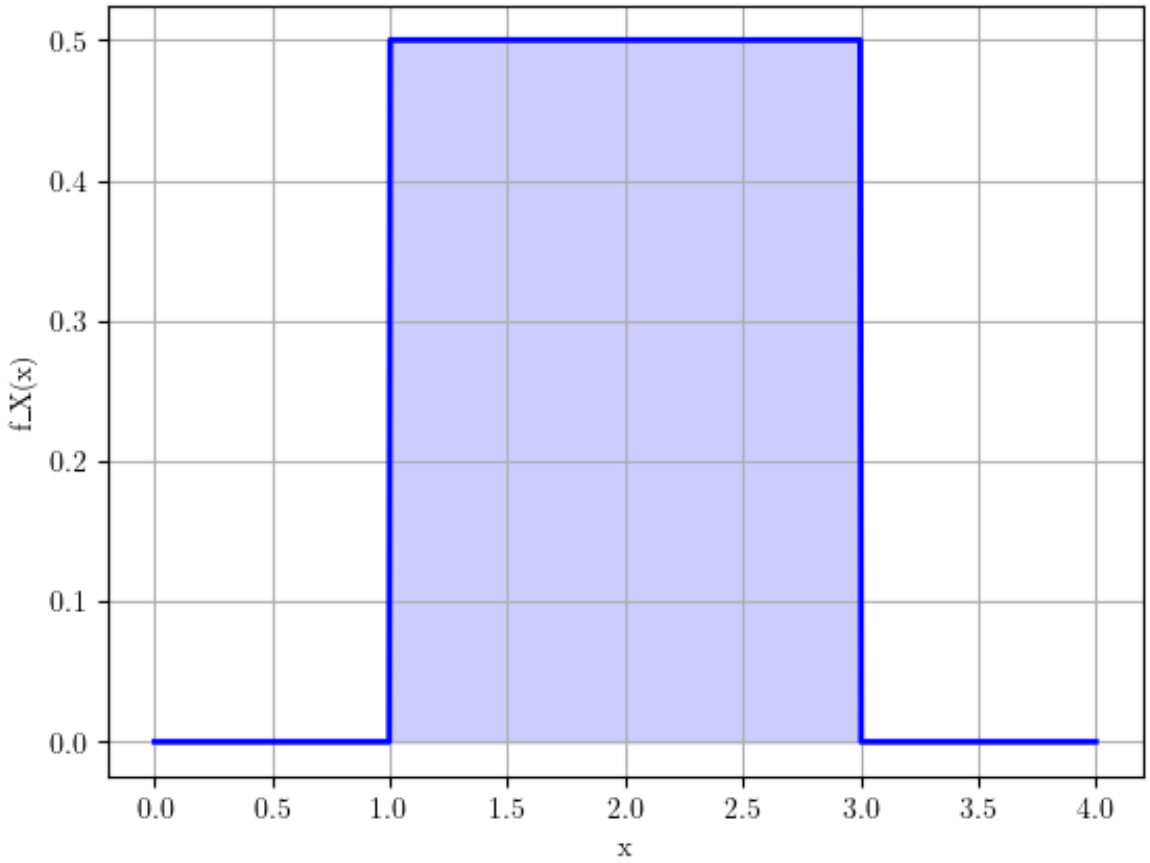

Source: Made by the author.

where, μ and σ^2 are the mean and variance of this random variable. Figure 3 illustrates the shape of this PDF. In this example, a zero-mean normal random variable is assumed, without loss of generality. Note that the distribution is symmetric around its mean, and the width of the peak is determined by its variance.

Moreover, from (1.26), it is easy to see that the calculation of the CDF is not straightforward, since the integral in (1.27)

$$F(x) = \int_{-\infty}^{x} \frac{1}{\sqrt{2\pi\sigma^2}} \exp\left(-\frac{(t-\mu)^2}{2\sigma^2}\right) dt, \tag{1.27}$$

cannot be solved analytically. However, it can be expressed in terms of the error function erf$(\cdot)$,

Figura 2 – CDF of a uniform random variable, where $a = 1$ and $b = 3$

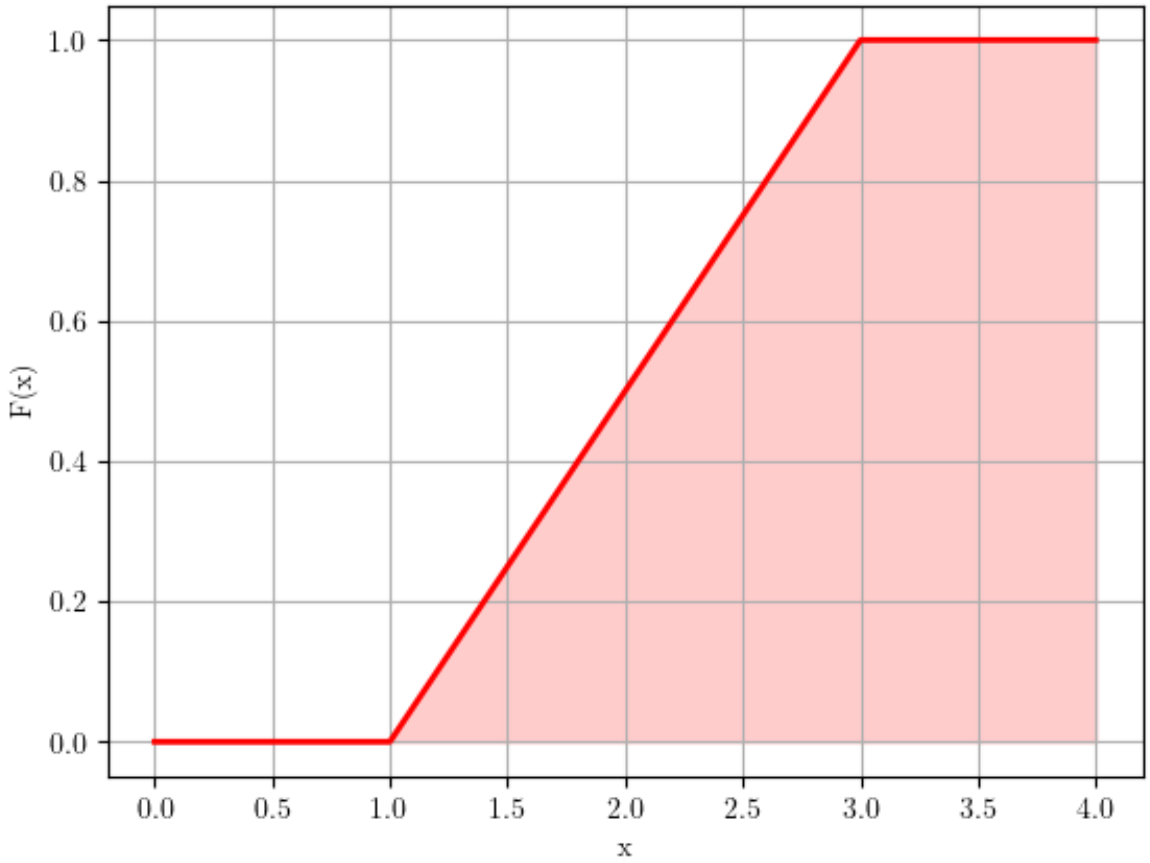

Source: Made by the author.

as shown in (1.28).

$$
\begin{aligned}
F(x) &= \int_{-\infty}^{x} \frac{1}{\sqrt{2\pi\sigma^2}} e^{-\frac{(t-\mu)^2}{2\sigma^2}} dt = \int_{-\infty}^{\frac{x-\mu}{2\sigma}} \frac{1}{\sqrt{\pi}} e^{-\frac{z^2}{2}} dz \\
&= \int_{-\infty}^{0} \frac{1}{\sqrt{\pi}} e^{-\frac{z^2}{2}} dz + \int_{0}^{\frac{x-\mu}{2\sigma}} \frac{1}{\sqrt{\pi}} e^{-\frac{z^2}{2}} dz \\
&= \frac{1}{2} + \int_{0}^{\frac{x-\mu}{2\sigma}} \frac{1}{\sqrt{\pi}} e^{-\frac{z^2}{2}} dz \\
&= \frac{1}{2} \left(1 + \frac{2}{\sqrt{\pi}} \int_{0}^{\frac{x-\mu}{2\sigma}} e^{-\frac{z^2}{2}} dz \right) \\
&= \frac{1}{2} \left(1 + err\left(\frac{x-\mu}{2\sigma} \right) \right).
\end{aligned}
\tag{1.28}
$$

The shape of this CDF resembles that of a hyperbolic tangent function, and also bears similarity to the CDF of a uniform random variable, but with smoother variations, as it can be seen from Figure 4.

The aforementioned discussion was conducted assuming continuous random variables, but it can also be readily extended to discrete random variables. From this point onward, we focus on discrete random variables due to their importance in digital communications, where

Figura 3 – PDF of a normal random variable, where $a = 1$ and $b = 3$

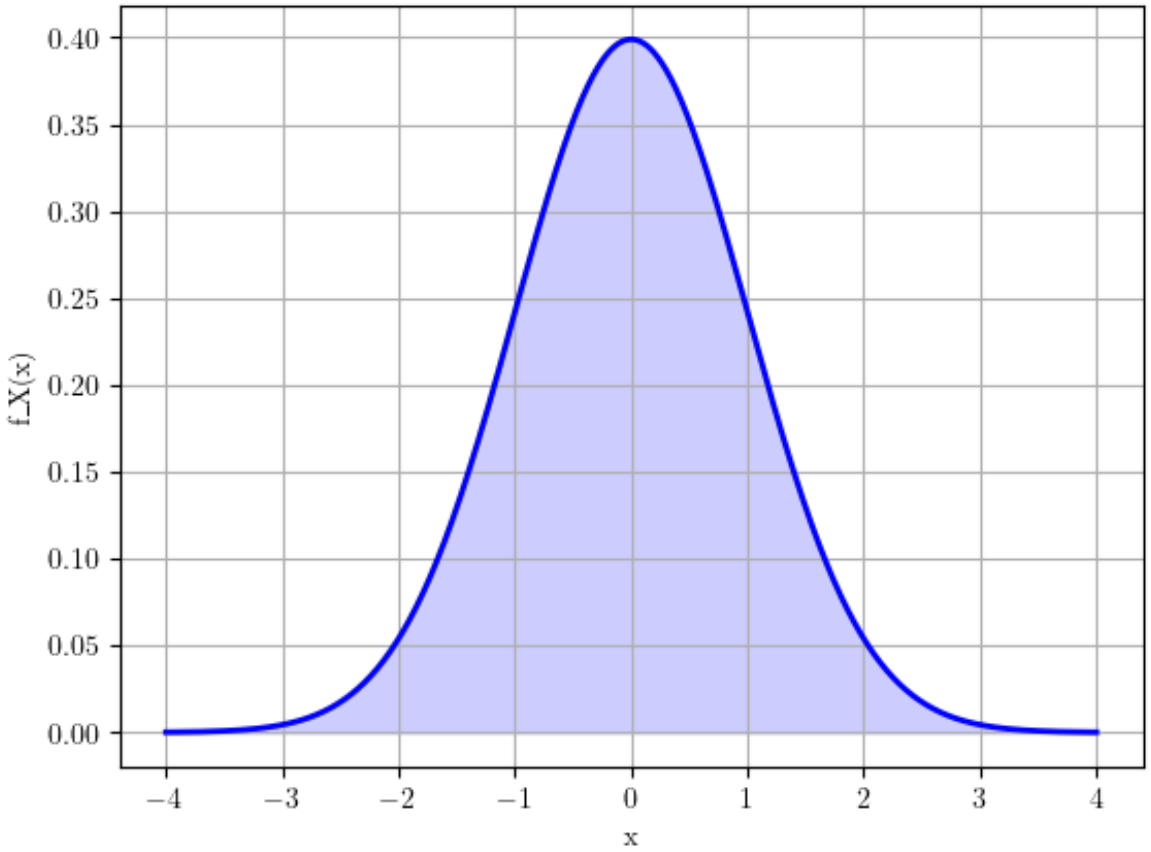

Source: Made by the author.

systems operate with discretized measurements of continuous signals in real-world applications.

1.1.2 Random Process

The previous subsection introduced the concept of random variables, providing the necessary background for the understanding of random processes (CRAMÉR; LEADBETTER, 2013). In summary, a random process extends this concept by incorporating time dependence. It is important to emphasize that this dependence is not deterministic, but rather random in nature. In essence, a random process produces a random value at each time instant, according to a given probability distribution.

Therefore, a discrete-time random process can be defined as the collection of time samples

$$x = \{x[n] : n \in \mathbb{Z}_{\geq 0}\},$$

where each $x[n]$ is a random variable. Equivalently, in continuous time, a random process can be

Figura 4 – CDF of a normal random variable, where $a = 1$ and $b = 3$

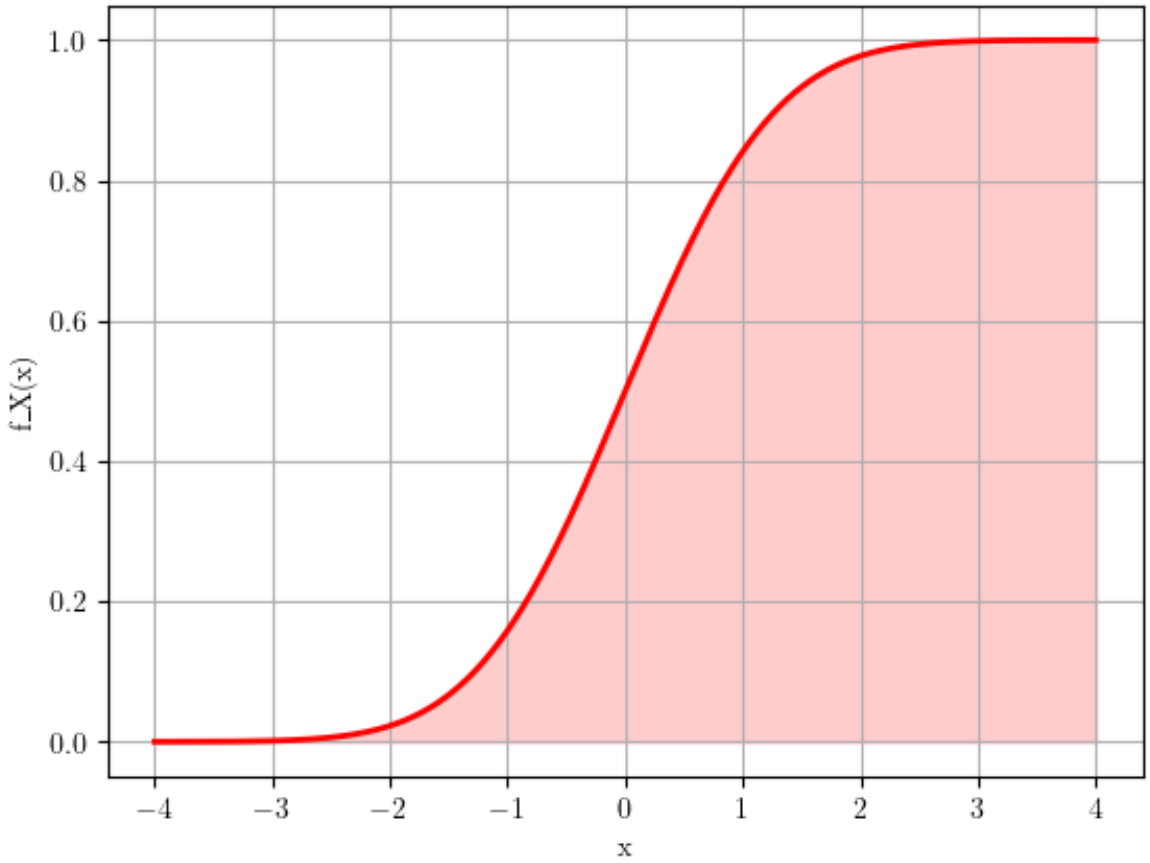

Source: Made by the author.

written as

$$x = \{x(t) : t \geq 0\},$$

with $x(t)$ being a random variable at each time instant t. A graphical illustration of a random process is provided in Figure 5.

Random processes are particularly useful for modeling physical phenomena that are inherently random. For example, voice signals can be modeled as random processes. However, their applications are not restricted to physical phenomena; in financial markets, for example, the historical variations of asset prices can also be represented by random processes.

In this context, stationarity (ROZANOV, 1963; HIDA, 2015) is one of the most fundamental concepts in the theory of random processes, and it will be formally defined in terms of strict sense stationary (SSS) and wide sense stationary (WSS) random processes. As the name suggests, the conditions required to classify a random process as SSS are more restrictive than those for WSS.

Definition 1.1.4. $x = \{x[n] : n \geq 0\}$ *is said to be an SSS, or strongly stationary process, if for all*

Figura 5 – Graphical representation of a random process

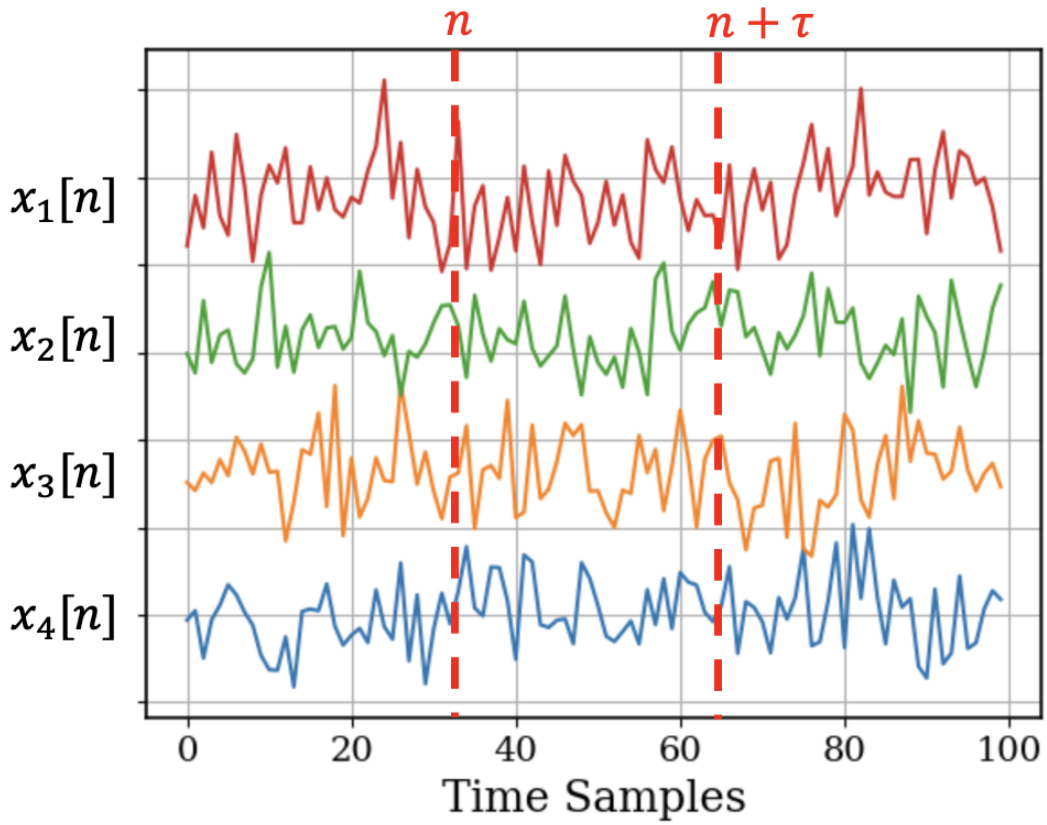

Source: Made by the author.

$n_1, n_2, \ldots n_N$ *and* τ

$$\{x[n_1], x[n_2], \ldots x[n_N]\} \text{ and } \{x[n_1+\tau], x[n_2+\tau], \ldots x[n_N+\tau]\}. \tag{1.29}$$

have the same joint distribution.

In real-world applications, it is often difficult, if not impractical, to ensure that all time measurements of a phenomenon modeled as a random process have the same joint distribution. Due to the complexity inherent in the definition of SSS random processes, this requirement is typically relaxed, giving rise to the concept of WSS random processes.

Definition 1.1.5. *A discrete-time random process* $x = \{x[n] : n \geq 0\}$ *is said to be WSS (wide-sense stationary), or weakly stationary, if the following conditions hold for all* n_1, n_2 *and for any time shift* τ*:*

1. *The mean is constant (independent of n):*

$$\mathbb{E}\{x[n_1]\} = \mathbb{E}\{x[n_2]\} = \mu_x. \tag{1.30}$$

2. *The autocorrelation depends only on the time difference (lag):*

$$R_{xx}[n_1, n_2] = \mathbb{E}\{x[n_1]x[n_2]\} = \mathbb{E}\{x[n_1+\tau]x[n_2+\tau]\}. \tag{1.31}$$

Until now, the concept of autocorrelation has not been formally defined. Therefore, a definition is provided below.

Definition 1.1.6. *Given a random process $x = \{x[n] : n \geq 0\}$, the autocorrelation function is defined as*

$$R_{xx}(n, n-\tau) = \mathbb{E}\{x[n]\, x[n-\tau]\}, \tag{1.32}$$

where τ denotes the time shift (or lag) between two samples of the process.

In the special case where $\{x[n]\}$ is composed of independent and identically distributed (IID) random variables, the joint PDF factorizes as

$$f_x(x[n], x[n-\tau]) = f_x(x[n])\, f_x(x[n-\tau]), \tag{1.33}$$

which implies that

$$R_{xx}(\tau) = \mathbb{E}\{x[n]\}\, \mathbb{E}\{x[n-\tau]\}. \tag{1.34}$$

The *cross-correlation function* extends this concept to measure the statistical similarity between two distinct random processes. Let $x = \{x[n]\}$ and $y = \{y[n]\}$ be two random processes. Their cross-correlation is defined as

$$R_{xy}(\tau) = \mathbb{E}\{x[n]\, y[n-\tau]\}. \tag{1.35}$$

1.1.3 Estimation Theory

This subsection introduces some of the fundamental concepts of estimation theory (KAY, 1993; TREES, 2002). It is important to note that the ideas discussed here were built upon the concepts of statistics and random processes introduced in the previous subsections.

Classical estimation theory, as the name suggests, is the field of study concerned with the estimation of unknown parameters under specific statistical assumptions. These parameters may be deterministic but unknown, or random in nature. When selecting an estimation approach, it is essential to consider the nature of the parameters being estimated. Furthermore, since the estimation is performed from measurements of a signal, i.e. phenomenon of interest, the probability distribution associated with that signal must also be taken into account.

Consider the case where the parameters of interest are deterministic but unknown. Let $s[n; \theta]$ represent a deterministic signal that depends on the parameter θ. The observed signal,

denoted by $y[n]$, corresponds to the n-th measurement and can be modeled as

$$y[n] = s[n;\theta] + z[n], \tag{1.36}$$

where $z[n]$ is a zero-mean random variable with PDF $f_Z(z[n])$. The term $z[n]$ accounts for the additive noise or perturbations that occur during the measurement process.

Since $s[n;\theta]$ is deterministic, the PDF of the observation $y[n]$, denoted as the likelihood function $p_{y;\theta}(y[n];\theta)$, has a similar probability distribution to that of $z[n]$, but shifted by $s[n;\theta]$. In other words, the mean of $y[n]$ is $s[n;\theta]$, while its variance is fully determined by the distribution of $z[n]$.

To illustrate this behavior, consider a simple scenario where $s[n;\theta] = A$ and $z[n]$ is a zero-mean Gaussian random variable with variance σ^2. Figure 6 shows the histograms of $z[n]$ and $y[n]$ for $A = 4$. It can be observed that adding the constant A to $z[n]$ shifts its distribution

Figura 6 – Histograms of $z[n]$ and $y[n]$ for $A = 4$. Adding the deterministic component A shifts the distribution of $z[n]$ to the right by A, resulting in the distribution of $y[n]$ with mean $\mathbb{E}\{y[n]\} = A$.

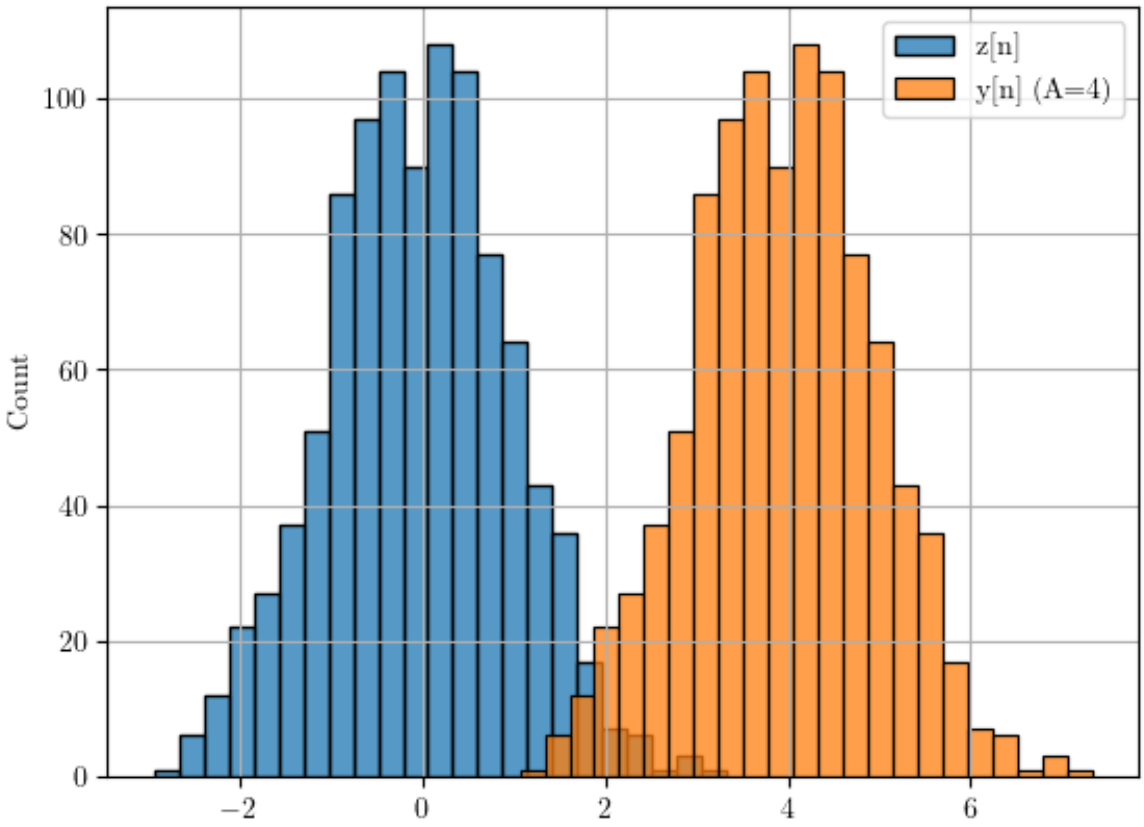

Source: Made by the author.

by A, resulting in $\mathbb{E}\{y[n]\} = A$. This behavior naturally extends to the case where $s[n;\theta]$ is

not a constant function. In such cases, each sample of $s[n;\theta]$ introduces a different shift to the distribution of the corresponding sample of $y[n]$.

For simplicity, throughout the rest of this section, it is assumed that $z[n]$ follows a normal distribution with zero mean and variance σ_z^2. In shorthand notation, this can be expressed as $z[n] \sim \mathcal{N}(0, \sigma_z^2)$. It should also be noted that the reasoning developed in this section can be extended to other perturbation models with different PDFs, without loss of generality.

In light of the previous discussion, we can define the likelihood function of $y[n]$, i.e. $p_y(y;\theta)$. It is similar in essence to the concept of conditional PDF, with the difference that $y[n]$ is conditioned on the unknown parameters θ.

In this context, consider a set of N measurements of $y[n]$, denoted as $\{y[1], y[2], \ldots, y[N]\}$. These observations can be arranged into the vector $\mathbf{y} \in \mathbb{C}^{N\times 1}$. Assuming that all realizations of $z[n]$ are IID, the joint likelihood function of $\mathbf{y}$ can be expressed as

$$\begin{aligned} p_{\mathbf{y}}(\mathbf{y};\theta) &= \prod_{n=1}^{N} p_y(y[n];\theta) \\ &= \frac{1}{(2\pi\sigma_z^2)^{N/2}} \exp\left(-\frac{1}{2\sigma_z^2} \sum_{n=1}^{N} \big(y[n] - s[n;\theta]\big)^2 \right). \end{aligned} \tag{1.37}$$

In general terms, an estimator $\hat{\theta}(\mathbf{y})$ can be defined as a vector-valued function that maps the observation vector $\mathbf{y} \in \mathbb{C}^{N\times 1}$ to an estimate of the true parameter vector θ.

In classical estimation theory, estimators are conceived under the assumption that the likelihood function of the measurements is known in advance. In this context, there exists a wide range of techniques that can be employed to derive $\hat{\theta}(\mathbf{y})$. However, regardless of the specific approach adopted, it is ideally expected that a good estimator converges to the true value of θ.

This convergence is evaluated in terms of $\mathbb{E}\{\hat{\theta}(\mathbf{y})\}$, such that an estimator is said to converge to θ if and only if:

$$\mathbb{E}\{\hat{\theta}(\mathbf{y})\} = \theta. \tag{1.38}$$

Estimators that satisfy Eq. (1.38) are classified as unbiased estimators. However, even if Eq. (1.38) is satisfied, it is desirable that the fluctuations of $\hat{\theta}(\mathbf{y})$ around the actual value of remain θ stable and small as N is increased. This is directly related to the notion of a consistent estimator.

Definition 1.1.7. *Let $\hat{\theta}(\mathbf{x})$ be an unbiased estimator of θ. It is said to be consistent if, as the number of samples N of $y[n]$ tends to infinity,*

$$\hat{\theta}(\mathbf{y}) \to \theta,$$

which is equivalent to requiring that

$$\mathrm{Var}(\hat{\theta}(\mathbf{y})) \to 0.$$

In other words, the estimator's fluctuations around the true value θ become infinitesimally small as N grows. To illustrate this behavior, consider the previous example where $s[n;\theta] = A$. Assuming a maximum likelihood (ML) estimator (KAY, 1993; TREES, 2004; YIN *et al.*, 2023), for $A = 4$, Figure 7 shows how the fluctuations around A diminish as N increases.

Figura 7 – Illustration of estimator consistency: as the number of samples N increases, the fluctuations of the maximum likelihood estimate $\hat{A}$ around the true value $A = 4$ decrease, and the estimator converges toward the true parameter.

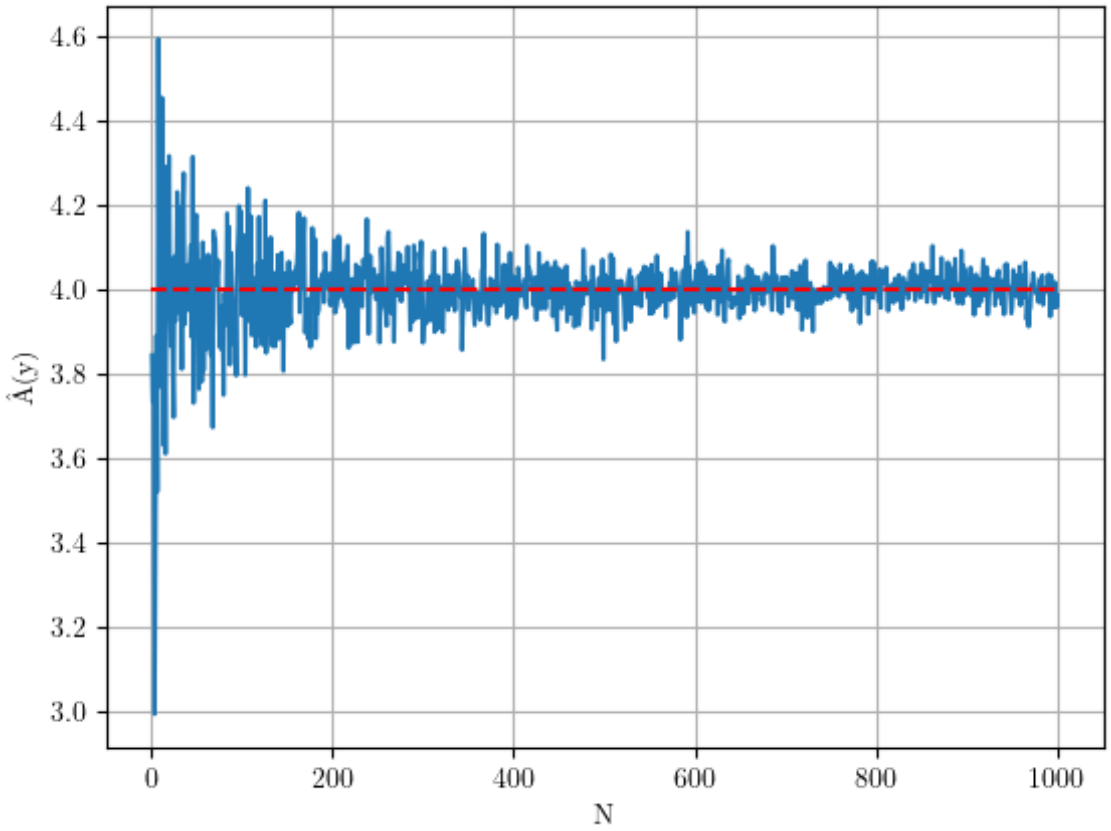

Source: Made by the author.

It is important to note that being unbiased and consistent does not necessarily imply that $\hat{\theta}(\mathbf{y})$ is a good estimator, or the best one available. An estimator should ideally be unbiased

and consistent, but it must also achieve a variance that is as low as possible compared to other estimators.

Moreover, it is desirable to establish a baseline for the variance of an estimator. Such a baseline should be universal, in the sense that it can serve as a benchmark for any unbiased and consistent estimator of a given unknown parameter, while still being defined with respect to the parameter under estimation. In this context, the Cramér-Rao lower bound (CRLB) (KAY, 1993; TREES, 2004) as the name suggests provides a lower bound on the variance of any unbiased estimator.

From (KAY, 1993), the CRLB can be described, according to the following theorem:

Teorema 1.1.1 (Cramér-Rao Lower Bound)**.** *Let $p_{\mathbf{y}}(\mathbf{y};\theta)$ be a likelihood function that satisfies the "regularity"condition*

$$\mathbb{E}\left\{\frac{\partial \ln p_{\mathbf{y}}(\mathbf{y};\theta)}{\partial \theta}\right\} = 0, \text{ for all } \theta. \tag{1.39}$$

Then, the covariance matrix of any unbiased estimator $\hat{\theta} \in \mathbb{C}^{K\times 1}$ must satisfy,

$$\mathbf{C}_{\theta} - \mathbf{I}^{-1}(\theta) \succeq \mathbf{0}, \tag{1.40}$$

where, $\mathbf{I}(\theta)$ stands for the Fisher information matrix (FIM), defined as follows

$$[\mathbf{I}(\theta)]_{k,l} = -\mathbb{E}\left\{\frac{\partial^2 \ln p_{\mathbf{y}}(\mathbf{y};\theta)}{\partial \theta_k \partial \theta_l}\right\}, \tag{1.41}$$

for $k = 1,\ldots,K$ and $l = 1,\ldots,K$.

Furthermore, an unbiased estimator may be found that attains the bound in that, $\mathbf{C}_{\theta} = \mathbf{I}^{-1}(\theta)$, if and only if

$$\frac{\partial \ln p_{\mathbf{y}}(\mathbf{y};\theta)}{\partial \theta} = \mathbf{I}(\theta)(\mathbf{g}(\mathbf{y}) - \theta). \tag{1.42}$$

where $\mathbf{g}(\mathbf{y})$ is minimum variance unbiased (MVU) estimator, $\hat{\theta} = \mathbf{g}(\mathbf{y})$, and $\mathbf{I}(\theta)^{-1}$ is the minimum variance that can be achieved by this estimator.

1.2 Background on Wireless Communications

This section now introduces a theoretical background on wireless communications, which is one of the core foundations of this work. This section begins with a discussion of the most relevant mathematical and physical concepts of array signal processing in the context of multiple-input multiple-output (MIMO) systems. Subsequently, it discusses user-centric cell-free networks in contrast to the classical cellular network design, highlighting the advantages of this novel network paradigm, and finishes by introducing the concept of ISAC.

1.2.1 Array Signal Processing

One of the key technologies that contributed to the success of 4G over its predecessor, 3G, was the introduction of hardware employing multiple antennas at both the transmitter (Tx) and receiver (Rx) nodes. This technology, known as MIMO (ISHTEYAQ; MUZAFFAR, 2022), was conceived to exploit spatial diversity and improve link reliability and spectral efficiency.

To provide a deeper understanding of the MIMO architecture, let us first consider a SISO system, as illustrated in Figure 8. This system consists of Tx and Rx nodes, each equipped

Figura 8 – Representation of a SISO system. The Tx and Rx nodes are each equipped with a single antenna, and the signal propagation occurs through an LOS path.

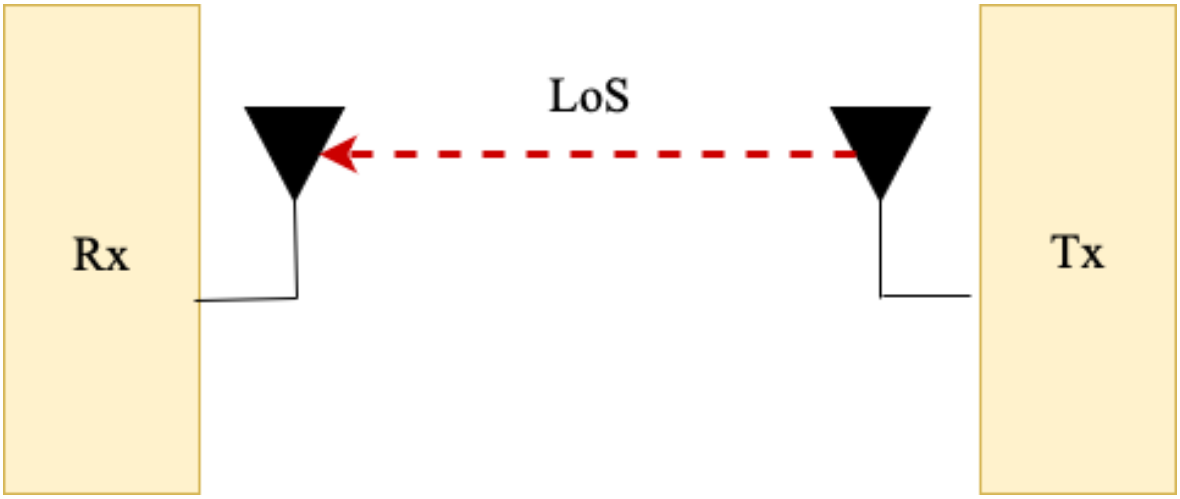

Source: Made by the author.

with a single antenna. Furthermore, consider that a signal $x[t]$ is transmitted from the Tx node to the Rx node, and, for simplicity, assume a LOS propagation path (AL-HOURANI, 2020) between them, i.e., a direct path without reflecting obstacles. At the Rx, the received signal is an attenuated and delayed version of $x[t]$. In this context, Eq. (1.43) provides a mathematical model for the baseband-equivalent received signal (PROAKIS; SALEHI, 2001; HAYKIN, 2008), denoted by $y[t]$.

$$y[t] = hx[t] + z[t], \tag{1.43}$$

where $h = \alpha e^{-j2\pi f_c \tau}$ represents the complex channel coefficient that models the effects of attenuation and propagation delay. Here, α, τ, and f_c denote the attenuation factor, the propagation delay, and the carrier frequency, respectively, while $z[t]$ represents the additive noise component.

Note that, for this setup, the channel is a scalar. Therefore, if the channel coefficient h is known, the transmitted signal can be recovered simply by dividing $y[t]$ by h. Furthermore,

this channel model is conceived under the LOS assumption. As the number of propagation paths increases, the nature of the resulting channel tends to become random due to the presence of multiple reflections, scattering, and diffraction effects. Nevertheless, the reasoning for recovering the original signal remains essentially the same.

Consider now that two additional antennas are introduced to the system, one at each node, as illustrated in Figure 9.

Figura 9 – Representation of a MIMO system. The Tx and Rx nodes are each equipped with two antennas, and the signal propagation occurs through an LOS path.

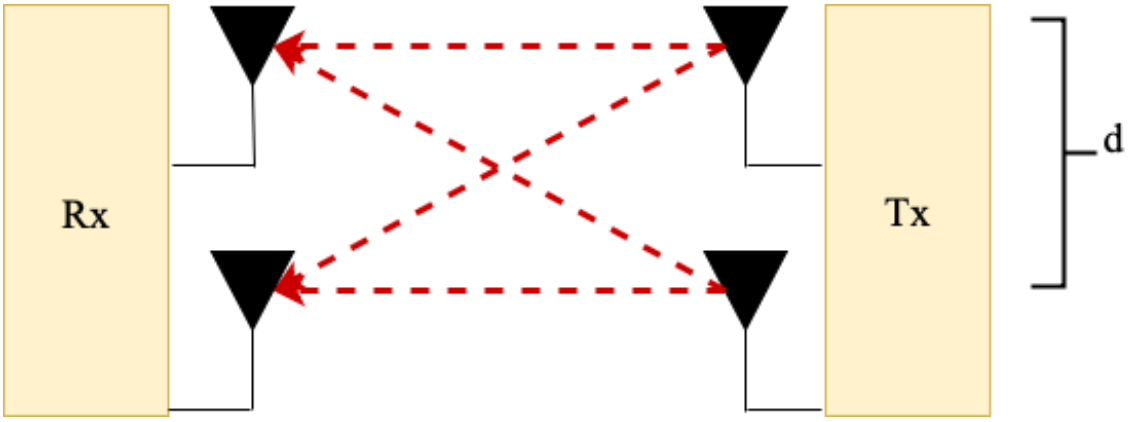

Source: Made by the author.

Assume that each Tx antenna transmits a distinct signal, denoted by $x_1[t]$ and $x_2[t]$. The signals received at the Rx antennas, $y_1[t]$ and $y_2[t]$, are superpositions of delayed and attenuated versions of the transmitted signals. The resulting signal model can therefore be expressed in Eq. (1.44), as follows:

$$\mathbf{y}[t] = \mathbf{H}\mathbf{x}[t] + \mathbf{z}[t], \tag{1.44}$$

where $\mathbf{y}[t] = \begin{bmatrix} y_1[t] & y_2[t] \end{bmatrix}^T \in \mathbb{C}^{2\times 1}$ is the received signal vector, $\mathbf{x}[t] = \begin{bmatrix} x_1[t] & x_2[t] \end{bmatrix}^T \in \mathbb{C}^{2\times 1}$ is the transmitted signal vector, $\mathbf{z}[t] \in \mathbb{C}^{2\times 1}$ represents the additive noise vector, and $\mathbf{H} \in \mathbb{C}^{2\times 2}$ is the channel matrix, whose entries $h_{i,j}$ represent the channel coefficients between the j-th Tx antenna and the i-th Rx antenna.

At this point, it should be noted that $x_1[t]$ and $x_2[t]$ are multiplexed in space, which enables the simultaneous transmission of different parts of the same message. Moreover, the reasoning for recovering $\mathbf{x}[t]$ is analogous to the SISO case, in the sense that, if the channel matrix $\mathbf{H}$ is known and invertible, the transmitted signal can be recovered from the received vector $\mathbf{y}[t]$. Note that Eq. (1.44) can be expressed with any number of Tx and Rx antennas, without loss of generality.

Furthermore, it must be stated that enabling spatial multiplexing is not the only advantage of employing multiantenna systems. From the Tx node perspective, the use of multiple antennas allows beamforming (VEEN; BUCKLEY, 1988), which consists of shaping the Tx power distribution to direct Tx towards a region of interest and to attenuate the transmission towards undesirable directions. Analogously, from the Rx node perspective, multiple antennas can also be used for beamforming to enhance reception in a direction of interest while attenuating the power received from undesired directions.

To illustrate the concept of beamforming under the far-field assumption, consider a point source transmitting a planar wavefront (BALANIS, 2012), which is described by the time-varying electric field vector $\mathbf{E}(\vec{\mathbf{r}},t)$ as follows:

$$\mathbf{E}(\vec{\mathbf{r}},t) = \alpha e^{j(\mathbf{k}^T\mathbf{r}-2\pi f_c(t-\tau))}s[n-\tau]. \tag{1.45}$$

where α denotes a complex gain accounting for propagation effects, f_c is the carrier frequency, and τ represents the propagation delay. The vector $\vec{\mathbf{r}}$ denotes the spatial position at which the wave is observed, while $\mathbf{k} = \frac{2\pi}{\lambda}\hat{\mathbf{k}}$ is the wave-vector, where $\hat{\mathbf{k}}$ unitary vector that indicates the direction of propagation of the wave. The term $s[n-\tau]$ represents the transmitted signal signal delayed by τ.

Moreover, this wavefront is assumed to be transmitted toward an Rx node located sufficiently far from the source, which is equipped with a uniform linear array (ULA) (TREES, 2002; YEN, 1985) composed of N antenna elements, equally spaced by a distance d and vertically arranged along the z-axis, as depicted in Figure 10.

Note that, if the source is sufficiently far from the Rx, the impinging wavefronts at the antenna elements can be approximated as parallel.

Therefore, consider that the antenna element located at $\vec{\mathbf{p}}_0 = \begin{bmatrix} 0 & 0 & 0 \end{bmatrix}$ is chosen as a reference point. Thus, the wavefront takes $\tau_0 = \frac{R_0}{c}$ to propagate a distance of R_0 from the source towards the reference point. Moreover, note that, depending on the angle of arrival (AoA), each antenna element experiences a distinct, yet proportional, propagation delay, since the distance R_n from the source towards each n-th antenna element of the ULA, located at $\vec{\mathbf{p}}_n = \begin{bmatrix} 0 & 0 & nd \end{bmatrix}$ $n = 0,1,\ldots,N-1$, can be expressed in terms of R_0:

$$R_n = R_0 - n\Delta R. \tag{1.46}$$

Note that the term ΔR can be expressed as the projection of the position vector of the first antenna element, $\vec{\mathbf{p}}_1$, onto the direction of arrival unit vector $\vec{\mathbf{r}}$. For the geometry considered, this

Figura 10 – Geometric model of a plane wave impinging on a three-element uniform linear array (ULA) aligned along the z-axis, with an angle of incidence θ relative to the array broadside, resulting in a path difference $\Delta R = d\sin\theta$ between adjacent elements.

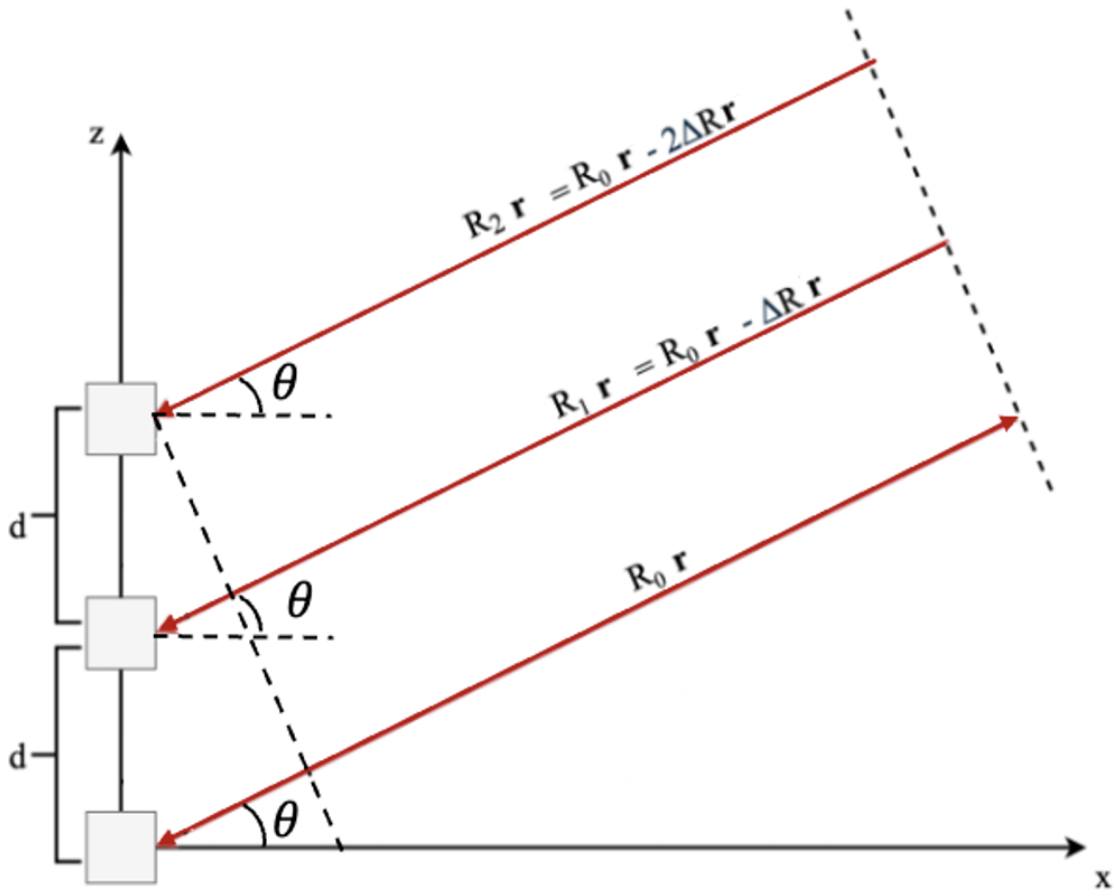

Source: Made by the author.

projection yields $\Delta R = d\sin\theta$. As a consequence, the propagation delay observed at the n-th antenna element, τ_n, can be expressed as follows:

$$\tau_n = \tau - \frac{n\,d\sin\theta}{c}. \tag{1.47}$$

Assume now that the individual responses of the antenna elements are combined at the Rx node by assigning a distinct weight w_n to each element. Under this assumption, the baseband representation of the resulting combined signal can be expressed as follows:

$$y[t] = \sum_{n=0}^{N-1} w_n \alpha e^{-j2\pi f_c \tau_n} s[t-\tau_n]. \tag{1.48}$$

Moreover, by substituting Eq. (1.47) into Eq. (1.48)

$$y[t] = \alpha e^{-j2\pi f_c \tau} \sum_{n=0}^{N-1} w_n e^{j\frac{2\pi}{\lambda} n d\sin\theta} s[t-\tau_n]. \tag{1.49}$$

Furthermore, extending this development to narrowband signals (TREES, 2002; ASPLUND *et al.*, 2020), implies that the approximation $s[t-\tau_n] \approx s[t-\tau_m] \approx s[t]$ holds for all $n = 0,\dots N-1$ and $m = 0,\dots N-1$. Note that this approach will be accurate for the case where the propagation delay difference $\Delta\tau \approx \tau_m - \tau_n$ is small. As a consequence, Eq. (1.49) can be rewritten as follows:

$$y[t] = \alpha e^{-j2\pi f_c \tau}\left(\sum_{n=0}^{N-1} w_n e^{j\frac{2\pi}{\lambda}nd\sin\theta}\right)s[t]. \tag{1.50}$$

From Eq. (1.50), note that $\sum_{n=0}^{N-1} w_n\, e^{j\frac{2\pi}{\lambda}nd\sin\theta}$ acts as a scaling factor. From now on, we refer to this term as the array factor, $AF(\theta)$.

Since the array factor multiplies the received field, the received power is scaled by its squared magnitude, to which we now refer to as the gain pattern:

$$\left|AF(\theta)\right|^2 = \left|\sum_{n=0}^{N-1} w_n\, e^{-j\frac{2\pi}{\lambda}nd\sin\theta}\right|^2. \tag{1.51}$$

Initially, let us assume that $w_n = \frac{1}{N}$ for all $n = 0,\dots N-1$, for simplicity and without loss of generality. It is possible to further develop Eq. (1.51) as follows:

$$\begin{aligned}\sum_{n=0}^{N-1} e^{j\frac{2\pi}{\lambda}nd\sin\theta} &= \frac{1-e^{j\frac{2\pi}{\lambda}Nd\sin\theta}}{1-e^{j\frac{2\pi}{\lambda}d\sin\theta}} \\ &= \frac{e^{j\frac{\pi}{\lambda}Nd\sin\theta}\left(e^{-j\frac{\pi}{\lambda}Nd\sin\theta} - e^{j\frac{\pi}{\lambda}Nd\sin\theta}\right)}{e^{j\frac{\pi}{\lambda}d\sin\theta}\left(e^{-j\frac{\pi}{\lambda}d\sin\theta} - e^{j\frac{\pi}{\lambda}d\sin\theta}\right)} \\ &= e^{j\frac{\pi}{\lambda}(N-1)d\sin\theta}\frac{\sin\left(\frac{\pi}{\lambda}Nd\sin\theta\right)}{\sin\left(\frac{\pi}{\lambda}d\sin\theta\right)}.\end{aligned} \tag{1.52}$$

Therefore,

$$\left|AF(\theta)\right|^2 = \left(\frac{1}{N}\right)^2\left|\frac{\sin\left(\frac{\pi}{\lambda}Nd\sin\theta\right)}{\sin\left(\frac{\pi}{\lambda}d\sin\theta\right)}\right|^2. \tag{1.53}$$

It is, therefore, clear from Eq. (1.53) that $\left|AF(\theta)\right|^2$ depends on both the AoA θ and the number of antenna elements N. To illustrate this behavior, Figure 11 shows the resulting gain pattern over the angular interval $[-90^\circ, 90^\circ]$ for different values of N. From Figure 11, three key observations can be made. First, the gain pattern reveals that certain angular regions are emphasized while others are attenuated, according to the magnitude of $|AF(\theta)|^2$. Second, the pattern is symmetric and achieves its maximum at $\theta = 0^\circ$. Finally, as N increases, the main lobe becomes narrower and more concentrated around broadside ($\theta = 0^\circ$), at the cost of a larger number of side lobes.

Figura 11 – Array gain pattern, for $N = 2, 4, 6$, considering $d = 0.5\lambda$.

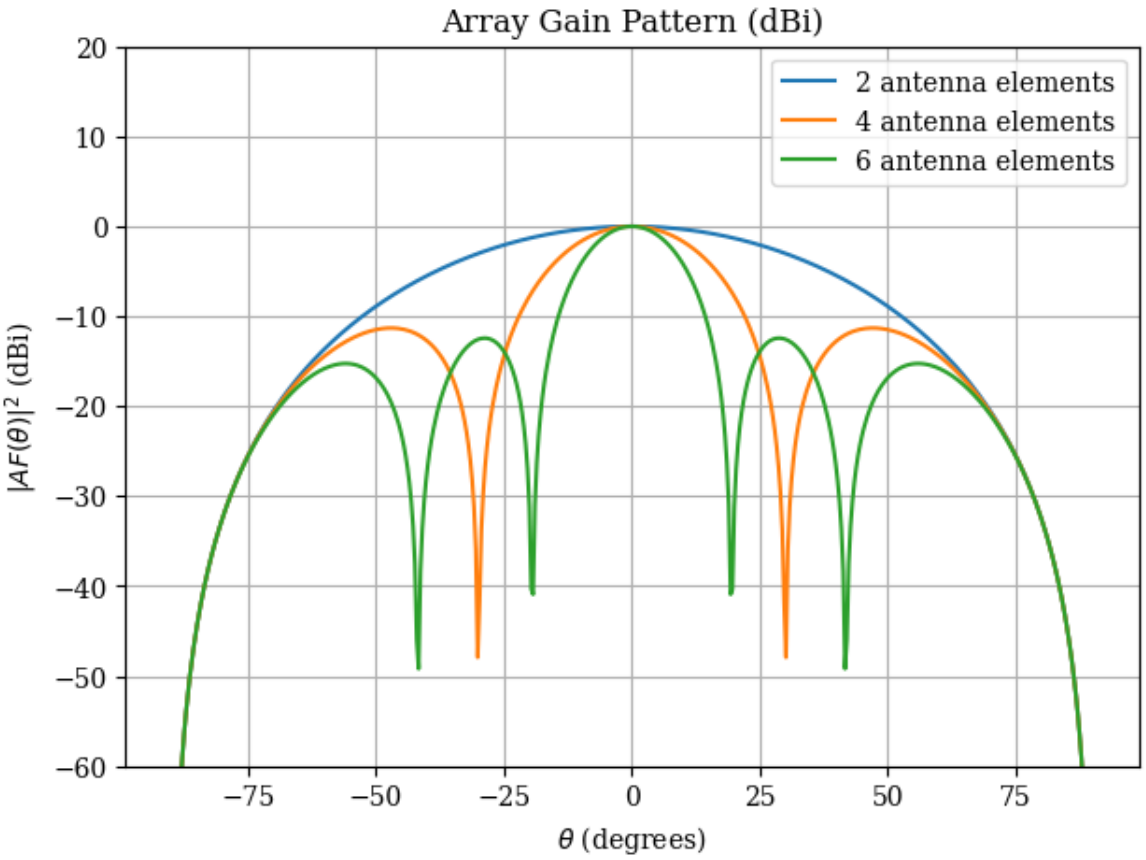

Source: Made by the author.

Therefore, setting $w_n = \frac{1}{N}$ for all $n = 0, \ldots, N-1$ results in the main lobe being steered toward broadside ($\theta = 0°$). More generally, since $1 = e^{-j\frac{2\pi}{\lambda}nd\sin 0°}$, selecting weights of the form $w_n = e^{-j\frac{2\pi}{\lambda}nd\sin\theta'}$ for $n = 0, \ldots, N-1$ steers the beam toward an arbitrary direction θ', such that Eq. (1.53) can be generalized as follows,

$$\left|AF(\theta)\right|^2 = \left(\frac{1}{N}\right)^2 \left|\frac{\sin\left(\frac{\pi}{\lambda}Nd(\sin\theta - \sin\theta')\right)}{\sin\left(\frac{\pi}{\lambda}d(\sin\theta - \sin\theta')\right)}\right|^2. \tag{1.54}$$

In light of this discussion, let us revisit Eq. (1.50) and define the concepts of the steering vector (ROBEY *et al.*, 2001) and the beamforming vector. Note that the $AF(\theta, \phi)$ can be seen as the inner product of two vectors,

- **Steering vector**:

$$\mathbf{a}(\theta) = \left(\frac{1}{\sqrt{N}}\right)\left[1 \quad e^{j\frac{2\pi}{\lambda}d\sin\theta} \quad \ldots \quad e^{j\frac{2\pi}{\lambda}nd\sin\theta} \quad \ldots \quad e^{j\frac{2\pi}{\lambda}(N-1)d\sin\theta}\right]^T, \tag{1.55}$$

where the factor $\frac{1}{\sqrt{N}}$ ensures that the steering vector has unit norm, thus limiting the maximum array gain to 1.

- **Beamforming vector**:

$$\mathbf{w} = \begin{bmatrix} w_0 & w_1 & \dots & w_n & \dots & w_{N-1} \end{bmatrix}^T. \tag{1.56}$$

The term $\frac{1}{\sqrt{N}}$ is implicitly considered in the design of $\mathbf{w}$.

Furthermore, the ULA was chosen for simplicity, as it allows us to illustrate the core concepts developed in this discussion. However, these concepts can be easily generalized to different array designs. To this end, in light of Eq. (1.50) and Eq. (1.55), note that $\frac{2\pi}{\lambda} n d_z \sin\theta = \mathbf{k}^T \mathbf{p}_n$, where $\mathbf{p}_n = \begin{bmatrix} 0 & 0 & n d_z \end{bmatrix}$. Even though a ULA design was assumed for the developments throughout this section, this equality allows Eq. (1.55) to be rewritten in a more general form that also applies to other array geometries, as shown below:

$$\mathbf{a}(\theta,\phi) = \left(\frac{1}{\sqrt{N}}\right) \begin{bmatrix} e^{j\mathbf{k}^T\mathbf{p}_0} & e^{j\mathbf{k}^T\mathbf{p}_1} & \dots & e^{j\mathbf{k}^T\mathbf{p}_n} & \dots & e^{j\mathbf{k}^T\mathbf{p}_{N-1}} \end{bmatrix}^T. \tag{1.57}$$

This new formulation of the steering vector as a function of $\mathbf{k}$ and $\mathbf{p}_n$ is particularly interesting, as it abstracts the array geometry and can therefore be applied to model planar (SAQIB *et al.*, 2021), circular (GUO *et al.*, 2024), or any other antenna-array designs (ANSELMI *et al.*, 2024) defined by the spatial arrangement of its elements. For this reason, it is perceived as a function of the azimuth angle ϕ and the zenith angle θ.

Based on the current discussion, it is evident that employing beamforming techniques at both the Tx and Rx sides in MIMO systems directly impacts the amount of transmitted power effectively received at the Rx node, particularly in the presence of adversarial effects such as path loss. Figure 12 illustrates a simplified pipeline of the power flow from the Tx node to the Rx node, abstracting shadowing and channel fading factors. In this block diagram $G_{Rx}(\theta_{AoA},\phi_{AoA})$,

Figura 12 – Block diagram that summarizes the Power flow from the Rx node towards the Tx node.

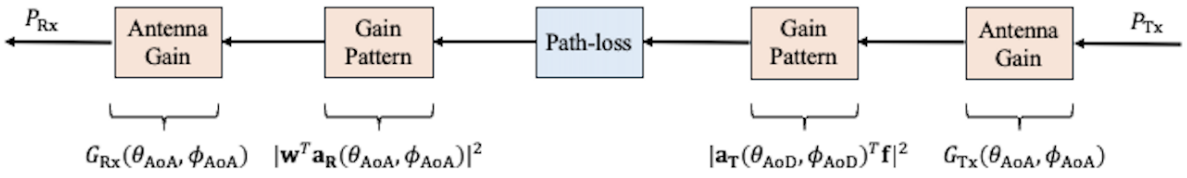

Source: Made by the author.

$G_{Tx}(\theta_{AoD},\phi_{AoD})$, $\mathbf{w} \in \mathbb{C}^{N_R \times 1}$, $\mathbf{f} \in \mathbb{C}^{N_T \times 1}$, $\mathbf{a}_R(\theta_{AoA},\phi_{AoA}) \in \mathbb{C}^{N_R \times 1}$ and $\mathbf{a}_T(\theta_{AoD},\phi_{AoD}) \in \mathbb{C}^{N_T \times 1}$, denote the Rx and Tx antenna gains, the receive beamforming vector, the precoder vector, and

Rx and Tx steering vectors, respectively. Therefore, the Rx power P_{Rx} in this system can be calculated as follows:

$$P_{Rx} = \left(\frac{G_{Rx}(\theta_{AoA},\phi_{AoA}) G_{Tx}(\theta_{AoD},\phi_{AoD})}{\text{Path-loss}} \right) \left| \mathbf{w}^T \mathbf{a}_{\mathbf{R}}(\theta_{AoA},\phi_{AoA}) \mathbf{a}_T(\theta_{AoD},\phi_{AoD}) \mathbf{f} \right|^2 P_{Tx}. \tag{1.58}$$

This expression indicates that the Rx power depends not only on the antenna gains and path-loss, but also on the spatial alignment between the transmit and receive beamforming directions.

From Eq. (1.58), the Rx signal of a MIMO system employing beamforming vectors can be describe as follows:

$$y[t] = \alpha[t] e^{-j\pi f_c \tau} \mathbf{w}^T \mathbf{a}_{\mathbf{R}}(\theta_{AoA},\phi_{AoA}) \mathbf{a}_T(\theta_{AoD},\phi_{AoD})^T \mathbf{f} s[t-\tau] + z[t], \tag{1.59}$$

where $z[t] \sim \mathscr{CN}(0,\sigma^2)$ denotes an additive Gaussian noise and $\alpha[t]$ encapsulates the Tx and Rx antenna gains, the path-loss and other adversarial propagation effects. Note that (1.59) considers an LOS model, since a single propagation path is assumed. However, in many scenarios, due to spreading obstacles the Rx signal will be a superposition of signals coming from multiple propagation paths. To account for a multi path scenario (1.59) can be generalized as follows

$$y[t] = \mathbf{w}^T \left(\sum_{l=1}^{L} \alpha_l[t] e^{-j2\pi f_c \tau_l} \mathbf{a}_{\mathbf{R}}(\theta_{AoA,l},\phi_{AoA,l}) \mathbf{a}_T(\theta_{AoD,l},\phi_{AoD,l})^T \right) \mathbf{f} s[t] + z[t], \tag{1.60}$$

where L denotes the number of propagation paths.

From Eq. (1.60), it is possible to define both the equivalent and MIMO channel representations. Starting with the equivalent channel, it can be interpreted as a multiplicative factor that scales the transmitted symbol $s[t]$, and it is defined as

$$\bar{h}[t] \triangleq \mathbf{w}^T \left(\sum_{l=1}^{L} \alpha_l \, e^{-j2\pi f_c \tau_l} \, \mathbf{a}_R(\theta_{\text{AoA},l},\phi_{\text{AoA},l}) \, \mathbf{a}_T^T(\theta_{\text{AoD},l},\phi_{\text{AoD},l}) \right) \mathbf{f}. \tag{1.61}$$

On the other hand, in light of Eq. (1.44), the MIMO channel matrix $\mathbf{H}[t] \in \mathbb{C}^{N_R \times N_T}$ is defined as follows

$$\mathbf{H}[t] \triangleq \sum_{l=1}^{L} \alpha_l \, e^{-j2\pi f_c \tau_l} \, \mathbf{a}_R(\theta_{\text{AoA},l},\phi_{\text{AoA},l}) \, \mathbf{a}_T^T(\theta_{\text{AoD},l},\phi_{\text{AoD},l}). \tag{1.62}$$

This channel model has particular importance for this PhD thesis, as it highlights the dependencies on the AoA and AoD.

Moreover, design $\mathbf{w}$ and $\mathbf{f}$ according to the perspective discussed so far, i.e. $w_n = e^{j\vec{k}^T \vec{p}_n}$ for all $n = 0,\ldots,N_R-1$ and $f_m = e^{j\vec{k}^T \vec{p}_m}$ for all $m = 0,\ldots,N_T-1$, might not perform very well in a multipath scenario. In this context, beamforming and precoder vectors must be

chosen in such a way to maximize the Rx power (SUN *et al.*, 2024; TAN *et al.*, 2024; XIAO *et al.*, 2024).

In this context, beamforming techniques can generally be classified into three main categories: analog beamforming, digital beamforming, and hybrid beamforming. These three categories will be discussed in further details in the sequence.

- **Analog beamforming**: Analog beamforming (KUTTY; SEN, 2016) is precisely the technique that has been discussed throughout this chapter. Among the three beamforming categories, it offers the simplest implementation, as it relies on a single radio-frequency (RF) chain and adjusts only the phase and amplitude of the signal at each antenna element. However, it provides the least flexibility in shaping the beam pattern compared to digital or hybrid approaches, as all antennas share the same baseband signal. Moreover, analog beamforming does not support the simultaneous formation of multiple independent beams, which limits its ability to serve multiple users or spatial directions at once.
- **Digital beamforming**: Digital beamforming (ALI *et al.*, 2017) can be understood as an evolution of analog beamforming, designed to provide greater flexibility than its predecessor and to enable the implementation of advanced beamforming techniques that were impractical with traditional analog architectures. This flexibility comes at the cost of requiring one RF chain per antenna element, which makes it more complex and costly. Moreover, digital beamforming enables spatial multiplexing, i.e., the simultaneous transmission of multiple data streams, which is particularly advantageous when serving multiple UEs.
- **Hybrid beamforming**: Hybrid beamforming (SOHRABI; YU, 2016; AHMED *et al.*, 2018; AHMED *et al.*, 2017; ELBIR *et al.*, 2023) , on the other hand, is a technology that combines analog and digital beamforming. It consists of a two-stage architecture. In the first stage, the antenna array is connected to a reduced number of RF chains through analog phase shifters, which implement analog beamforming. In the second stage, digital precoding is applied in the baseband domain over the signals produced by the RF chains. This hybrid structure seeks to achieve a balance between the high flexibility of digital beamforming and the lower hardware complexity of analog beamforming.

1.2.2 User-centric Cell-Free Network

Across the evolution from 1st generation (1G) to 5G, communication networks have been designed under a traditional cellular paradigm (MISHRA, 2004; TABASSUM *et al.*, 2019). In this architecture, the base stations are positioned at the center of hexagonal cells and are responsible for serving multiple UEs within their coverage area, as illustrated in Figure 13.

Figura 13 – Cellular network design.

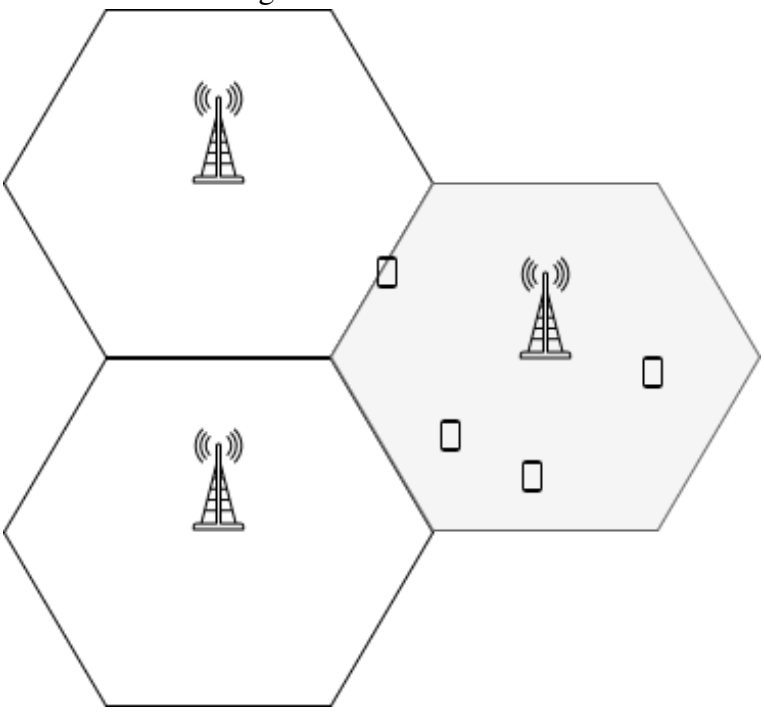

Source: Made by the author.

In this context, it is worth mentioning that some of the benefits of cellular networks include, but are not limited to:

- mobility support (handover);
- ubiquitous connectivity;
- ease of maintenance;
- straightforward upgrades; and
- near-instant connection establishment.

However, despite the aforementioned benefits, cellular networks also exhibit inherent limitations, which have motivated the evolution of wireless architectures toward user-centric network designs. For instance, in cellular networks, UEs tend to experience highly non-uniform path loss within the coverage area of a hexagonal cell; specifically, the farther a UE is from the base station located at the cell center, and consequently closer to the cell borders, the more severe

the path loss becomes. As a result, such UEs also become increasingly exposed to inter-cell interference from neighboring cells. UEs located near the cell borders are commonly referred to as cell-edge UEs, and their presence is one of the key factors motivating research on user-centric network designs as alternatives to mitigate these limitations.

In this context, user-centric networks are envisioned as one of the enabling technologies for upcoming 6G systems. While previous generations were built upon a cellular approach, the user-centric paradigm (AMMAR *et al.*, 2022; YAN *et al.*, 2023; NGO *et al.*, 2024), as the name suggests, places the UE at the center of the network operation. In this paradigm, the traditional notions of cells and cell boundaries are overcome (ZHANG *et al.*, 2019); instead, each UE in the network is served by a cluster of spatially distributed transceivers. In this sense, each UE can be regarded as the effective center of its own serving cluster of transceivers herein referred to as APs, as illustrated in Figure 14.

Figura 14 – User-centric design.

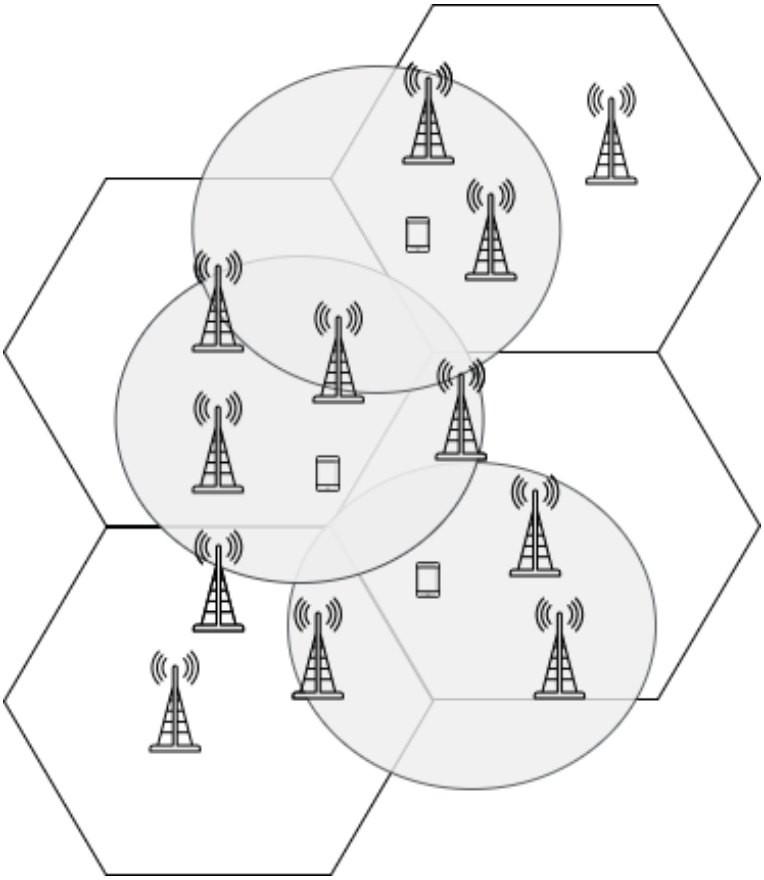

Source: Made by the author.

It is important to highlight the methodologies that can be adopted to form the cluster of transmitters. A first approach relies on a distance-based criterion, as described in (AMMAR;

ADVE, 2019), where APs closest to each UE are selected to form its serving cluster. Alternatively, network performance can also be used as a clustering criterion, as pointed out in (LIU *et al.*, 2016). Additional studies on AP clusterization in user-centric networks can be found in (BJORNSON *et al.*, 2011; NGO *et al.*, 2018; ANTONIOLI *et al.*, 2023).

1.2.3 Integrated Sensing and Communication

An introduction to wireless communication systems was delivered in the previous subsections. Throughout the text, the benefits of employing multiantenna systems were discussed in detail in the context of communication. However, it is important to highlight that radar systems can also benefit from multiantenna technologies. Although radar and wireless communication systems evolved as two independent branches, they share similarities at some level.

According to (SKOLNIK, 2008), radar systems were originally conceived for object detection and localization. Regardless of the specific task, a radar system fundamentally operates by having one or more Tx nodes transmit probing signals over a region of interest. These signals impinge upon a target object and are reflected back toward the one or more Rx nodes, which processes the received echoes to perform detection and/or localization.

Therefore, note that radar systems operate in a similar manner to communication systems. In radar systems, the primary interest lies in the echoes of the Tx signal reflected by the target. However, in architectures where the Tx and Rx nodes are physically separated, the Rx node also receives a direct-path component of the transmitted signal. This direct-path signal is generally undesirable in radar operation since it does not carry any information about the target, and requires additional signal processing steps for suppression or mitigation. In contrast, in communication systems, the transmitted signal itself constitutes the signal of interest. Nevertheless, the Rx also receives components scattered by the surrounding environment, i.e. signals reflected by objects within the propagation medium.

In this context, the integration of radar sensing and communication systems has attracted significant attention from both academia and industry. This integration can be achieved either by extending an existing radar network to support communication services, referred to in the literature as joint radar and communication (JRC) (FENG *et al.*, 2020), or, analogously, by introducing the support of sensing services into a communication network, an approach known as ISAC (LIU *et al.*, 2022). Regardless of the strategy adopted, several inherent challenges arise, including the selection of an appropriate operating frequency band to ensure an adequate QoS

for both communication and sensing, the design of waveforms suitable for dual functionality, and additional system-level trade-offs (LU *et al.*, 2024). For the sake of this PhD dissertation, the remainder of this document will be focusing only on ISAC.

According to the literature, ISAC networks may operate, for instance, in a time division multiplexing (TDM) mode, in which distinct time blocks are allocated to sensing and communication services, such that the network performs only one service at a time. Another alternative is known as concurrent ISAC, in which both services are carried out simultaneously. This can be achieved by employing a common waveform for both functionalities or, alternatively, by using distinct waveforms for each service, leveraging multibeam techniques, exploiting the echoes of communication signals for sensing purposes, and other approaches discussed in the literature. Depending on the Tx node, the sensing service can be classified either as downlink and uplink sensing. ISAC networks can be further classified according to their network architecture (LUO *et al.*, 2026), as follows:

- **Monostatic ISAC network**: in this configuration, both the Tx and Rx nodes are physically collocated within the same network entity. Since a single device is responsible for transmitting probing signals and receiving the echoes reflected from the targets, the targets' AoAs coincide with the AoDs. This architecture inherently suffers from self interference due to the proximity of the Tx and Rx nodes.
- **Bistatic ISAC network**: it offers a greater degree of freedom when compared to the monostatic one. In this configuration the Tx and Rx nodes are no longer collocated, such that the targets' AoAs and AoDs are now defined in terms of the LCS of each node. Furthermore, this architecture overcomes the problem of self interference, since the Tx and Rx nodes are sufficiently separated in space.
- **Multistatic ISAC network**: This configuration can be regarded as an extension of the bistatic architecture, in which multiple Tx and Rx nodes are spatially distributed across the network. Consequently, the system benefits from multiple AoAs and AoDs, one associated with each node, introducing angular diversity that can be exploited to enhance localization accuracy and sensing capabilities.

Furthermore, the implementation of an ISAC network introduces challenges that affect both sensing and communication services. From a communication perspective, user mobility poses a significant challenge, as it inherently causes beam pair link (BPL) misalignment and introduces Doppler shifts that may degrade the QoS. In contrast, from a sensing perspective,

Doppler information is essential, as it enables the estimation of target velocity and is fundamental in applications such as radar tracking and meteorology. Moreover, modern communication systems have evolved to operate effectively in richly scattered environments and can even exploit multipath propagation to enhance performance. Conversely, from a sensing perspective, the presence of a multi-scattering environment introduces clutter, which can significantly degrade target detection and localization performance if not properly mitigated.

1.3 Objectives and Thesis Structure

In light of the overview of random variables, random processes, estimation theory, and wireless communication systems presented in the previous section, this PhD dissertation aims to address the angle estimation problem from different scenarios and perspectives, including communication, a sensing and ISAC scenarios. The remaining chapters of this manuscript address the angle estimation problem under these aforementioned scenarios, following the order presented above.

Chapter 2 addresses the angle estimation problem from a communication perspective. Assuming a MIMO scenario composed of an AP and a single UE, polarization-domain multiplexing is exploited to provide an accurate and efficient algorithm for AoA estimation that relies on a single polarization measurement, by resolving the phase mismatch of virtual subarrays at the Rx node. It is worth noting that the proposed technique can be employed for both uplink and downlink transmissions. As shown in the chapter, these estimates can therefore be used for beam refinement to improve the quality of the BPL between the Tx and Rx nodes. The performance of the proposed technique is evaluated in terms of the absolute AoA estimation error and the resulting RSRP improvement obtained when performing beam refinement.

Chapter 3, on the other hand, addresses the AoA and Doppler frequency estimation problem from a pure sensing network perspective. Two scenarios are analyzed in this chapter: a bistatic scenario composed of a Tx and a Rx AP, both connected to a hypothetical central processing unit (CPU); and a multistatic scenario composed of a single Tx AP and multiple Rxs APs, also with both ends connected to a hypothetical CPU. The asymptotic behavior of the CRLB for both parameters is employed to evaluate the impact of key network parameters, such as the number of Rx nodes and the amount of available time samples. Finally, parameter estimation is carried out using the Newton–Raphson algorithm.

Chapter 4 unifies both communication and sensing perspectives by addressing the

estimation problem under an ISAC framework. This chapter assumes a bistatic ISAC scenario with transmitting (Tx) and receiving (Rx) APs, in which the Tx serves multiple UEs in the downlink while simultaneously sensing a single passive target, estimating its AoA and AoD. In this context, this chapter proposes a joint time-averaged sum-rate and CRLB optimization approach by dividing the region around the Tx node into a given number of sectors and optimally assigning space–time resources to each of them.

Finally, Chapter 5 summarizes the main findings in light of the discussions presented in the previous chapters and provides insights into possible directions for future work.

1.4 Contributions

This section summarizes the main contributions of this PhD dissertation. In this context, the contributions of each subsequent chapter of this document are listed below:

Chapter 2

- In Chapter 2, similarly to (QIN *et al.*, 2020), virtual sub-arrays are exploited to perform the AoA estimation, but instead of making use of time-multiplexing, this work exploits the dual-polarization diversity.
- In (QIN *et al.*, 2020), equal channel gains over time is assumed for reference signal (RS) measurements, which does not hold for the polarization domain. Hence, a channel equalization procedure is proposed to improve the angle estimation.
- The proposed phase estimation falls in a phase ambiguity sub-problem, where multiple phase values are pointed as feasible solution. To handle this issue, this work proposes a sub-optimal solution taking advantage of angular knowledge given by the initial BPL with wide beams.

Chapter 3

- In Chapter 3, a framework for handling multiple observations acquired by multiple Rx APs is introduced to facilitate parameter estimation.
- Evaluating both bistatic and multistatic architectures, the respective CRLB equations were analytically derived. Additionally, these equations were reformulated for specific scenarios useful for understanding system behavior, particularly in distributed MIMO (D-MIMO)

sensing.

- The ML estimator is numerically solved using the Newton–Raphson method to obtain the unknown parameters. In the sequence, Monte Carlo simulations are used to compare its variance with the CRLB.

Chapter 4

- In Chapter 4, the CRLB equations for the target's AoA and AoD estimates are analytically derived from samples of the received echo signals at the Rx node.
- The expression of the communication time-averaged sum rate is analytically derived as well, from the individual signal-to-interference-plus-noise ratio (SINR) expressions for each UE.
- We show that both the CRLB and the time-averaged sum rate are affected by the target's position and by the sensing time allocated to sweeping the sensing beam across the angular sector in which the target is located. Motivated by this property, the area surrounding the Tx is partitioned into equal-width target sensing service areas (TSSAs). A specific sensing time block is then assigned to each TSSA, which we refer to as the sensing space–time resource.
- We formulate a convex optimization problem to allocate space–time resources per TSSA, enhancing the QoS of communication and sensing in terms of time-averaged sum rate and CRLB.

1.5 Scientific Contributions

Currently, the content of this thesis is published or is under review with the following bibliographic information:

[J1] Dos Santos, M. G.; Da Costa, L. R.; Guerreiro, I. M.; Athley, F. *AoA Estimation In Dual-Polarization Virtual Sub-arrays fo Analog Beam Refinement*. **Journal of Communication and Information Systems**, VOL. 40, No.1, 2025, doi:https://doi.org/10.14209/jcis.2025.10.

[C1] Dos Santos, M. G.; Fodor, G.; Freitas,W. C.; Silva, Y. C. B.; Palhano. I. B. *On Estimating the Angle of Arrival and Doppler Frequency in Bistatic and Multistatic Systems*. **2024 IEEE 100th Vehicular Technology Conference (VTC2024-Fall)**, Washington, DC, USA, 2024, pp. 1-5, doi: 10.1109/VTC2024-Fall63153.2024.10757950.

[J2] Dos Santos, M. G.; Freitas,W. C.; Fodor, G. *Space-Time Resource Allocation for Joint CRLB and Communication Rate Optimization*. **IEEE Communications Letters**, 2026 (to be submitted).

It is worth mentioning that this thesis was developed under the context of the following Ericsson/UFC technical cooperation projects:

- **UFC.49** - *Network performance evaluation of a sub-THz downlink system operating under dynamic DTX*, December 2020/ November 2022.
- **UFC.50** - *User-Centric Cell-Free Massive MIMO for Joint Communication and Sensing*, December 2022/ November 2024.
- **UFC.52** - *Fundamental limits and trade-offs, resource sharing and topology impacts*, December 2024/ May 2025.

Within the framework of these projects, the author also collaborated in the following scientific works that are not directly related to the content of this thesis:

Conference Papers

[C2] Palhano. I. B.; Antonioli, R. P.; Silva, Y. C. B.; Fodor, G.; Freitas, W. C.; Dos Santos, M. G. *Power Allocation for Uplink Sensing and Communication in Cell-free ISAC Systems with Multi-Antenna Users and Multibeam*. **2024 IEEE 100th Vehicular Technology Conference (VTC2024-Fall)**, Washington, DC, USA, 2024, pp. 1-5, doi: 10.1109/VTC2024-Fall63153.2024.10757786.

[C3] Oliveira, B.; Dos Santos, M. G.; Freitas, W. C. *Codificações Espaço-Temporais Tensoriais em Sistemas MIMO Sem Fio*. **XXXIX Simpósio Brasileiro de Telecomunicações e Processamento de Sinais**, 2021, On-line.

[C4] Oliveira, B.; Dos Santos, M. G.; Freitas, W. C. *Vehicle Platooning System with Tensor-based Space-Time Coding Schemes*. **XXXIX Simpósio Brasileiro de Telecomunicações e Processamento de Sinais**, 2021, On-line.

[C5] Do Amaral, C. C.; OLIVEIRA, C. A. M.; Dos Santos, M. G.; Mota, J. C. M.; Freitas, G. A. A.; Andriola, W. B. *Análise dos Resultados de Avaliação do Curso de Engenharia de Telecomunicações da Universidade Federal do Ceará – Um Estudo Comparativo nos Anos de 2017 a 2021* **Congresso Brasileiro de Educação em Engenharia, Proceedings of the L Brasilian Congress of Engineering Education**, 2022.

Patents

[P1] Guerreiro, I. M.; Da Costa, L. R.; Dos Santos, M. G.; Karipidis, E, Athley, F. Analog beam refinement in dual-polarization virtual subarrays. WO 20250/80175 A1. November 2023. Patent Application.

2 AOA ESTIMATION IN DUAL-POLARIZATION VIRTUAL SUB-ARRAYS FOR ANALOG BEAM REFINEMENT

This chapter addresses the angle estimation problem from a communication-only perspective, while introducing a novel angle of arrival (AoA) estimator approach designed for analog beam refinement in cellular systems operating in the millimeter-wave (mmWave) bands. In light of the existing literature, the key distinctive aspect of the proposed method is that it exploits the diversity in the polarization domain and virtual sub-arrays to estimate the AoA through a cross-correlation function. Furthermore, the proposed estimator distinguishes itself by requiring a single polarization-multiplexed measurement to provide an accurate estimation of the AoA. To cope with polarization leakage issues, this work proposes a channel equalization in the polarization domain conditioned on the estimation of the cross-channel gain. Simulation results indicate that the beam refinement procedure with the proposed AoA estimator has similar performance to the classical beam sweeping, but using less time-multiplexed measurements.

2.1 Introduction

Obtaining terabit per second data rates is a key requirement for 6G, motivating the use of millimeter-wave (mmWave) (WANG *et al.*, 2023) bands. Nevertheless, these high-frequency bands are inherently subject to severe propagation losses (LI *et al.*, 2024a), which could limit network coverage. To mitigate such losses, the use of large antenna arrays becomes essential.

In high-frequency band scenarios, ensuring good QoS in the communication between transmitter (Tx) and receiver (Rx) nodes requires establishing reliable beam pair links (BPLs) between both entities, defined as the pair of Tx and Rx beams. To this end, beam management (BM) procedures can be employed to ensure the selection of the best BPLs, thereby enhancing the overall communication performance. Initial BPLs usually comprise wide beams and are established during initial/random access phases. Then, once the UE is connected, its initial BPL can be boosted. The classical beam sweeping (BSP) is an effective BM choice by sounding multiple BPL combinations. However, it usually consumes too many time-multiplexed reference signals (RSs) measurements (3GPP, 2022).

A notable characteristic of channels in mmWave bands is their sparsity in propagation paths. Hence, in general, only a single dominant path lies within the main beam coverage of an analog beam (KIM *et al.*, 2019). Therefore, knowledge of the angular information of this path

can be exploited to steer the beams toward it when beam refinement is required, thus emerging as a potentially lower-latency alternative that reduces the RS overhead associated with BSP. In this context, several AoA estimators have been proposed (ZHANG *et al.*, 2023; LI; CHENG, 2021; SONG *et al.*, 2021; QIN *et al.*, 2020).

In (ZHANG *et al.*, 2023), an AoA estimation method is proposed that approximates the power pattern of an analog array using a Gaussian function and requires BSP for AoA estimation. In (LI; CHENG, 2021), the AoA estimator uses multiple single-polarized physical sub-arrays, each connected to a single RF chain. The method consists of computing the correlation among the signals received by sub-arrays placed at different locations and exploiting the phase offsets among them to estimate the AoA. Similarly, (SONG *et al.*, 2021) adopts an interleaved subarray architecture at the receiver and forms a monopulse signal from subarray responses to derive an AoA estimator. Finally, the AoA estimator (QIN *et al.*, 2020) leverages phase correlation between virtual subarrays, avoiding the need for multiple physical subarrays.

Some limitations of such methods must be pointed out. In (ZHANG *et al.*, 2023), the proposed method assumes an ideal array to approximate the array response function to a Gaussian function, ignoring the side lobe effects and realistic antenna gain patterns. Although the methods proposed in (LI; CHENG, 2021; SONG *et al.*, 2021) require only a single transmission, it explores space diversity at the expense of requiring at least two physical sub-arrays with one RF chain each, which may imply increased hardware complexity. In (QIN *et al.*, 2020), the authors choose to explore time diversity at the cost of requiring two time-multiplexed RS transmissions.

Given the limitations addressed above, the contributions of this chapter may be summarized as follows:

- Similarly to (QIN *et al.*, 2020), this work also exploits virtual sub-arrays to perform the AoA estimation, but instead of making use of time-multiplexing, this work exploits the dual-polarization diversity. The beam refinement latency of proposed solution is of one RS measurement.
- In (QIN *et al.*, 2020), equal channel gains over time is assumed for RS measurements, which does not hold for the polarization domain. Hence, this work also proposes a channel equalization procedure to improve the angle estimation.
- The proposed phase estimation falls in a phase ambiguity sub-problem, where multiple phase values are pointed as feasible solution. To handle this issue, this work proposes a sub-optimal solution taking advantage of angular knowledge given by the initial BPL with

wide beams.

Simulation results show the proposed method achieves comparable angle estimation accuracy to (QIN *et al.*, 2020) using less time-multiplexed measurements, and is robust against channel gain and phase ambiguity errors.

The rest of this chapter is organized as follows: Section 2.2 details the system model; Section 2.3 presents the proposed method; Section 2.4 discusses the asymptotical behavior of the Cramér-Rao lower bound (CRLB); Section 2.5 evaluates performance; Section 2.6 concludes the paper.

Notations: $(\cdot)^H$, $(\cdot)^T$, $(\cdot)^*$ denote Hermitian, transpose, and conjugate, respectively. $\mathrm{E}[\cdot]$ is expectation. Bold letters $\mathbf{x}$ and $\mathbf{X}$ represent vectors and matrices. $\mathscr{W}_x$ is a codebook of x-dimensional unit-norm beams. Angles $(\cdot)'$ are defined locally.

2.2 System Model

Consider a Tx/Rx pair in a multiple-input multiple-output (MIMO)-OFDM cellular network operating at carrier frequency f_c in a mmWave band[1]. The development described in the following applies to uplink or downlink, assuming that an initial BPL is established. According to (SLOANE *et al.*, 2023), channel sparsity is inherent to mmWave bands and is stronger than in microwave bands. As larger arrays form narrower beams, only a few paths, often a single one, fall within their coverage area; hence, a LOS-only scenario is considered for this chapter.

Both Tx and Rx use M_T and M_R element ULAs, respectively, with dual-polarization and linear slant angles $\xi_{T,A}, \xi_{T,B}$ and $\xi_{R,A}, \xi_{R,B}$, respectively. Analog beamforming is deployed across the antenna elements connected to each digital port, one per polarization, controlling only the phase of their excitation weights and keeping their amplitude constant. A port as defined in (3GPP, 2022) represents a logical abstraction of one or more physical antennas, where each port is associated with a specific RS transmission. In this context, what matters is the number of antenna ports rather than the number of physical antennas. Antenna element spacing equals $d = 0.5\lambda$ in both ULAs.

A Cartesian, global coordinate system (GCS), (x,y,z), is adopted in which both ULAs are vertically placed along the z axis, as illustrated in Figure 15. No rotation is applied into the Rx ULA, i.e., its local coordinate system (LCS) coincides with the GCS. Then, it points

[1] Single-carrier might be assumed instead under the cost of eventual performance losses due to fewer available samples.

its boresight towards x axis. Furthermore, in this scenario, it is assumed that the Tx ULA can rotate by angle α around the z axis. Thus, it has an LCS, (x′,y′,z′), that is a rotated version of the GCS in terms of α with z′=z, and points its boresight towards x′ axis. From (3GPP, 2019), the transformation from GCS to LCS for the Tx ULA is given by:

$$\begin{aligned} \theta' &= \theta, \\ \phi' &= \phi - \alpha, \end{aligned} \tag{2.1}$$

with θ and ϕ denoting the zenith and azimuth angles, respectively.

Figura 15 – Uplink scenario: Tx rotated by α around z-axis, with AoD and AoA defined in LCS and GCS, respectively.

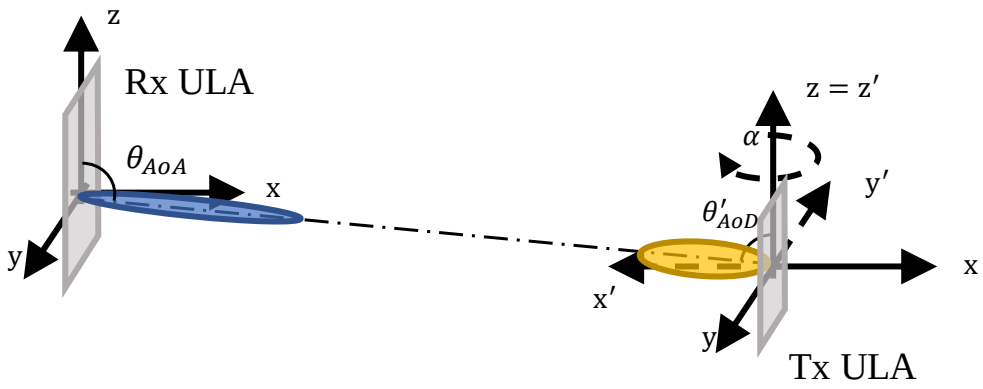

Source: Made by the author.

In this context, the Tx and Rx steering vectors are given by:

$$\mathbf{a}_R(\theta) = \begin{bmatrix} e^{j(M_R-1)\psi_{R,z}} & \dots e^{jn\psi_{R,z}} & \dots & 1 \end{bmatrix}^T \in \mathbb{C}^{M_R \times 1}, \tag{2.2}$$

$$\mathbf{a}_T(\theta) = \begin{bmatrix} e^{j(M_T-1)\psi_{T,z}} & \dots e^{jm\psi_{T,z}} & \dots & 1 \end{bmatrix}^T \in \mathbb{C}^{M_T \times 1}, \tag{2.3}$$

with $\psi_{R,z} = \psi_{T,z} = 2\pi d \cos\theta$.

Let θ_{AoD} and ϕ_{AoD} denote the zenith and azimuth angles of departure from the Tx ULA, the MIMO channel matrix $\mathbf{H}_{i,j} \in \mathbb{C}^{M_R \times M_T}$ between digital ports $i, j \in \{A, B\}$ is given by:

$$\mathbf{H}_{i,j} = \gamma_{i,j} \mathbf{a}_R(\theta_{AoA}) \mathbf{a}_T(\theta_{AoD})^T, \tag{2.4}$$

where $\gamma_{i,j} = \sqrt{A_{\text{RPP}}} \frac{\lambda}{4\pi d} \cos(\xi_{R,i} + \xi_{T,j})$, $A_{\text{RPP}} \triangleq A(\theta_{AoA}, \phi_{AoA}) A(\theta_{AoD}, \phi_{AoD} - \alpha)$, where $A(\theta, \phi)$ is the antenna radiation pattern defined in (3GPP, 2019), which is a function of the azimuth and elevation angles, as depicted in Figure 16. Furthermore, according to (3GPP, 2019) the maximum directional gain of an antenna element $G_{E,max}$ is set to 8dBi. Angle α is the rotation

Figura 16 – Vertical and Horizontal cuts of the antenna radiation pattern described in (3GPP, 2019)

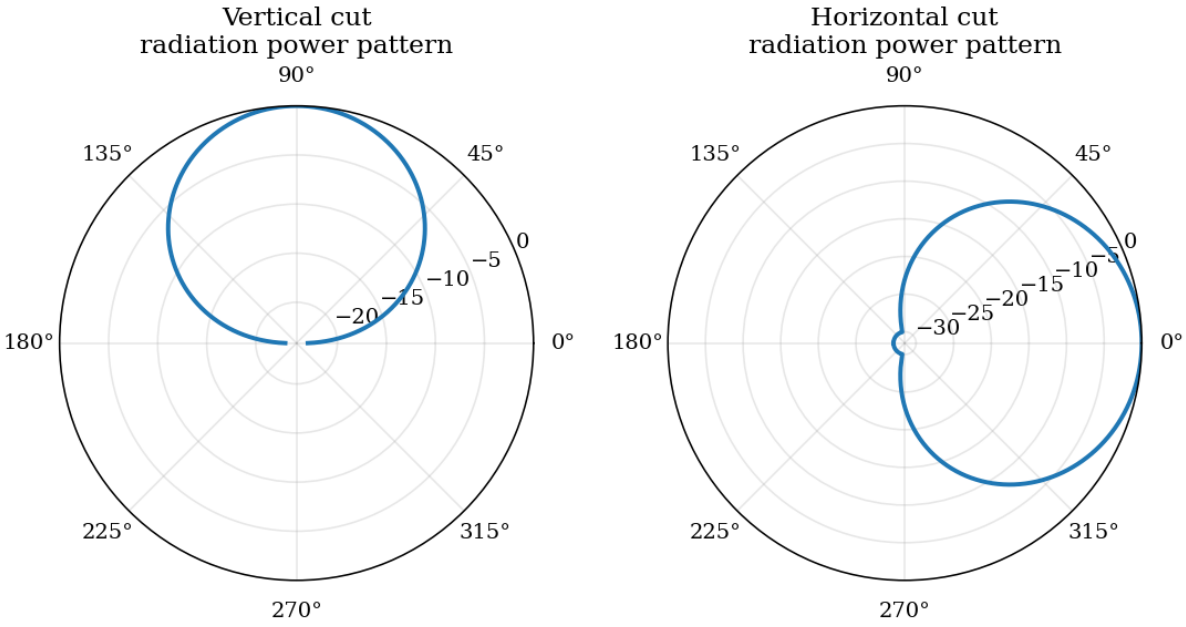

Source: Made by the author.

around the z-axis. The channel in Eq. (2.4) is assumed constant within a few consecutive time resources. The received signal $y_{i,k} \in \mathbb{C}$ at digital port i and receive beam k is:

$$y_{i,k} = \sqrt{\frac{P_{tx}}{2}} \sum_{j \in \{A,B\}} \mathbf{w}_{i,k}^H \mathbf{H}_{i,j} \mathbf{f}_j^* s + z_{i,k}, \tag{2.5}$$

where P_{tx} denotes the Tx power, s is the transmitted symbol, $\mathbf{w}_{i,k}$ and $\mathbf{f}_j$ are beamforming vectors, both assumed to be unit-norm. The noise term $z_{i,k} = \mathbf{w}_i^H \mathbf{z}_{i,k}$ is additive Gaussian noise (AWGN), with $\mathbf{z}_{i,k} \in \mathbb{C}^{M_R \times 1}$ being the Rx AWGN vector, such that $\mathbf{z}_{i,k} \sim \mathscr{CN}(\mathbf{0}, \sigma_z^2 \mathbf{I}_{M_R})$. From Eq. (2.4), this simplifies to:

$$y_{i,k} = \mu_i \mathbf{w}_{i,k}^H \mathbf{a}_R(\theta_{AoA}) b_i + z_{i,k}, \tag{2.6}$$

with $b_i = \sqrt{\frac{P_{tx}}{2}} (\mathbf{a}_T(\theta_{AoD}))^T (\gamma_{i,A} \mathbf{f}_A^* + \gamma_{i,B} \mathbf{f}_B^*) s$, for $i \in \{A,B\}$, contains all Tx-side parameters and polarization-dependent terms.

Moreover, virtual sub-arrays are assumed at the Rx side. At this point, it is important to emphasize the distinction between physical and virtual sub-arrays. In physically separated sub-arrays, the antenna elements are spatially separated into distinct groups, and an independent RF chain is assigned to each polarization of each sub-array. In contrast, virtual sub-arrays are not physically separated; instead, the array is logically partitioned in the signal model, requiring only a single RF chain per polarization for the entire array. Therefore, assuming even M_R, the

receive array is divided into two halves. The array response then becomes:

$$\mathbf{a}_R(\theta) = \left[e^{j\frac{M_R}{2}\psi_{R,z}} \mathbf{a}_0(\theta)^T \quad \mathbf{a}_0(\theta)^T \right]^T . \tag{2.7}$$

Each half-size array is referred to as a *virtual sub-array*. As depicted in Figure 17, we denote the top and bottom sub-arrays as companion array and protoarray, respectively. Consequently, $\mathbf{a}_0(\theta) \in \mathbb{C}^{\frac{M_R}{2}\times 1}$ stands for the array response of the protoarray.

Figura 17 – Virtual sub-array representation: protoarray (bottom) and companion array (top).

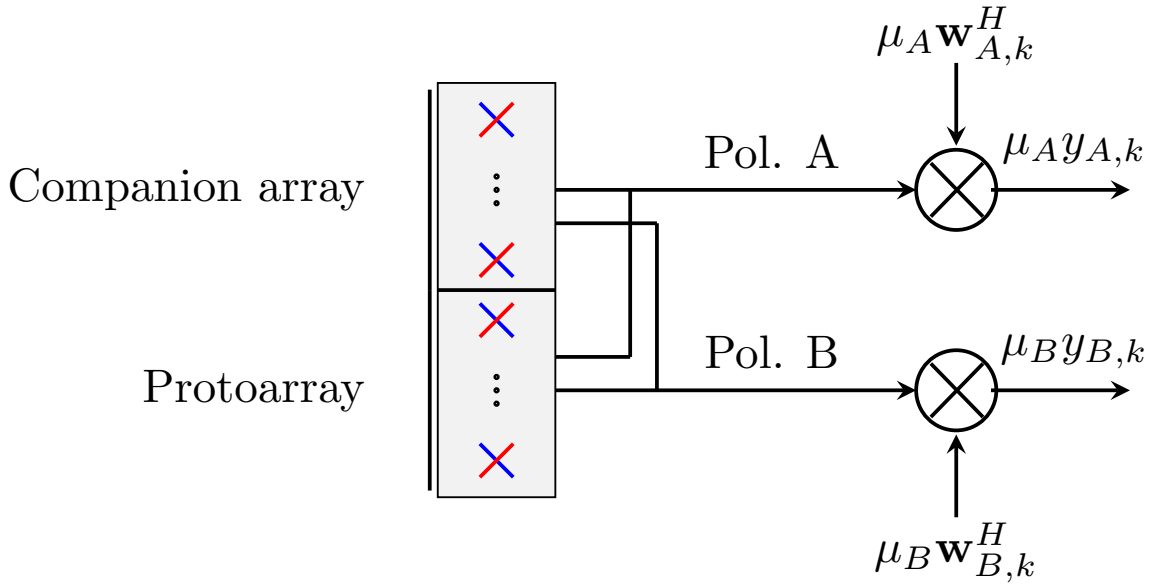

Source: Made by the author.

2.2.1 Problem Formulation

Given an initial BPL obtained during some prior BM procedure, the goal is to perform a beam refinement on the Rx side, i.e., to select $\mathbf{w}_{A,k}, \mathbf{w}_{B,k} \in \mathscr{W}_{M_R}$ in Eq. (1.59) that boost the BPL quality in terms of received power. To this end, the transmit beams $\mathbf{f}_A, \mathbf{f}_B \in \mathscr{W}_{M_T}$ in Eq. (2.5) are assumed fixed.

From Eq. (2.5), we may define the equivalent channel $\Delta_i(\mathbf{w}_{i,k})$ at the i-th port and beamformed by $\mathbf{w}_{i,k}$ as $\Delta_i(\mathbf{w}_{i,k}) = \sum_{j\in\{A,B\}} \mathbf{w}_{i,k}^H \mathbf{H}_{i,j} \mathbf{f}_j^*$, which can be estimated by assuming that symbol s is known and transmitted in multiple subcarriers where channel $\mathbf{H}_{i,j}$ is constant for the purpose of noise mitigation. The BPL quality is then evaluated via the bijective function $\Delta(\mathbf{w}_{A,k}, \mathbf{w}_{B,k}) = \sum_{i\in\{A,B\}} |\Delta_i(\mathbf{w}_{i,k})|^2$. Finally, let $\mathscr{W} \subset \mathscr{W}_{M_R}$ be a codebook of M_R-dimensional candidate beam vectors that contains $L \leq |\mathscr{W}_{M_R}|$ vectors of $\mathscr{W}_{M_R}$. The beam refinement problem

can then be formulated as:

$$\max_{\mathbf{w}_A,\mathbf{w}_B\in\mathscr{W}} \Delta(\mathbf{w}_A,\mathbf{w}_B)\,. \tag{2.8}$$

The problem in Eq. (2.8) is combinatorial as $\mathscr{W}$ is finite and its solution can be found via exhaustive search. Note that the smaller L the lower the exhaustive search burden, but less beam directions are sounded, which decreases the chance of boosting the BPL.

From Eq. (2.6), the BPL quality can be redefined in terms of the gain $|\mathbf{w}^H\mathbf{a}_R(\theta_{AoA})|^2$, assuming that the same beamformer vector is used in both digital ports, i.e., $\mathbf{w}_A=\mathbf{w}_B=\mathbf{w}\in\mathscr{W}_{M_R}$. Although θ_{AoA} cannot be known directly, its estimate $\hat{\theta}_{AoA}$ can be obtained. A problem similar to Eq. (2.8) can be formulated as:

$$\max_{\mathbf{w}\in\mathscr{W}_{M_R}} \left|\mathbf{w}^H\mathbf{a}_R(\hat{\theta}_{AoA})\right|^2, \tag{2.9}$$

which scales with the cardinality of $\mathscr{W}_{M_R}$.

2.3 Proposed Angle Estimator, DP-ViSA

The proposed AoA estimation framework extends the virtual sub-array based AoA (ViSA) algorithm (QIN *et al.*, 2020), both exploiting phase shifts between sub-arrays. Unlike ViSA, which cross-correlates time-lagged RSs, our method uses polarization-multiplexed measurements with cross-channel equalization in the polarization domain.

Proposition 2.3.1. *Let y_i be the received signals at each polarization, $i\in\{A,B\}$. The phase shift $e^{j\frac{M_R}{2}\psi_{R,z}}$ is acquired exploiting the cross-correlation between*

$$r_d=\mu_B y_B-\mu_A y_A, \tag{2.10}$$

$$r_s=\mu_B y_B+\mu_A y_A, \tag{2.11}$$

where $\mu_A=1$, $\mu_B=b_A/b_B$, and, as in (GIRNYK; PETERSSON, 2021),

$$\mathbf{w}_A=\frac{1}{\sqrt{2}}\begin{bmatrix}-\mathbf{w}_0^T & \mathbf{w}_0^T\end{bmatrix}^T,\ \mathbf{w}_B=\frac{1}{\sqrt{2}}\begin{bmatrix}\mathbf{w}_0^T & \mathbf{w}_0^T\end{bmatrix}^T, \tag{2.12}$$

with $\mathbf{w}_0\in\mathscr{W}_{M_R/2}$, and used to estimate the AoA.

Proof. Using Eq. (2.7) and Eq. (2.12) in Eq. (2.6) yields:

$$y_A=\frac{1}{\sqrt{2}}(1-e^{j\frac{M_R}{2}\psi_{R,z}})\mathbf{w}_0^H\mathbf{a}_0 b_A+z_A, \tag{2.13}$$

$$y_B=\frac{1}{\sqrt{2}}(1+e^{j\frac{M_R}{2}\psi_{R,z}})\mathbf{w}_0^H\mathbf{a}_0 b_B+z_B. \tag{2.14}$$

Substituting into Eq. (2.10) and Eq. (2.11), we obtain:

$$r_d = e^{j\frac{M_R}{2}\psi_{R,z}}\mathbf{w}_0^H\mathbf{a}_0 b_A + z_A - z_B\frac{b_A}{b_B}, \tag{2.15}$$

$$r_s = \mathbf{w}_0^H\mathbf{a}_0 b_A + z_A + z_B\frac{b_A}{b_B}. \tag{2.16}$$

Finally, the cross-correlation becomes:

$$\rho = (r_s)^* r_d = |\bar{b}|^2 e^{j\frac{M_R}{2}\psi_{R,z}} + g_z, \tag{2.17}$$

where $\bar{b} = \mathbf{w}_0^H\mathbf{a}_0 b_A$ and g_z is a noisy term. □

Phase estimation: From Eq. (2.17), a set of candidate phases is defined:

$$\mathscr{P}_{\psi_{R,z}} = \left\{ \frac{\angle\rho + 2k\pi}{M_R/2} \,\middle|\, k \in \{-M_R/2, M_R/2\} \right\}. \tag{2.18}$$

where $\mathscr{K} = \{-\frac{M_R}{2}, \frac{M_R}{2}\}$, then introducing a phase ambiguity problem, also observed in (QIN *et al.*, 2020).

Let $\hat{\psi}_{R,z} \in \mathscr{P}_{\psi_{R,z}}$ be the estimated version of $\psi_{R,z}$. Since all the possible values of $\frac{2k\pi}{M_R/2}$ are known and given that $|\cos(\theta_{AoA})| \leq 1$, it is possible to obtain a subset of possible values of θ_{AoA}, defined as $\mathscr{P}_{\theta_{AoA}} = \left\{ \cos\left(\frac{\hat{\psi}_{R,z}}{2\pi d_z} - \frac{2k}{d_z M_R}\right)^{-1} \,\middle|\, \left|\frac{\hat{\psi}_{R,z}}{2\pi d_z} - \frac{2k}{d_z M_R}\right| \leq 1 \right\}$. Then, the best $\hat{\theta}_{AoA}$ may be selected by solving the following problem:

$$\hat{\theta}_{AoA} = \underset{\theta \in \mathscr{P}_{\theta_{AoA}}}{\arg\max} \left| (\mathbf{w}^\star)^H \mathbf{a}_R(\theta, \phi_{AoA}) \right|^2,$$

where $\mathbf{w}^\star$ is the wide beam from the initial BPL.

2.4 Cramér-Rao Lower Bound

From the discussion in Chapter 1, it was mentioned that the CRLB establishes a theoretical lower bound on the variance of any unbiased estimator. Assuming that such a bound exists, it can be used to evaluate the asymptotic behavior of the variance of the estimator with respect to the system parameters. In this context, assuming that the transmitted OFDM signal consists of N subcarriers implies that for each polarization there will be N measurements of the received signal available. These measurements are weighted by μ_A and μ_B and stacked into a

vector $\bar{\mathbf{y}} \in \mathbb{C}^{2N\times 1}$, expressed as

$$\bar{\mathbf{y}} = \begin{bmatrix} \mu_A \mathbf{y}_{A,1} \\ \mu_A \mathbf{y}_{A,2} \\ \vdots \\ \mu_A \mathbf{y}_{A,N} \\ \mu_B \mathbf{y}_{B,1} \\ \mu_B \mathbf{y}_{B,2} \\ \vdots \\ \mu_B \mathbf{y}_{B,N} \end{bmatrix} = \begin{bmatrix} \mathbf{w}_A^H \mathbf{a}_R(\theta_{AoA}) b_{A,1} \\ \mathbf{w}_A^H \mathbf{a}_R(\theta_{AoA}) b_{A,2} \\ \vdots \\ \mathbf{w}_A^H \mathbf{a}_R(\theta_{AoA}) b_{A,N} \\ \mathbf{w}_B^H \mathbf{a}_R(\theta_{AoA}) b_{A,1} \\ \mathbf{w}_B^H \mathbf{a}_R(\theta_{AoA}) b_{A,2} \\ \vdots \\ \mathbf{w}_B^H \mathbf{a}_R(\theta_{AoA}) b_{A,N} \end{bmatrix} + \begin{bmatrix} z_{A,1} \\ z_{A,2} \\ \dots \\ z_{A,N} \\ z_{B,1} \\ z_{B,2} \\ \dots \\ z_{B,N} \end{bmatrix} \triangleq \mu_{\mathbf{y}}[\theta_{AoA}] + \bar{\mathbf{z}} \in \mathbb{C}^{2N\times 1}. \tag{2.19}$$

From Eq. (2.19), it is straightforward to observe that $\mu_{\mathbf{y}}[\theta_{AoA}] \in \mathbb{C}^{2N\times 1}$ is a deterministic vector, and that $\mathbf{z} \in \mathbb{C}^{2N\times 1} \sim \mathscr{CN}(\mathbf{0}, \sigma_z^2 \mathbf{M})$, where $\mathbf{M} = diag([|\mu_A|^2 \mathbf{1}^T \ |\mu_B|^2 \mathbf{1}^T]^T) \in \mathbb{C}^{2N\times 2N}$. Consequently, the likelihood function of $\bar{\mathbf{y}}$, denoted as $p_{\bar{\mathbf{y}}}(\mathbf{y}; \theta_{AoA})$, is also complex Gaussian, i.e. $\bar{\mathbf{y}} \sim \mathscr{CN}(\mu[\theta_{AoA}], \sigma_z^2 \mathbf{M})$, such that

$$p_{\bar{\mathbf{y}}}(\bar{\mathbf{y}}; \theta_{AoA}) = \frac{1}{(\pi\sigma_z)^{2N} |\mu_A \mu_B|^{2N}} \exp\left(\sum_{i\in A,B} \sum_{n=1}^{N} \frac{-|\bar{y}_{i,n} - [\mu_{\mathbf{y}}[\theta_{AoA}]]_{i,n}|^2}{2\sigma_z^2 |\mu_i|^2} \right). \tag{2.20}$$

Therefore, to verify the existence of the CRLB, it is necessary to check whether Eq. (2.20) satisfies the regularity condition which states that,

$$\mathbb{E}\left\{ \frac{\partial \ln p_{\bar{\mathbf{y}}}(\bar{\mathbf{y}}; \theta_{AoA})}{\partial \theta_{AoA}} \right\} = 0. \tag{2.21}$$

To this end, by computing $\frac{\partial \ln p_{\bar{\mathbf{y}}}(\bar{\mathbf{y}}; \theta_{AoA})}{\partial \theta_{AoA}}$, it follows that:

$$\begin{aligned} \frac{\partial \ln p_{\bar{\mathbf{y}}}(\bar{\mathbf{y}}; \theta_{AoA})}{\partial \theta_{AoA}} &= -\sum_{i\in A,B} \sum_{n=1}^{N} \frac{1}{2\sigma_z^2 |\mu_i|^2} \frac{\partial}{\partial \theta_{AoA}} |\bar{y}_{i,n} - [\mu_{\bar{\mathbf{y}}}[\theta_{AoA}]]_{i,n}|^2 \\ &= -\sum_{i\in A,B} \sum_{n=1}^{N} \frac{1}{2\sigma_z^2 |\mu_i|^2} \Bigg[-\frac{\partial [\mu_{\bar{\mathbf{y}}}[\theta_{AoA}]]_{i,n}}{\partial \theta_{AoA}} \bar{y}_{i,n}^* + \frac{\partial [\mu_{\bar{\mathbf{y}}}[\theta_{AoA}]]_{i,n}}{\partial \theta_{AoA}} [\mu_{\bar{\mathbf{y}}}[\theta_{AoA}]]_{i,n}^* \\ &\quad - \bar{y}_{i,n} \frac{\partial [\mu_{\bar{\mathbf{y}}}[\theta_{AoA}]]_{i,n}^*}{\partial \theta_{AoA}} + \mu_{\bar{\mathbf{y}}}[\theta_{AoA}]]_{i,n} \frac{\partial [\mu_{\bar{\mathbf{y}}}[\theta_{AoA}]]_{i,n}^*}{\partial \theta_{AoA}} \Bigg]. \end{aligned} \tag{2.22}$$

Thus, from the distribution of $p_{\bar{\mathbf{y}}}(\bar{\mathbf{y}}; \theta_{AoA})$, $\mathbb{E}\{y_{i,n}\} = [\mu_{\mathbf{y}}[\theta_{AoA}]]_{i,n}$, from Eq. (2.22) it follows that

regularity condition is satisfied. Moreover, from Eq. (2.19) it follows that:

$$\begin{aligned}\frac{\partial[\mu_{\mathbf{y}}[\theta_{AoA}]]_{i,n}}{\partial\theta_{AoA}} &= \frac{\partial}{\partial\theta_{AoA}}\left(\mu_i \mathbf{w}_i^H \mathbf{a}_R(\theta_{AoA}) b_{i,n}\right) \\ &= \mu_i \sum_{m_R=1}^{M_R} w_{i,m_T}^* \frac{\partial e^{j2\pi(m_T-1)d\cos\theta_{AoA}}}{\partial\theta_{AoA}} b_{i,n} \\ &= -j2\pi d\sin\theta_{AoA}\mu_i \sum_{m_R=1}^{M_R} (m_T-1) w_{i,m_R}^* e^{2\pi(m_R-1)d\cos\theta_{AoA}} b_{A,n} \\ &= -j2\pi d\sin\theta_{AoA}\mu_i \mathbf{w}_i^H \mathbf{D}_{M_R}\mathbf{a}_R(\theta_{AoA}) b_{A,n}.\end{aligned} \tag{2.23}$$

where, $\mathbf{D}_{M_R} = diag([0\ 1\ \ldots\ M_R-1]^T) \in \mathbb{C}^{M_R\times M_R}$.

In light of this discussion, and according to (KAY, 1993), the FIM for any vector of unknown parameters ξ can be calculated using the following expression:

$$[\mathbf{I}(\xi)]_{i,j} = \mathrm{tr}\left[\mathbf{C}_{\bar{\mathbf{y}}}^{-1}\frac{\partial\mathbf{C}_{\bar{\mathbf{y}}}}{\partial\xi_i}\mathbf{C}_{\bar{\mathbf{y}}}^{-1}\frac{\partial\mathbf{C}_{\bar{\mathbf{y}}}}{\partial\xi_j}\right] + 2Re\left[\frac{\partial\mu_{\bar{\mathbf{y}}}^H}{\partial\xi_i}\mathbf{C}_{\bar{\mathbf{y}}}^{-1}\frac{\partial\mu_{\bar{\mathbf{y}}}}{\partial\xi_j}\right]. \tag{2.24}$$

Since a single unknown parameter, θ_{AoA}, is assumed in this chapter, and because $\mathbf{C}_{\bar{\mathbf{y}}}$ does not depend on θ_{AoA}, Eq. (2.24) reduces to:

$$I(\theta_{AoA}) = 2Re\left[\frac{1}{\sigma_z^2}\frac{\partial\mu_{\bar{\mathbf{y}}}^H[\theta_{AoA}]}{\partial\theta_{AoA}}\mathbf{M}^{-1}\frac{\partial\mu_{\bar{\mathbf{y}}}[\theta_{AoA}]}{\partial\theta_{AoA}}\right]. \tag{2.25}$$

Thus, by substituting Eq. (2.23) into Eq. (2.25), and assuming that $|s_n|^2 = 1$ and consequently $|b_{A,n}|^2 = |b_A|^2$ for all n, the CRLB $\sigma^2_{\hat{\theta}_{AoA}}$ is obtained as:

$$\begin{aligned}\sigma^2_{\hat{\theta}_{AoA}} &\geq I(\theta_{AoA})^{-1} \\ &\geq \frac{\sigma_z^2}{2(2\pi d\sin\theta_{AoA})^2 N\left(\frac{1}{|\mu_A|^2}|\mu_A\mathbf{w}_A^H\mathbf{D}_{M_R}\mathbf{a}_R(\theta_{\mathbf{AoA}})b_A|^2 + \frac{1}{|\mu_B|^2}|\mathbf{w}_B^H\mathbf{D}_{M_R}\mathbf{a}_R(\mu_B\theta_{\mathbf{AoA}})b_B|^2\right)} \\ &= \frac{\sigma_z^2}{2(2\pi d\sin\theta_{AoA})^2 N\sum_{i\in A,B}|\mathbf{w}_i^H\mathbf{D}_{M_R}\mathbf{a}_R(\theta_{\mathbf{AoA}})b_i|^2}.\end{aligned} \tag{2.26}$$

Note that this result is independent of the values chosen from μ_A and μ_A.

From Eq. (2.26) it is possible to identify an explicit dependency on θ_{AoA}, the number of samples N, the terms $|b_A|^2$, $|b_B|^2$, and the noise variance σ_z^2. To further assess these dependencies, assuming for simplicity that $|b_B|^2 = |b_A|^2$, Eq. (2.26) was plotted by varying $|b_A|^2$ and the number of samples. In Figure 18, the CRLB is calculated for multiple values of $|b_A|^2$, which are expressed in units of σ_z^2. As can be seen, as $|b_A|^2$ becomes greater than σ_z^2, the CRLB tends to decrease. Moreover, from Figure 19, as it was also expected as increasing the number of available samples the CRLB is reduced as well.

Figura 18 – AoA estimator's CRLB varying $|b_A|^2$.

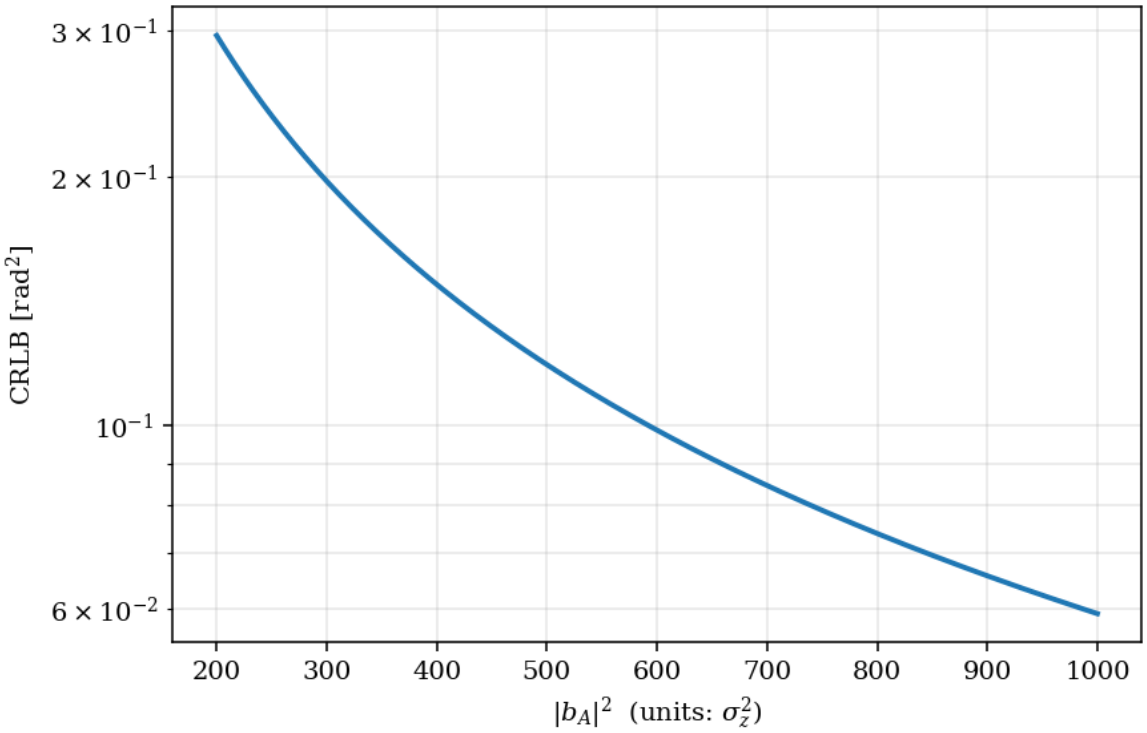

Source: Made by the author.

Figura 19 – AoA estimator's CRLB varying the number of samples.

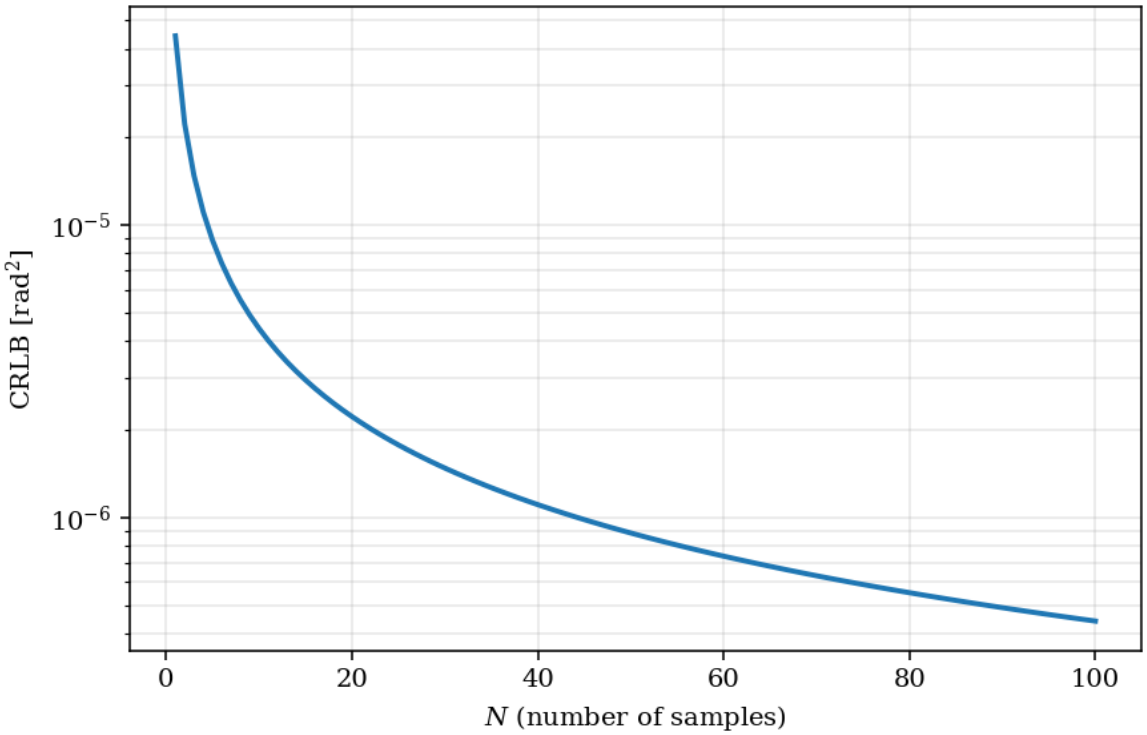

Source: Made by the author.

2.5 Numerical Results

In this section, numerical results are provided to evaluate the proposed beam refinement procedure. The Tx node is randomly positioned using a uniform distribution within the Rx node's azimuth range in $[-\pi/3, \pi/3]$, with a Rx-Tx distance $d \in [10, 50]$ m. The zenith angles of the LOS path are derived from the Rx and Tx coordinates. Table 1 provides a summary of additional simulation parameters. Furthermore, simulations use a comb-type structure with 12

Tabela 1 – SIMULATION PARAMETER SETUP.

Parameter	Value
Monte Carlo samples	1000
Rx height [m]	10
Tx height [m]	1.5
Rx ULA length M_R	64
Tx ULA length M_T	8
Tx rotation angle α [rad]	π
Initial Rx beam	Wide beams (GIRNYK; PETERSSON, 2021) with highest RSRP
Initial Tx beam	DFT beam 0
Tx transmit power P_{tx} [dBm]	10
Noise power spectral density [dBm/Hz]	-174
Narrow beam codebook	DFT without oversampling
Carrier frequency f_c [GHz]	100
Subcarrier spacing [kHz]	960
Channel model	Only LOS component (3GPP, 2019)
Number of frequency-multiplexed symbols	12
Path loss	Free space

Source: Elaborated by the author.

frequency-multiplexed symbols[2] and a free-space path loss model.

The technique's quality was evaluated using two metrics: absolute AoA estimation error and BPL's RSRP. A simplified layer 1 (L1)-RSRP is calculated as follows:

$$\sum_{i\in\{A,B\}} \left| \sum_{j\in\{A,B\}} \mathbf{w}_i^H \mathbf{H}_{i,j} \mathbf{f}_j \right|^2 . \tag{2.27}$$

The proposal, herein called dual-polarization virtual sub-array based AoA (DP-ViSA) estimator was compared with (i) ViSA estimator (QIN *et al.*, 2020), adapted to dual-polarization, in terms of the absolute AoA estimation error, and with (ii) BSP using either two or eight narrow beams, in terms of the L1-RSRP obtained with the selected beams suing both techniques. The number of transmissions required by each simulated method can be seen in Table 2.

We compare DP-ViSA and ViSA, as both rely on similar hardware architectures based on virtual subarrays. ViSA differs by applying an Rx beamforming configuration similar to

[2] Other comb-type factors can be employed without loss of generality.

Tabela 2 – NUMBER OF REFERENCE SIGNAL TRANSMISSIONS REQUIRED BY DIFFERENT BEAM REFINEMENT TECHNIQUES.

Parameter	Value
DP-ViSA	1
ViSA	2
BSP - 2 beams	2
BSP - 8 beams	8

Source: Elaborated by the author.

Eq. (2.12) over two time-multiplexed measurements and exploiting the resulting phase mismatch between subarrays.

To assess ambiguity suppression, DP-ViSA and ViSA are evaluated with both optimal and proposed methods, where $\hat{\psi}_{R,z}$ is compared to all candidate values in Eq. (2.18) and the closest is selected. Simulations also consider the impact of using either an estimated or exact value of the weight ratio $\frac{b_A}{b_B}$.

Figura 20 – Absolute AoA estimation error's CDF (Optimum ambiguity solution).

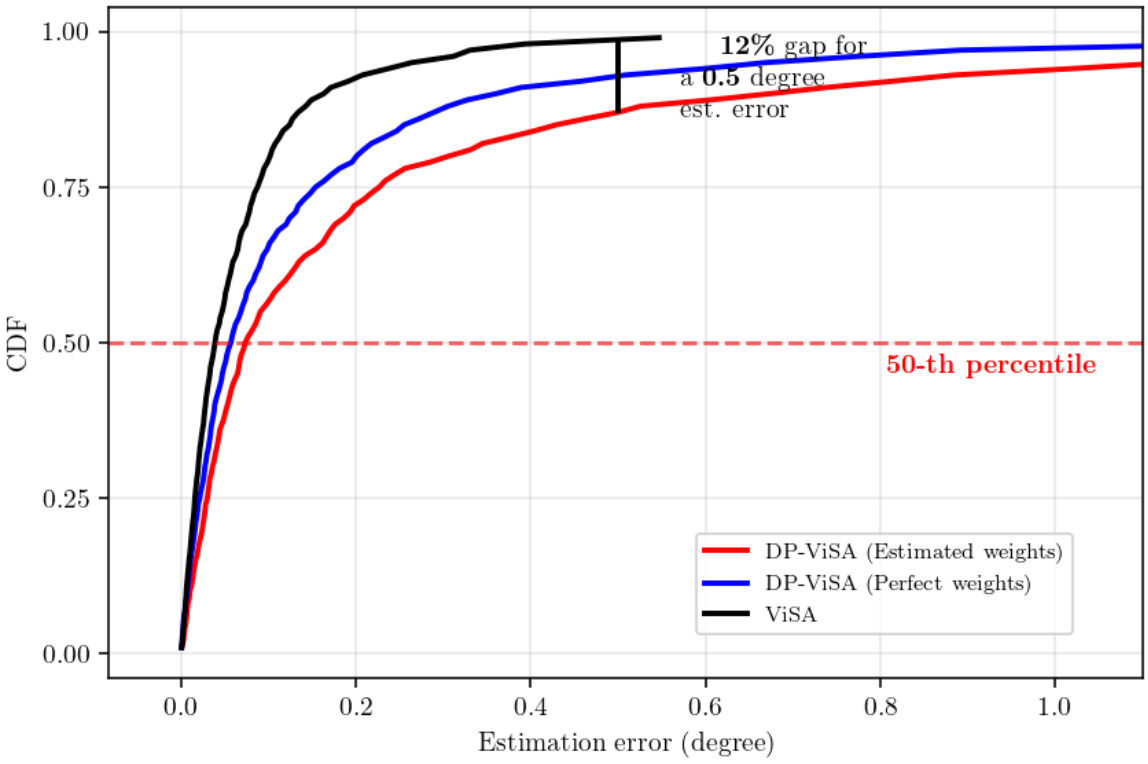

Source: Made by the author.

In Figure 20 and Figure 21, the 50th-percentile performance of both ambiguity suppression methods is very similar. Although ViSA slightly outperforms DP-ViSA (estimated

Figura 21 – Absolute AoA estimation error's CDF (Proposed ambiguity solution).

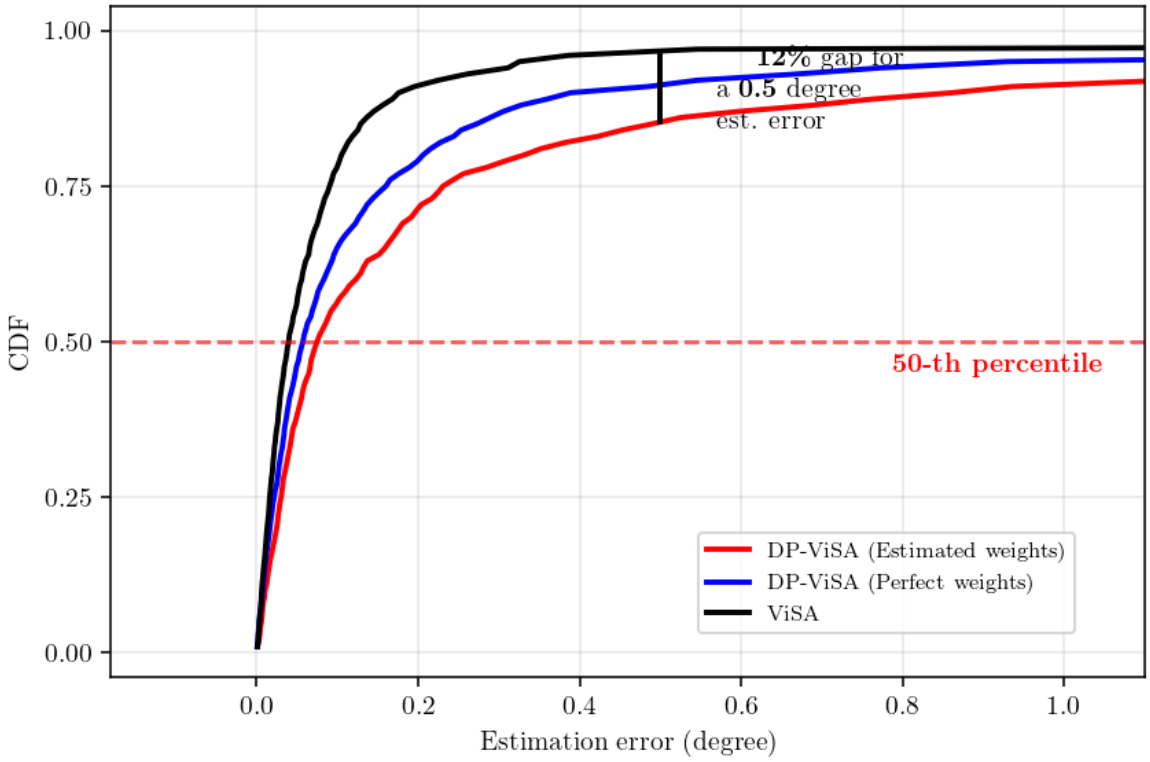

Source: Made by the author.

weights), the gap is merely 0.035 degrees, possibly negligible for beam selection. At a 0.5-degree error, the percentile difference reaches up to 12%, but DP-ViSA still maintains performance above the 80th percentile.

Figures 22 and 23 show that DP-ViSA and ViSA yield similar RSRP distributions. Notably, DP-ViSA (estimated weights) outperforms 2-long BSP by nearly 2 dB at the 50th percentile. For both ambiguity solutions, DP-ViSA achieves performance comparable to eight-beam BSP, albeit slightly lower with the proposed ambiguity method, as expected due to its non-optimality.

2.6 Conclusion

This chapter introduces a dual-polarization extension of the single-polarization ViSA (QIN *et al.*, 2020) estimator for analog beam refinement in cellular systems. The proposed approach provides similar results while requiring only a single time-multiplexed measurement, conditioned on dual-polarization gain knowledge obtained from previous signaling, e.g., during random access, to perform the AoA estimation.

Furthermore, the proposed method provided performance close to that of 8-long

Figura 22 – RSRP's CDF (Optimum ambiguity solution).

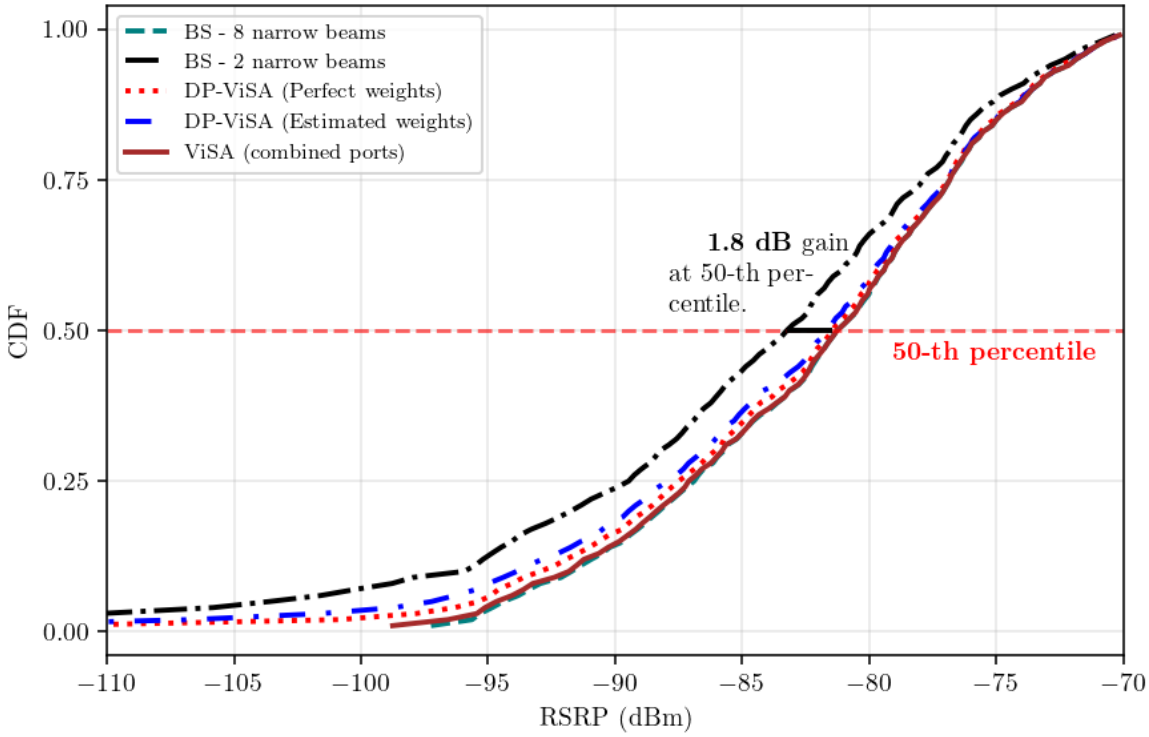

Source: Made by the author.

Figura 23 – RSRP's CDF (Proposed ambiguity solution).

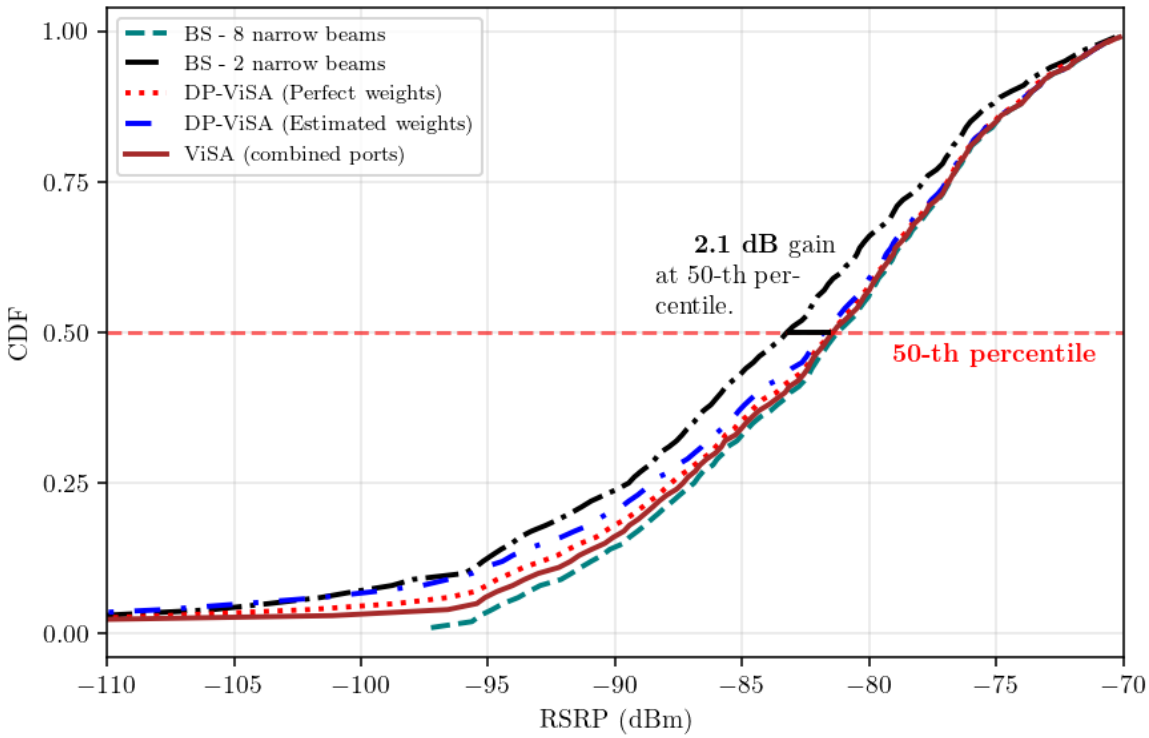

Source: Made by the author.

beam sweeping, but with only a single dual-polarization measurement, i.e., 8x less signaling. The proposal proved up to 2dB better than a 2-long beam sweeping. A sub-optimum solution,

which delivers reliable results, for the ambiguity problem present in both ViSA and DP-ViSA, was also proposed as a contribution of this work.

As future work, one can consider evaluating the proposed AoA estimation in rectangular arrays and also with different sub-array virtualization schemes.

3 ON ESTIMATING THE ANGLE OF ARRIVAL AND DOPPLER FREQUENCY IN BISTATIC AND MULTISTATIC SYSTEMS

In this chapter, the angle of arrival (AoA) estimation problem is discussed from a purely sensing perspective. Bistatic and multistatic sensing network scenarios are investigated, in which both the sensing transmitter and the receiver(s) are equipped with multiple antennas. Assuming perfect synchronization among the transmitter and the receiver(s), this chapter addresses the joint estimation of the Doppler frequency and the angle of arrival of a passive target. The input to this estimation problem consists of noisy sensing signals collected over multiple time instances, while the output corresponds to the estimated angle of arrival and Doppler frequency, obtained either at each individual sensing node or at a hypothetical centralized processing entity. Within this general setting, the analysis evaluates how the estimation performance is affected by key system parameters, such as the number of receive APs and the number of available time samples. Numerical results show that the Cramér-Rao lower bound (CRLB) of the estimated parameters exhibits an inverse dependence on the number of time samples collected from the received echoes. Moreover, an even stronger inverse dependency is observed with respect to the number and spatial distribution of the receiver APs within the region of interest, highlighting the advantages of adopting a distributed MIMO (D-MIMO) architecture for sensing purposes.

3.1 Introduction

Radar systems (SKOLNIK, 2008) emerged in the 1930s and has advanced significantly, finding applications in civil and military sectors. Various radar implementations have been proposed, such as phased array radars (BROOKNER, 2002; BROOKNER, 2016), electronically steered arrays, and multiple-input multiple-output (MIMO) radars (FISHLER *et al.*, 2004). These radar technologies share similarities with communication networks, leading to the creation of the integrated communication and sensing (ISAC) field (WEI *et al.*, 2023), which aims to capitalize on common modules and features between communication and radar systems to merge the two technologies.

Both purely radar and ISAC networks share important similarities in their architectural design. In this context, ISAC networks inherit the well-established configuration models of classical radar systems, namely the monostatic, bistatic, and multistatic architectures (ZHANG *et al.*, 2022a).

The monostatic architecture (CUI; POLLIN, 2025) is the simplest in terms of imple-

mentation. In this configuration, the Tx and Rx are co-located, i.e., both functionalities reside within the same physical entity in the network. The bistatic architecture (LI *et al.*, 2024b), on the other hand, offers a higher degree of flexibility, at the cost of physically separating the Tx and Rx nodes. Finally, the multistatic architecture (BEHDAD *et al.*, 2024) can be understood as an evolution of the bistatic model, offering an even higher degree of flexibility by employing multiple physically separated Tx and Rx nodes. This architecture is particularly attractive for implementation in cell-free (distributed MIMO or user-centric) networks in the context of ISAC. Despite their differences, the fundamental radar functionality remains the same across all configurations: a probing signal is transmitted, and the environment is sensed by processing the echoes received from that signal.

Sensing-related services have gained significant attention in both industry and academia, particularly in the context of ISAC networks and in light of the forthcoming 6G. Although numerous sensing applications have long been established in the radar domain, two that are of particular relevance to ISAC are detection and target localization.

The detection, as the name suggests, consists in determining whether a target is present within a specified region of interest. Among the literature addressing this subject in the radar field, we refer to (GURUACHARYA *et al.*, 2021; TANG *et al.*, 2022; WEI *et al.*, 2022). Specifically in ISAC scenarios, recent advances include reliable detection in the presence of clutters (VINOGRADOVA; FODOR, 2023). Moreover, regarding the ISAC field, we refer to (SAKHNINI *et al.*, 2022; ZHANG *et al.*, 2022b; BEHDAD *et al.*, 2024). The practical limitation of detection in both radar and ISAC is that it cannot provide further information on the target's position, but only indicates the presence of a target within a specific region of interest. Thus, an additional application aligned with detection is needed to accurately determine the position of the target.

The target localization can be achieved by using the time of arrival (ToA), AoA and Doppler frequency measured from the echoes of a signal reflected by the target. The Doppler frequency being used to estimates the target's velocity. The information of AoA and the Doppler frequency itself has proven to be an efficient approach for achieving this goal. As expected, the accuracy of the estimation of these parameters has motivated some works to propose new estimation methods and improve the performance of existing ones, among which we refer to (BERGER *et al.*, 2010; RAHMAN *et al.*, 2020; BAIG *et al.*, 2023). Regarding the accuracy of the estimation process, one important and useful tool is the CRLB (KAY, 1993), which provides

a theoretical lower bound on the variance of any unbiased estimator.This bound serves as a benchmark for assessing the performance of estimation methods and provides insights into how a system behaves under various scenarios. In this context, we also refer to (STOICA; NEHORAI, 1989; FISHLER *et al.*, 2004).

In this chapter, under a LOS assumption, the performance of the joint estimation of the AoA and the Doppler frequency of a single moving target is compared for both bistatic and multistatic purely sensing network architectures.

In this context, the main contributions of this work can be summarized as follows:

- First, a framework for handling multiple observations acquired by multiple Rx APs is introduced to facilitate parameter estimation.
- Both bistatic and multistatic architectures were evaluated, and the respective CRLB equations were analytically derived. Additionally, these equations were reformulated for specific scenarios that have proven to be useful in understanding the overall system behavior, especially concerning sensing in D-MIMO systems.
- We numerically solve the ML estimator using the Newton-Raphson method to estimate the set of unknown parameters. Moreover, Monte Carlo simulations were used to compare its variance against the CRLB.

The remainder of this chapter is organized as follows: in Section 3.2, we offer a detailed description of the system model. Section 3.3 is dedicated to deriving the CRLB equations, starting from the bistatic architecture and extending to the multistatic one. Section 3.4 presents numerical results for a specified parameter setup. Finally, in Section 3.5, we discuss the conclusions drawn from this work.

3.2 System Model

In contrast with the communication-only perspective discussed in Chapter 2 regarding the AoA estimation problem, it is now explored under a purely sensing perspective. Although the reader may notice some similarities with the previous chapter in terms of the system model, a key difference is that dual polarization is not assumed in this analysis, as the sensing framework considered here relies solely on single-polarized transmission and reception.

Consider a single moving target located within the region covered by a multistatic sensing network. A single Tx AP, equipped with a ULA of M_T elements, is assumed to transmit sensing pilots (i.e., probing signals) while steering its Tx beam toward predefined directions

within a specified azimuth range. Additionally, K APs operating in Rx mode, each equipped with a ULA of M_R elements, are assumed to receive the echoes of the transmitted pilots reflected by the target. Furthermore, it is assumed that both Tx and Rx APs are equally distributed within the border of a circle of radius L as shown in Figure 24. Additionally, these APs are connected to a central processing unit (CPU), which handles the sensing processing tasks.

Figura 24 – Picture of a specific system model setup containing 3 APs.

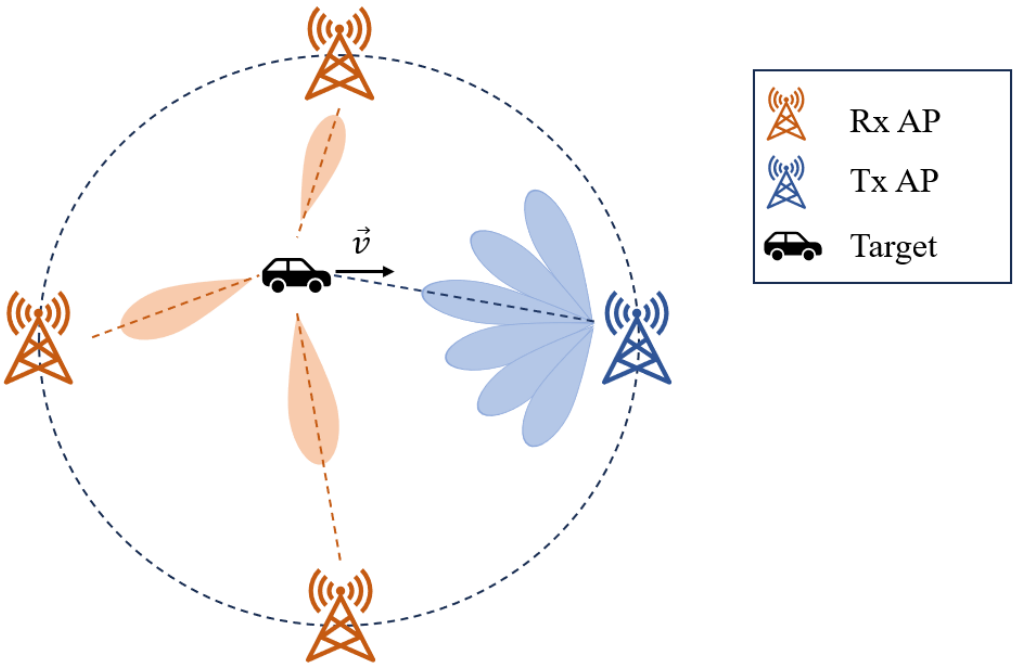

Source: Made by the author.

The content of this Chapter relies on the LOS assumption between the target and the APs, and it is also assumed that the AP-to-AP interference was resolved on a prior stage in the absence of the target. Therefore, we may describe the signal received at the k-th Rx AP at the n-th time instant, as it follows:

$$\mathbf{y}_k[n] = \mu_k[n] + \mathbf{z}[n] \in \mathbf{C}^{M_R \times 1}, \tag{3.1}$$

such that,

$$\mu_k[n] \triangleq \alpha_k e^{-j2\pi f_c \tau_k} e^{-j2\pi f_{D,k} n T_s} \mathbf{a}_R(\theta_k) \mathbf{a}_T(\phi)^T \mathbf{s}[n], \tag{3.2}$$

where α_k stands for the square root of the received power observed at the k-th Rx AP, f_c stands for the carrier frequency, $f_{D,k}$ stands for the bistatic Doppler shift observed at the k-th Rx AP,

T_s stands for the sampling period, $\mathbf{a}_R(\theta_k) \in \mathbf{C}^{M_R \times 1}$ is the Rx steering vector defined in terms of the AoA regarding the *k-th* Rx AP, $\mathbf{a}_T(\phi) \in \mathbf{C}^{M_T \times 1}$ is the Tx steering vector defined in terms of the AoD, and $\mathbf{s}[n] \triangleq \mathbf{f}[n]x[n] \in \mathbf{C}^{M_T \times 1}$ where $\mathbf{f}[n] \in \mathbf{C}^{M_T \times 1}$ and $x[n]$ are the transmit beamforming vector and the transmitted symbol at the *n-th* time instant, respectively. The time measurements are assumed to be obtained within a coherence block, such that $\{\alpha_k, \theta_k, \phi, \tau_k, f_{D,k}\}$ can be assumed to be quasi-constant, for all k.

3.3 Cramér-Rao Lower Bound

Proposition 3.3.1. *Assuming a bistatic network architecture, let $\mathbf{y}_0[n] \in \mathbb{C}^{M_R \times 1}$ be the reflected echo observed at the n-th time instant. The CRLB equations for a given set of unknown parameters $\{f_{D,0}, \theta_0\}$ can be analytically derived collecting multiple time observations at the Rx-side, i.e,*

$$\mathbf{y}_0 \triangleq \mu_0 + \mathbf{z}_0 \in \mathbb{C}^{NM_R \times 1}, \tag{3.3}$$

such that,

$$\mu_0 \triangleq \begin{bmatrix} \mu_0[N]^T & \dots & \mu_0[1]^T \end{bmatrix}^T \in \mathbb{C}^{NM_R \times 1}, \tag{3.4}$$

is a deterministic contribution accounting for the collected noise-less received signals, and

$$\mathbf{z}_0 \triangleq \begin{bmatrix} z_0[N]^T & \dots & z_0[1]^T \end{bmatrix}^T \in \mathbb{C}^{NM_R \times 1}, \tag{3.5}$$

accounts for the collected noise contributions, given that, $[\mathbf{z}_0]_i \sim \mathscr{CN}(0, \sigma_z^2)$, with $i = 1, \dots, NM_R$.

Proof. From Eq. (3.3), we can infer that the PDF of $\mathbf{y}_0$ is a non-zero mean complex Gaussian, i.e, $\mathbf{y}_0 \sim \mathscr{CN}(\mu_0, \sigma_z^2 \mathbf{I}_{NM_R})$, given that the noise is Gaussian. We may, therefore, calculate the CRLB from the FIM as it is described in Appendix A, which leads to:

$$\sigma^2_{\hat{f}_{D,0}} \geq \frac{1}{2(2\pi T_s)^2 \left[\sum_{n=1}^{N} n^2 \gamma_0[n] - \frac{3(M_R-1)\left(\sum_{n=1}^{N} n\gamma_0[n]\right)^2}{2(2M_R-1)\left(\sum_{n=1}^{N} \gamma_0[n]\right)} \right]}, \tag{3.6}$$

and

$$\sigma^2_{\hat{\theta}_0} \geq \frac{1}{\frac{1}{3}(\pi \cos\theta_0)^2 (2M_R-1)(M_R-1)} \frac{1}{\left[\sum_{n=1}^{N} \gamma_0[n] - \frac{3(M_R-1)\left(\sum_{n=1}^{N} n\gamma_0[n]\right)^2}{2(2M_R-1)\left(\sum_{n=1}^{N} n^2\gamma_0[n]\right)} \right]}, \tag{3.7}$$

where, $\gamma_0[n] \triangleq \frac{\|\mu_0[n]\|^2}{\sigma_z^2}$ is the signal-to-noise ratio (SNR) measured at the Rx AP at time instant n.

Proposition 3.3.2. *Assuming a multistatic network architecture, let* $\mathbf{y}_k[n] \in \mathbb{C}^{M_r \times 1}$ *be the echo observed at the n-th time instant, at the k-th Rx AP. If we use the local coordinate system of one of those Rx APs as the reference coordinate system of the APs network, we can derive the CRLB equations for the set of unknown parameters associated with the target at this coordinate system,* $\{f_{D,r}, \theta_r\}$*, by rewriting the set of unknown parameters measured at the k-th Rx AP,* $\{f_{D,k}, \theta_k\}$*, as:*

$$\begin{aligned} f_{D,k} &= f_{D,r} + \varphi_k, \\ \theta_k &= \theta_r + \vartheta_k, \end{aligned} \tag{3.8}$$

for all k, and by additionally collecting multiple time observations from all of the Rx APs at a hypothetical CPU, i.e,

$$\mathbf{y} \triangleq \mu + \mathbf{z} \in \mathbb{C}^{KNM_R \times 1}, \tag{3.9}$$

such that,

$$\mu \triangleq \begin{bmatrix} \mu_0^T & \dots & \mu_r^T & \dots & \mu_{K-1}^T \end{bmatrix}^T \in \mathbb{C}^{KNM_R \times 1}, \tag{3.10}$$

is a deterministic contribution accounting for the collected noise-less received signals of all Rx AP, where:

$$\mu_k \triangleq \begin{bmatrix} \mu_k[N]^T & \dots & \mu_k[1]^T \end{bmatrix}^T \in \mathbb{C}^{NM_R \times 1}, \tag{3.11}$$

for all k. Moreover,

$$\mathbf{w} \triangleq \begin{bmatrix} \mathbf{w}_0^T & \dots & \mathbf{w}_r^T & \dots & \mathbf{w}_{K-1}^T \end{bmatrix}^T \in \mathbb{C}^{KNM_R \times 1}, \tag{3.12}$$

accounts for the collected noise contributions, where:

$$\mathbf{w}_k \triangleq \begin{bmatrix} \mathbf{w}_k[N]^T & \dots & \mathbf{w}_k[1]^T \end{bmatrix}^T \in \mathbb{C}^{NM_R \times 1}, \tag{3.13}$$

for all k, given that $[\mathbf{w}]_i \sim \mathscr{CN}(0, \sigma_w^2)$*, with* $i = 1, \dots, KNM_R$*.*

Proof. Similarly to what was observed in the bistatic scenario, from Eq. (3.9) it can be infered that the PDF of $\mathbf{y}$ is a non-zero mean complex Gaussian vector, i.e, $\mathbf{y} \sim \mathscr{CN}(\mu, \sigma_w^2 \mathbf{I}_{KNM_R})$, given that the noise is Gaussian. Thus, we can derive the analytical CRLB expressions for the reference set of parameters according to the development described in Appendix B, which leads to Eq. (3.14) and Eq. (3.15).

$$\sigma^2_{\hat{f}_{D,r}} \geq \frac{1}{2(2\pi T_s)^2} \frac{1}{\left[\sum_{k=0}^{K-1}\sum_{n=1}^{N} n^2\gamma_k[n] - \frac{3(M_R-1)\left(\sum_{k=0}^{K-1}\cos\theta_k \sum_{n=1}^{N} n\gamma_k[n]\right)^2}{2(2M_R-1)\sum_{k=0}^{K-1}\cos^2\theta_k \sum_{n=1}^{N}\gamma_k[n]}\right]}, \tag{3.14}$$

$$\sigma^2_{\hat{\theta}_r} \geq \frac{1}{\frac{1}{3}\pi^2(M_R-1)(2M_R-1)} \frac{1}{\left[\sum_{k=0}^{K-1}\cos^2\theta_k \sum_{n=1}^{N}\gamma_k[n] - \frac{3(M_R-1)\left(\sum_{k=0}^{K-1}\cos\theta_k \sum_{n=1}^{N} n\gamma_k[n]\right)^2}{2(2M_R-1)\sum_{k=0}^{K-1}\sum_{n=1}^{N} n^2\gamma_k[n]}\right]}. \tag{3.15}$$

where $\gamma_k[n] \triangleq \frac{\|\mu_k[n]\|^2}{\sigma_z^2}$ is the SNR measured at the *k-th* Rx AP at time instant n. Moreover, it is evident that these equations reduce to Eq. (3.6) and Eq. (3.7) for $K = 1$.

Note that it is also possible to use the individual estimates obtained for each Rx AP to obtain the set of parameters for a reference AP, but this is not within the scope of this work. Upon obtaining the equations for the CRLB for both bistatic and D-MIMO architectures, the next logical step in our discussion is to compare their respective performances based on these equations. However, this is not a trivial task, as the D-MIMO architecture equations display a strong dependence on the AoAs observed at each Rx AP with regard to their local coordinate system, as evidenced by Eq. (3.14) and Eq. (3.15).

A possible approach is to assume that the target is positioned at the center of the considered circular region, which aligns with the assumption of a circular radar cross section (RCS). This approach, in turn, ensures that the bistatic path loss and, consequently, the sensing SNR observed at each Rx AP would be the same, $\gamma_k[n] = \gamma_r[n]$. Moreover, if it is also assumed that the target and the Tx AP are on the x-axis and with a 0° angle between them, it can be shown that

$$\left(\sum_{k=0}^{K-1}\cos\theta_k\right)^2 = 1, \ \sum_{k=0}^{K-1}\cos\theta_k{}^2 = \frac{K}{2} - \frac{1}{2}, \tag{3.16}$$

which are valid for $K > 2$. Thus, we may rewrite Eq. (3.14) and Eq. (3.15) as follows:

$$\sigma^2_{\hat{f}_{D,r}} \geq \frac{K-1}{4(2\pi T_s)^2} \frac{1}{\left[\frac{K(K-1)}{2}\sum_{n=1}^{N} n^2\gamma_r[n] - \frac{3(M_R-1)\left(\sum_{n=1}^{N} n\gamma_r[n]\right)^2}{2(2M_R-1)\left(\sum_{n=1}^{N}\gamma_r[n]\right)}\right]}, \tag{3.17}$$

and

$$\sigma^2_{\hat{\theta}_r} \geq \frac{K}{\frac{1}{3}\pi^2(2M_R-1)(M_R-1)} \frac{1}{\left[\frac{K(K-1)}{2}\sum_{n=1}^{N}\gamma_r[n] - \frac{3(M_R-1)\left(\sum_{n=1}^{N} n\gamma_r[n]\right)^2}{2(2M_R-1)\left(\sum_{n=1}^{N} n^2\gamma_r[n]\right)}\right]}. \tag{3.18}$$

Based on the equations discussed above, it can be inferred that an increase in the number of APs would lead to a reduction in the variances obtained from the CRLB.

3.4 Numerical results

This section presents and discusses some numerical results used to evaluate the asymptotic behavior of the CRLB for the set of unknown parameters across predefined setups. In the first set of results, the position of the target is fixed at the center of the circular region delimited by the APs. Additionally, we evaluate the variance of an ML estimator against the theoretical variance given by the CRLB. A summary of the parameters setup used to generate these results is presented in Table 3.

Tabela 3 – NUMERICAL RESULTS' PARAMETERS SETUP.

Parameter	**Value**
Delimited region radius L [m]	150
Number of Rx APs	[1, 3, 5, 9, 11]
Rx ULA length M_{R}	10
Tx ULA length M_{T}	10
Tx transmit power P_{tx} [dBm]	30
Noise figure [dB]	9
Carrier frequency f_{c} [GHz]	1.9
Bandwidth [MHz]	20
Sampling period T_{s} [μs]	0.71
Target speed $\vec{v}$ [km/h]	60
Target RCS [m^2]	π
Path loss model	Two-way radar equation (bistatic)
Antenna element radiation pattern	(3GPP, 2019)
Number of frequency-multiplexed symbols	12

Source: Elaborated by the author.

We first compare the CRLBs by fixing the number of Rx antennas at each AP for both bistatic and multistatic architectures while increasing the available time samples of the received echoes at each AP.

From Figure 25 and Figure 26, two observations must be discussed in further detail. First, one expects that the CRLB decreases as we increase the available time samples, which is validated by the results. Second, increasing the available Rx APs leads to a smaller CRLB for both parameters. This result is consistent with equations Eq. (3.17) and Eq. (3.18), and it can also be verified from Figure 27 and Figure 28. These figures plot the CRLB curves, fixing the number of available time samples to 400, while varying the number of Rx APs.

It is worth noting that based on the curves presented in Figure 26 and Figure 28, the

Figura 25 – Curve of the CRLB regarding the AoA.

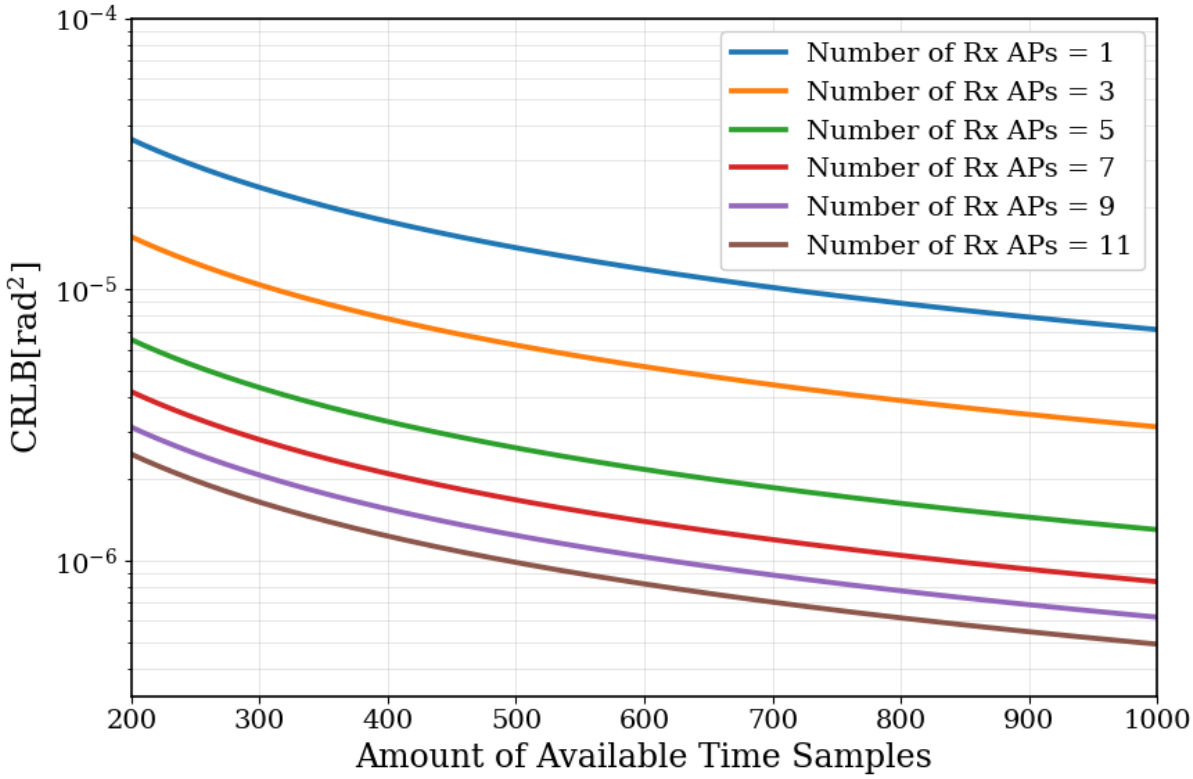

Source: Made by the author.

Figura 26 – Curve of the CRLB regarding the f_D.

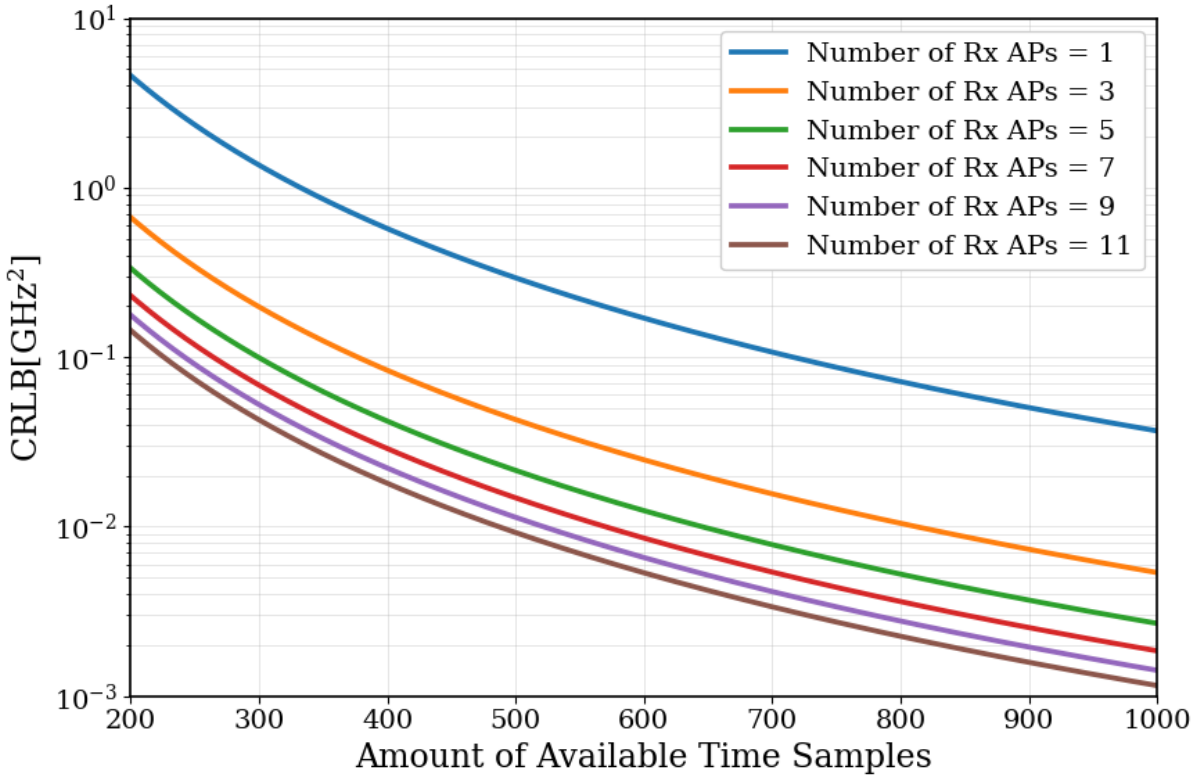

Source: Made by the author.

Figura 27 – Numerical results that illustrate the influence of the number of Rx APs on the CRLB, regarding the AoA estimation.

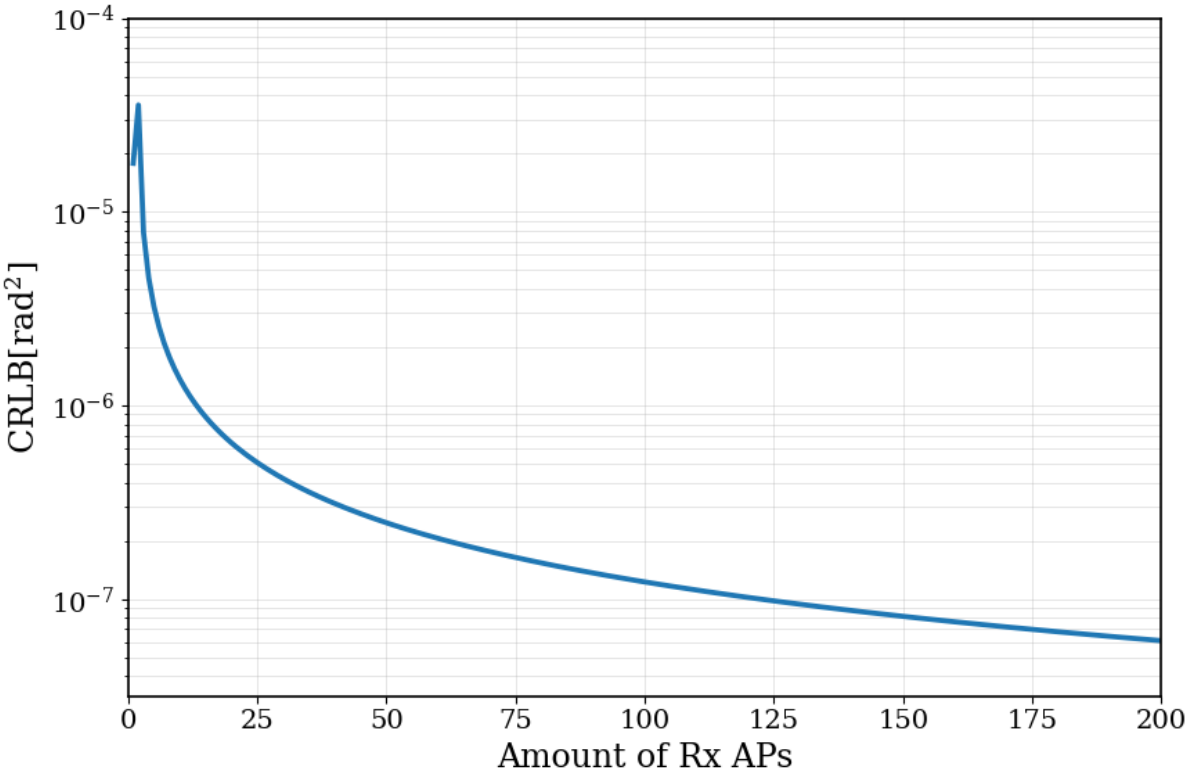

Source: Made by the author.

CRLB for the Doppler shift decreases at a slower rate than the CRLB for AoA. This phenomenon is due to the sampling period, which is a near-zero value on the denominator of Eq. (3.17). As a result, the other multiplicative term in the denominator of this equation must be very large to produce a significant decrease in CRLB. It is important to mention that varying the the position of the target within the area delimited by the Rx APs can potentially give rise to different values for the CRLB. However, it is reasonable to assume that trend of the asymptotic behaviors with respect to the number of antennas and time samples remains intact, albeit with some scaling factors.

In the last set of numerical results, the ML estimator was used to jointly estimate the AoA and the Doppler frequency using the Newton-Raphson method. We conducted 10000 Monte Carlo simulations while varying the available time samples. For each set of time samples, the variance of the ML estimator was computed and subsequently compared with the theoretical CRLB. Due to computational limitations, only the bistatic architecture was evaluated, with $M_R = M_T = 2$.

As it can be seen from Figure 29 and Figure 30, the variance of the ML estimator gets very close to that of the CRLB. This not only confirms the accuracy of the CRLB equations

Figura 28 – Numerical results that illustrate the influence of the number of Rx APs on the CRLB, regarding the Doppler Frequency estimation.

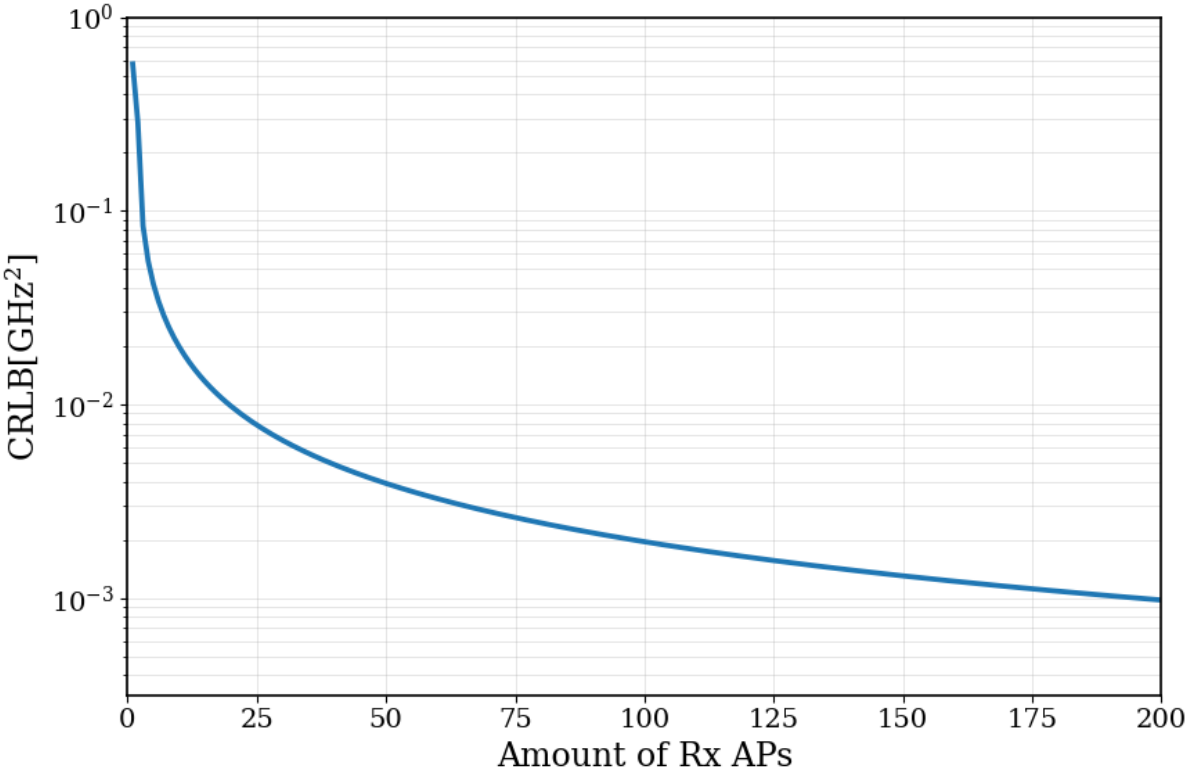

Source: Made by the author.

but also demonstrates that these equations provide a good approximation for the asymptotic performance of parameter estimation.

3.5 Conclusion

In this chapter, we discussed and evaluated the joint AoA and Doppler frequency estimation for a single passive moving target, assuming both bistatic and multistatic sensing scenarios. We initially derived the CRLB equations for both network architectures. Then, we gave special attention to the equations derived for the multistatic architecture and studied two ideal but beneficial use cases. We conducted numerical comparisons to evaluate the estimation performance, comparing a multistatic network with a bistatic one.

We studied the asymptotic behavior of the CRLB equations while varying the number of Rx APs and the amount of available time samples. Our numerical results indicate that increasing these parameters improve the estimation performance. However, they also show that the improvements tend to saturate after a certain point. Furthermore, we compared the empirical variance of ML estimation with the variance provided by the CRLB, and our results indicate that

Figura 29 – Numerical results that illustrate the influence of the number of Rx APs on the CRLB regarding the AoA.

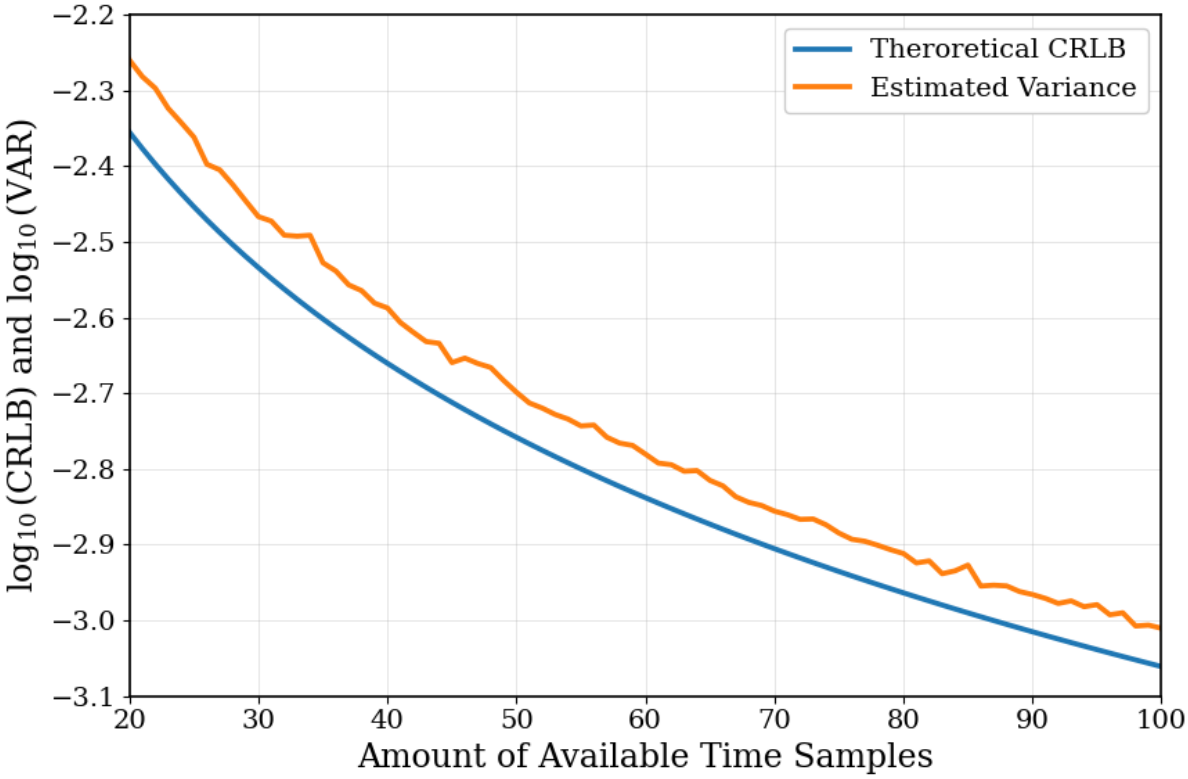

Source: Made by the author.

the behavior of this estimator is well represented by the closed-form CRLB equations.

We plan to expand the development described in this work to include ISAC networks in order to assess the impact of communication on estimation performance. Additionally, we are interested in exploring a multi-target scenario to understand how the estimation performance would be affected as we increase the number of passive targets in our system. Furthermore, we aim to relax the LOS assumption by considering a multi-scatterer system to allow for refined modeling of the propagation environment.

Figura 30 – Numerical results that illustrate the influence of the number of Rx APs on the CRLB regarding the Doppler Frequency.

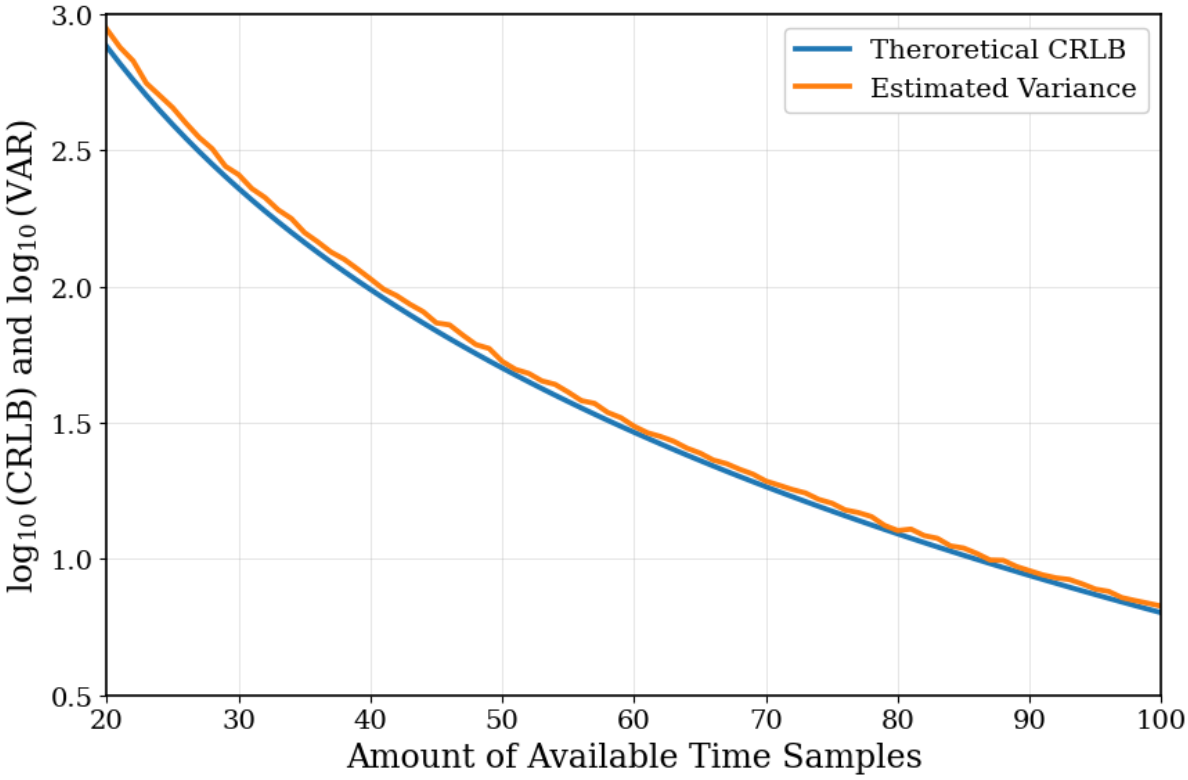

Source: Made by the author.

4 SPACE-TIME RESOURCE ALLOCATION FOR JOINT CRLB AND COMMUNICATION RATE OPTIMIZATION

Recent studies in the integrated communication and sensing (ISAC) literature that aim to enhance QoS through the optimization of specific key performance indicators (KPIs), such as the Cramér-Rao lower bound (CRLB) or the achievable sum rate, have primarily focused on power allocation strategies. In contrast, this chapter exploits the intrinsic space–time dependency of network resources to jointly improve the performance of both communication and sensing services. In this context, a bistatic ISAC network is considered, consisting of two access points that simultaneously serve multiple users in the downlink while sensing a passive target. By exploiting the relationship between the communication sum rate and the CRLB for the angles of arrival and departure, a convex optimization framework is proposed to jointly enhance the QoS of both functionalities through the allocation of space–time resources to regions of interest within the sensing area. Simulation results demonstrate significant performance improvements over conventional baseline strategies.

4.1 Introduction

The relevance of ISAC networks is rapidly growing in the context of 6G, driven by ongoing academic and industrial efforts to realize their full potential as an enabling technology. ISAC networks are designed to support the coexistence of communication and sensing services within a shared network infrastructure, enabling efficient utilization of hardware and spectral resources. From the sensing perspective, target localization has recently attracted significant attention among the various functionalities enabled by this technology.

As established in the existing ISAC literature, estimating parameters such as the angle of arrival (AoA) and the angle of departure (AoD) constitutes a fundamental step toward determining the target position within a predefined search region. Consequently, the overall localization accuracy is inherently tied to the precision achieved in AoA/AoD estimation. Therefore, it is essential that the estimators conceived for these parameters provide the most accurate estimates possible. To address this challenge, prior works have focused not only on proposing robust estimation techniques but also on improving existing ones, as shown in (BERGER *et al.*, 2010; RAHMAN *et al.*, 2020; BAIG *et al.*, 2023).

Within the context of parameter estimation, classical estimation theory (TREES, 2004) establishes that the accuracy of an estimator is intimately related to its variance. As the

variance increases, greater fluctuations of the estimated parameter around its true value are observed. It is therefore desirable for the estimator to have the smallest possible variance. In this regard, as stated in Chapter 1, the CRLB defines a theoretical lower bound on the variance achievable by any unbiased estimator.

For this reason, the CRLB is commonly used to evaluate and benchmark estimation techniques (KAY, 1993; LIU *et al.*, 2022), thereby providing key insights into system performance under varying conditions. Its application to sensing-related problems has been extensively investigated in works such as (STOICA; NEHORAI, 1989; FISHLER *et al.*, 2004). From a QoS perspective, minimizing the CRLB is highly desirable, as it directly reflects improvements in estimation accuracy and, consequently, in sensing performance. In this regard, recent contributions such as (XIONG *et al.*, 2023) and (LIU *et al.*, 2024) are particularly relevant and will be briefly reviewed below.

In (XIONG *et al.*, 2023), the authors investigate the fundamental limits of ISAC by analyzing the intrinsic trade-off between communication capacity and the CRLB associated with sensing performance. They introduce the concept of a CRLB–rate region that represents all achievable pairs of communication rates and sensing accuracies, and characterize its boundary by determining the maximum communication rate attainable under the minimum CRLB, and vice versa.

Finally, in (LIU *et al.*, 2024), the authors propose a novel parametric scattering model for sensing extended targets in concurrent-mode ISAC systems, where communication and sensing occur simultaneously using multibeam transmission. They first derive the CRLB for the unknown parameters and subsequently develop a beamforming design algorithm that minimizes the CRLB while satisfying both communication SINR and power constraints.

This chapter considers a bistatic ISAC network in which an AP operates as a Tx node that simultaneously serves multiple UEs in the downlink while sensing a single passive target. The echoes reflected from the target are received and processed by another AP operating in the Rx mode. Both APs are assumed to be connected to a central central processing unit (CPU). In contrast to previous studies in the literature, this chapter aims to enhance the QoS in terms of the CRLB of the target's AoA/AoD and the communication time-averaged sum rate, subject to suitable space–time resource allocation constraints. Under the LOS assumption, following (BEHDAD *et al.*, 2024), we analyze the impact of space–time resource management on the estimation of AoA and AoD using the CRLB, as well as on the communication performance

measured by the time-averaged sum rate. Furthermore, we formulate a convex optimization problem to allocate space–time resources among target sensing service areas (TSSAs) surrounding the Tx node (3GPP, 2024).

The main contributions disposed in this chapter can be summarized as follows:

- The CRLB equations for the target's AoA and AoD estimates are analytically derived from samples of the received echo signals at the Rx node.
- The expression of the communication time-averaged sum rate is analytically derived, as well, from the individual SINR expressions for each UE.
- We show that both the CRLB and the time-averaged sum rate are affected by the target's position and by the sensing time allocated to sweeping the sensing beam across the angular sector in which the target is located. Motivated by this property, the area surrounding the Tx is partitioned into equal-width TSSAs. A specific sensing time block is then assigned to each TSSA, which we refer to as the sensing space–time resource.
- Subsequently, we formulate a convex optimization problem that aims to properly allocate space-time resources per TSSA to enhance QoS of both communication and sensing services in terms of time-averaged sum rate and CRLB.

The remainder of this Chapter is organized as follows. Section 4.2 details the system model. Section 4.3 derives the CRLB, and Section 4.4 presents the time-averaged sum rate derivation at the UE side. Section 4.5 formulates the time resource allocation optimization problem. Section 4.6 provides numerical results. Finally, Section 4.7 summarizes the conclusions of this work.

4.2 System Model

At this point, the reader may have noticed that the previous chapters were organized in a storytelling manner. In Chapter 2, angle estimation was addressed in the context of a purely communication-oriented network. In Chapter 3, the estimation problem was examined within a sensing network. Finally, in this chapter, these two perspectives are unified, culminating in the analysis of the problem from the standpoint of ISAC networks. Consequently, the system model considered in this chapter must account for the specific characteristics of both sensing and communication signal modeling.

In this context, we consider a bistatic ISAC network comprising two APs: one operating in the Tx mode, serving K single-antenna UEs in the downlink while simultaneously

sensing a single passive target, and another operating in the Rx mode, which receives the target echoes together with residual interference from the communication counterpart.

The Tx AP is equipped with a ULA of N antenna elements and transmits distinct symbols $s_k[t]$ to each UE using dedicated precoders $\mathbf{w}_k$, while simultaneously steering a sensing beam toward predefined directions by employing a time-varying sensing precoder $\mathbf{w}_s[t]$ associated with the sensing symbol $s_0[t]$. The Rx AP, in turn, is equipped with a ULA of M elements and is connected to the Tx AP through a central CPU, as illustrated in Fig. 31. LOS conditions

Figura 31 – System model illustration.

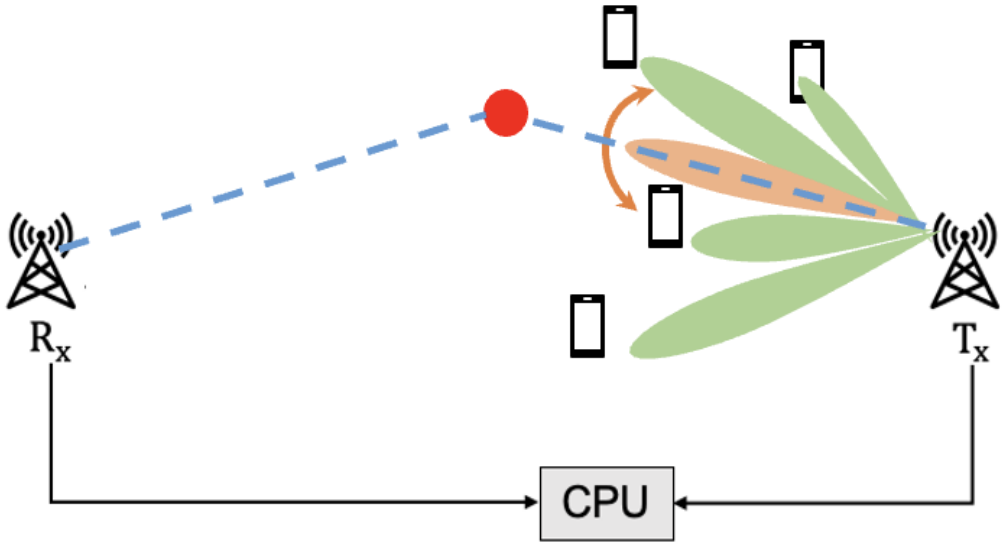

Source: Made by de author.

are assumed between the target and the APs. Moreover, it is also assumed that the AP-to-AP interference is resolved beforehand in the absence of targets. We further assume unit-power symbols, i.e., $|s_k[t]|^2 = 1$ for all $k \in \{0, 1, \ldots, K\}$, and let $\mathbf{s}[t] \in \mathbb{C}^{(K+1)\times 1}$ denote the symbol vector comprising K UE symbols and the sensing symbol $s_0[t]$.

4.2.1 Communication signal

From a communication perspective, the UEs act as Rx nodes, collecting time samples of superimposed communication and sensing signals. Thus, the signal received by the k-th UE at

the t-th time instant is given by:

$$y_k[t] = \sqrt{\rho_k}\mathbf{h}_k^T\mathbf{w}_k[t]s_k[t] + \sum_{i\neq k}\sqrt{\rho_i}\mathbf{h}_k^T\mathbf{w}_i[t]s_i[t] + \sqrt{\rho_0}\mathbf{h}_k^T\mathbf{w}_s[t]s_0[t] + z_c[t], \tag{4.1}$$

where $\mathbf{h}_k \in \mathbb{C}^{N\times 1}$ denotes the channel between the Tx-AP and the k-th UE, and $z_c[t] \sim \mathscr{CN}(0,\sigma_c^2)$ represents additive white Gaussian noise. The communication channels are modeled as Rayleigh fading channels, where large-scale effects, including path loss and average antenna gains, are absorbed into the channel variance. The term ρ_k denotes the transmit power allocated to the k-th UE, while ρ_0 corresponds to the sensing signal power. The communication channel is assumed to be perfectly known at the Tx-AP and constant over the transmission block.

4.2.2 Sensing signal

The sensing signal received at the Rx AP at the t-th time instant is given by

$$\mathbf{y}[t] = \sqrt{\rho_0}\alpha\mathbf{a}_R(\theta)\mathbf{a}_T(\phi)^T\mathbf{W}[t]\mathbf{s}[t] + \mathbf{z}_s[t], \tag{4.2}$$

where $\mathbf{W}[t] = \begin{bmatrix}\mathbf{w}_s[t] & \mathbf{w}_1 & \dots & \mathbf{w}_K\end{bmatrix} \in \mathbb{C}^{N\times(K+1)}$ is the precoding matrix, α is the reflection coefficient of the k-th target, $\mathbf{a}_R(\theta_k) \in \mathbb{C}^{M\times 1}$ is the Rx steering vector defined in terms of the angle of arrival (AoA) θ, and $\mathbf{a}_T(\phi_k) \in \mathbb{C}^{N\times 1}$ is the Tx steering vector defined in terms of the angle of departure (AoD) ϕ.

4.3 Time-Averaged Sum Rate

The scenario considered in this chapter shares system-level similarities with the one presented in (BEHDAD *et al.*, 2022). Consequently, the communication SINR expression adopted in that reference can be readily extended to the scenario investigated here. In this setting, the signal received at the k-th UE experiences interference from both the beams directed toward other UEs and the time-varying sensing beam. As a result, the communication SINR $\gamma_k[t]$ becomes time-dependent and is given by

$$\gamma_k[t] = \frac{\rho_k|\mathbf{h}_k^T\mathbf{w}_k|^2}{\sum_{i\neq k}\rho_i|\mathbf{h}_k^T\mathbf{w}_i|^2 + \rho_0|\mathbf{h}_k^T\mathbf{w}_s[t]|^2 + \sigma_c^2}, \tag{4.3}$$

where the term $\sum_{i\neq k}\rho_i|\mathbf{h}_k^T\mathbf{w}_i|^2$ accounts for the inter-UE interference, $\rho_0|\mathbf{h}_k^T\mathbf{w}_s[t]|^2$ represents the time-dependent sensing beam interference, and σ^2 denotes the noise power.

In this context, the corresponding instantaneous sum rate can be expressed in bits/s/Hz, and is given by

$$R[t] = \sum_{k=1}^{K} \log_2 \left(1 + \gamma_k[t]\right). \tag{4.4}$$

It is important to mention that, a detailed discussion of Tx power allocation strategies is beyond the scope of this chapter. Therefore, we assume that the Tx power is allocated such that an equal amount of power is assigned to each UE and to the sensing function, i.e, $\rho_k = \rho = \frac{P_{Tx}}{K+1}$ for all $k = 0, \ldots, K$.

The impact of the interference caused by sweeping the sensing beam across a given angular range on the communication sum rate is illustrated in Figure 32. In this example, we

Figura 32 – Instantaneous sum rate versus sensing beam steering angle. Peaks and valleys result from constructive and destructive interference between the sensing and communication beams, respectively.

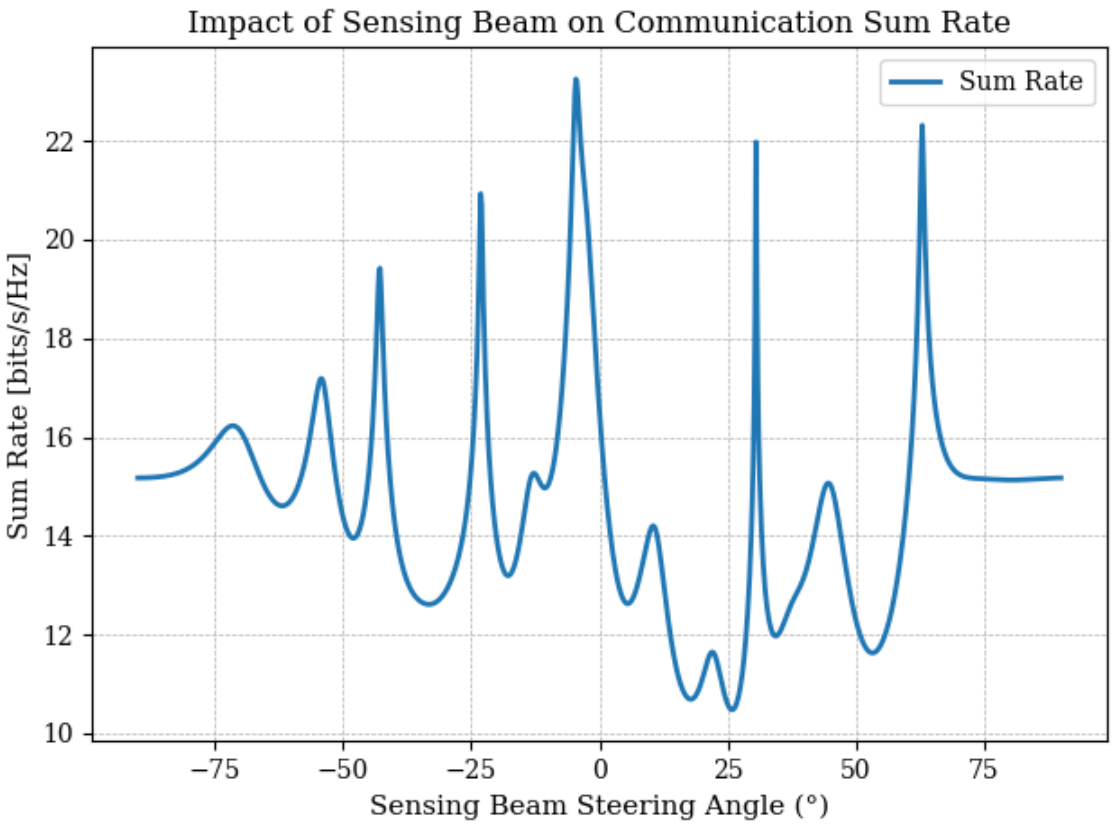

Source: Made by de author.

assume a hypothetical scenario with four UEs randomly positioned within a region of interest. A zero-forcing (ZF) precoder is applied to steer beams toward the UEs, while the sensing beam is sequentially swept across a fixed angular range, targeting one direction at a time. As shown in Figure 32, the plot exhibits peaks and valleys at specific directions, caused by interference

between the sensing and communication beams. Moreover, Figure 33 presents the beam pattern variations when the sensing beam is steered toward different directions. From this figure, it can

Figura 33 – Polar beam patterns: top-left shows the communication-only beam; others show the combined pattern with the sensing beam at $-30°$, $0°$, and $30°$.

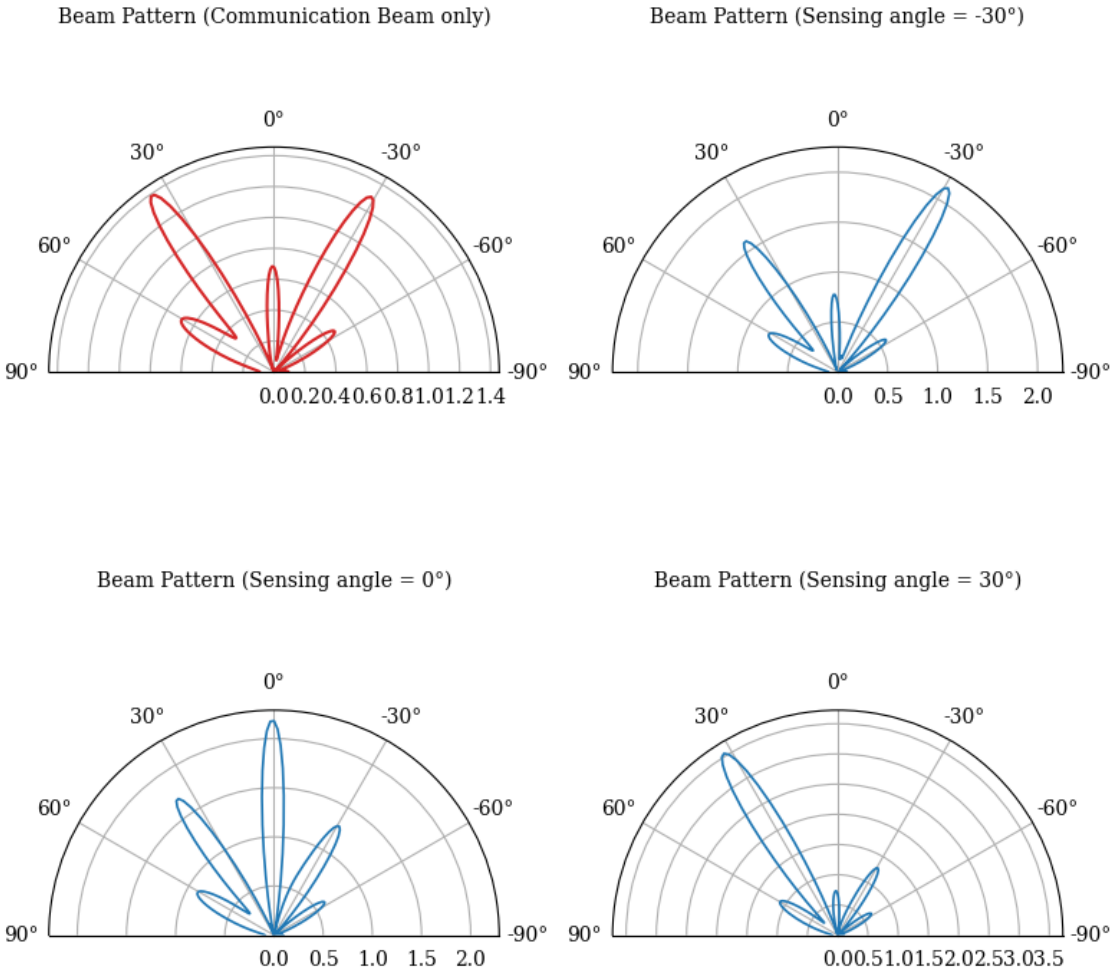

Source: Made by de author.

be inferred that valley regions occur due to destructive interference between the sensing and communication beams, which lowers the array factor over certain directions. In contrast, peak regions result from constructive interference, leading to a maximized array response.

In this context, if we regard the sum rate from a time-average perspective,

$$\bar{R} = \frac{1}{T_s} \sum_{t=1}^{T_s} R[t], \tag{4.5}$$

the broader the peak regions are, the higher the time-averaged sum rate will be. In other words, spending more time sweeping the sensing beam within a peak region translates into improvements

in the average communication rate. Conversely, allocating more time to sweeping the sensing beam within a valley region can significantly degrade the overall communication performance.

It is important to note that these peak and valley regions are not fixed; they depend on the communication and sensing beam shapes, the spatial arrangement of targets and UEs, and the allocation of time resources across directions.

4.4 Cramér-Rao Lower Bound

As previously discussed in this chapter, target localization in ISAC networks relies on accurate estimation of the AoA and AoD, and the resulting localization performance is closely related to the precision of these parameter estimates.

In the context of the estimation task, the CRLB (KAY, 1993) provides a fundamental benchmark by establishing a theoretical lower bound on the variance of any unbiased estimator. It is widely used to assess estimation performance and to evaluate how different system configurations influence estimation accuracy.

Let $\xi = \{\theta, \phi\}$ be the set of deterministic, but unknown parameters. If an unbiased estimator $\hat{\xi}$ exists, then its covariance matrix must satisfy the following inequality:

$$\mathrm{Cov}(\hat{\xi}) \succeq \mathbf{F}^{-1}, \tag{4.6}$$

where $\mathbf{F}$ denotes the FIM (KAY, 1993), obtained from the likelihood function $p_{\mathbf{y}}(\mathbf{y};\xi)$ of the observation vector $\mathbf{y} \in \mathbb{C}^{T_s M \times 1}$, which collects the T_s measurements $\mathbf{y}[t]$, and is expressed as follows:

$$\mathbf{F} = E\left\{ \frac{\partial \ln p_{\mathbf{y}}(\mathbf{y};\xi)}{\partial \xi} \frac{\partial \ln p_{\mathbf{y}}(\mathbf{y};\xi)}{\partial \xi^H} \right\}. \tag{4.7}$$

Accordingly, the FIM is structured as

$$\mathbf{F} = \begin{bmatrix} F_\theta & F_{\theta,\phi} \\ F_{\theta,\phi} & F_\phi \end{bmatrix}. \tag{4.8}$$

For the scenario considered in this chapter, and recalling the received signal in Eq. (4.2), the likelihood function $p_{\mathbf{y}}(\mathbf{y};\xi)$ can be expressed as:

$$p_{\mathbf{y}}(\mathbf{y};\xi) = \frac{1}{(\pi\sigma^2)^{T_s N}} \exp\left(-\frac{1}{\sigma^2} \sum_{i=0}^{T_s N-1} |[\mathbf{y}]_i - [\mu(\xi)]_i|^2 \right), \tag{4.9}$$

given that $\mathbf{z}[t] \sim \mathscr{CN}(\mathbf{0}, \sigma^2 \mathbf{I}_M)$, where $\mu \in \mathbb{C}^{T_s M \times 1}$ denotes the deterministic contribution to the measurement vector $\mathbf{y}$.

Thus, the FIM can be described in an element-wise representation as shown in Eq. (4.10):

$$
\begin{aligned}
F_{\theta} &= \sum_{t=1}^{T_s} \frac{2(\pi\cos\theta)^2}{\sigma^2} \sum_{m=0}^{M-1} m^2 \left|\alpha\, \mathbf{a}_T(\phi)^T \mathbf{W}[t]\mathbf{s}[t]\right|^2, \\
F_{\theta,\phi} &= \sum_{t=1}^{T_s} \frac{2\pi^2\cos\theta\cos\phi}{\sigma^2} \sum_{m=0}^{M-1} m\,\alpha^2\, \mathrm{Re}\Big\{ \big(\mathbf{a}_T(\phi)^T \mathbf{W}[t]\mathbf{s}[t]\big)^* \big(\mathbf{a}_T(\phi)^T \mathbf{D}_m \mathbf{W}[t]\mathbf{s}[t]\big) \Big\}, \\
F_{\phi} &= \sum_{t=1}^{T_s} \frac{2(\pi\cos\phi)^2}{\sigma^2} \sum_{m=0}^{M-1} \left|\alpha\, \mathbf{a}_T(\phi)^T \mathbf{D}_m \mathbf{W}[t]\mathbf{s}[t]\right|^2.
\end{aligned}
\tag{4.10}
$$

where $\mathbf{D}_m \triangleq \mathrm{diag}([0,1,\ldots,m,\ldots,M-1]^T) \in \mathbb{C}^{M\times M}$. Furthermore, by substituting Eq. (4.10) into Eq. (4.8), and noting that all entries of $\mathbf{F}$ share the same summation indices over the receive antennas and time instants, the FIM can be written as a sum of T_s time-indexed matrices $\mathbf{F}[t] \in \mathbb{C}^{2\times 2}$, given by:

$$
\mathbf{F} = \sum_{t=1}^{T_s} \mathbf{F}[t] = \sum_{t=1}^{T_s} \begin{bmatrix} F_{\theta}[t] & F_{\theta,\phi}[t] \\ F_{\theta,\phi}[t] & F_{\phi}[t] \end{bmatrix}. \tag{4.11}
$$

where,

$$
\begin{aligned}
F_{\theta}[t] &\triangleq \frac{2(\pi\cos\theta)^2}{\sigma^2} \sum_{m=0}^{M-1} m^2 \left|\alpha\, \mathbf{a}_T(\phi)^T \mathbf{W}[t]\mathbf{s}[t]\right|^2, \\
F_{\theta,\phi}[t] &\triangleq \frac{2\pi^2\cos\theta\cos\phi}{\sigma^2} \sum_{m=0}^{M-1} m\,\alpha^2\, \mathrm{Re}\Big\{ \big(\mathbf{a}_T(\phi)^T \mathbf{W}[t]\mathbf{s}[t]\big)^* \big(\mathbf{a}_T(\phi)^T \mathbf{D}_m \mathbf{W}[t]\mathbf{s}[t]\big) \Big\}, \\
F_{\phi}[t] &\triangleq \frac{2(\pi\cos\phi)^2}{\sigma^2} \sum_{m=0}^{M-1} \left|\alpha\, \mathbf{a}_T(\phi)^T \mathbf{D}_m \mathbf{W}[t]\mathbf{s}[t]\right|^2.
\end{aligned}
\tag{4.12}
$$

The CRLB for each unknown parameters, AoA and AoD, is obtained from the main diagonal entries of the inverse FIM, $\mathbf{F}^{-1}$, which follow the same ordering as F_{θ} and F_{ϕ} in Eq. (4.10). It can be observed that both the FIM and, consequently, the CRLB exhibit a space–time dependence. This dependence is governed by the number of available time samples, the target position, expressed through its AoA and AoD, and the number of Rx antennas.

4.5 Time Resources Allocation

As discussed in the previous sections, both spatial and temporal factors influence the time-averaged sum rate and the CRLB. As mentioned in Section 4.3 and illustrated in Figure 32, minimizing the time spent sweeping through valley regions can improve the time-averaged sum

rate. Moreover, due to the space–time dependence of the CRLB, improving the rate does not necessarily reduce the estimation error. This motivates the need for a joint optimization of spatial and temporal resources.

To exploit this dependency, the search area of the Tx and Rx APs was segmented into predefined search regions. Specifically, a hypothetical circle centered at the Tx AP is divided into L equal-width angular sectors, referred to as TSSAs. Figure 34 illustrates this sectorization approach. This allows the total search time T_s to be divided into sub-blocks $T_{s,l}$, each assigned

Figura 34 – Illustration of the TSSA sectorization.

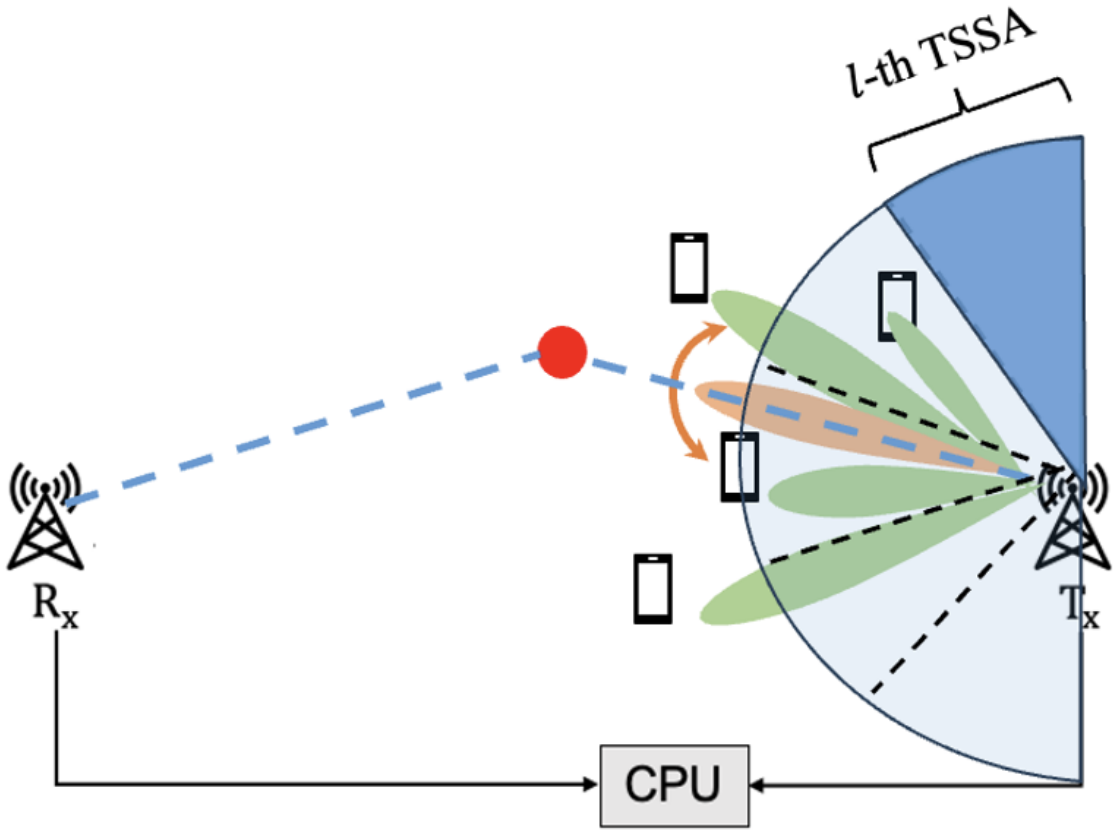

Source: Made by the author.

to the l-th TSSA based on system needs, with $l = 1,\ldots,L$. Due to the non-uniform target distribution, tailored time allocation can enhance resource efficiency.

Furthermore, to explicitly isolate the space–time dependency of the KPIs of interest, it is assumed that, during the time assigned to each TSSA, the sensing beam remains fixed and points toward the center of that sector. As a consequence, $\mathbf{W}[t] = \mathbf{W}_l$ for all $t \in T_{s,l}$ and $l = 1,\ldots,L$. Additionally, a global phase rotation is assumed between consecutive time instants, such that $\mathbf{s}[t+1] = e^{j\beta}\mathbf{s}[t]$, where β denotes a constant phase shift. Thus $\mathbf{W}_l\mathbf{s}[t+1] = e^{j\beta}\mathbf{W}_l\mathbf{s}[t]$

within each TSSA. Under these assumptions, from Eq. (4.5) and Eq. (4.10), the average rate and the FIM can be expressed as follows:

$$\begin{aligned}\bar{R} &= \frac{1}{T_s}\sum_{t=1}^{T_s} R[t] = \frac{1}{T_s}\sum_{l=1}^{L} T_{s,l} R_l, \\ \mathbf{F} &= \sum_{t=1}^{T_s} \mathbf{F}[t] = \sum_{l=1}^{L} T_{s,l}\mathbf{F}_l.\end{aligned} \tag{4.13}$$

Proposition 4.5.1. *Assume that the search region is partitioned into L TSSAs. Let $T_{s,l}$ denote the sensing time block during which the sensing beam is swept within the l-th TSSA. By efficiently allocating the time blocks $T_{s,l}$ across all TSSAs, it is possible to enhance both communication and sensing QoS, in terms of the time-averaged sum rate and the CRLB.*

Thus, let $\mathbf{t} \in \mathbb{R}^{L\times 1}$ denote the time-allocation vector containing the L sensing blocks $T_{s,l}$, one for each TSSA. Likewise, let $\mathbf{r} \in \mathbb{R}^{L\times 1}$ denote the vector that collects the communication time blocks $T_{r,l}$ assigned to each sector. Additionally, let $\mathbf{F}_l \in \mathbb{C}^{K\times K}$ represent the FIM contribution from the l-th TSSA. Based on this formulation, the efficient space-time resources allocation is obtained by solving:

$$\begin{aligned}\max_{\mathbf{t}} \quad & 10\log_{10}\left(\frac{1}{T_s}\sum_{l=1}^{L} t_l R_l\right) \\ s.t. \quad & \mathrm{tr}\left\{\mathbf{F}^{-1}\right\} \le \varepsilon \cdot \mathrm{tr}\left\{\bar{\mathbf{F}}^{-1}\right\}, \\ & \mathbf{r}^T\mathbf{t} \ge \frac{1+\chi}{L}\cdot \mathbf{r}^T\mathbf{1}, \\ & \mathbf{t}^T\mathbf{1} = T_s, \\ & \mathbf{t} \succeq \mathbf{0}\end{aligned} \tag{4.14}$$

where $\bar{\mathbf{F}} \in \mathbb{C}^{K\times K}$ is the reference FIM computed from Eq. (4.5) *under uniform time resources allocation, i.e., $T_{s,l} = T_s/L$ for all l.*

Proof. From Eq. (4.5), the time-averaged sum rate $\bar{R}$ is a linear function of the time allocation vector $\mathbf{t} \in \mathbb{R}^{L\times 1}$, subject to the constraints $\mathbf{t}^T\mathbf{1} = T_s$ and $\mathbf{t} \succeq \mathbf{0}$. Although $\mathbf{t}$ is discrete by definition, we relax it to allow continuous, non-negative values to simplify the problem. This relaxation preserves linearity, implying that $\bar{R}$ remains both convex and concave.

Maximizing $10\log_{10}(\bar{R})$ is equivalent to maximizing $\bar{R}$, since $\log_{10}(\cdot)$ is strictly increasing. Furthermore, as $\bar{R} > 0$, this transformation yields a concave objective function with

respect to $\mathbf{t}$. Thus, the relaxed optimization problem can be initially written as:

$$\begin{aligned} \max_{\mathbf{t}} \quad & 10\log_{10}\left(\frac{1}{T_s}\sum_{l=1}^{L} T_{s,l}R_l\right), \\ \text{s.t.} \quad & \mathbf{t}^T\mathbf{1} = T_s. \end{aligned} \tag{4.15}$$

To enforce a performance bound on sensing accuracy, we introduce a constraint on the CRLB by exploiting the dependence of the FIM on the vector $\mathbf{t}$ described in and $\hat{\mathbf{F}}$, which denotes the FIM obtained assuming that $\mathbf{t} = \frac{T_s}{L}\mathbf{1}$, as follows:

$$\mathrm{tr}\{\mathbf{F}^{-1}\} \leq \varepsilon \cdot \mathrm{tr}\{\bar{\mathbf{F}}^{-1}\}, \tag{4.16}$$

where ε is a user-defined tolerance factor. The proof of the convexity of this constraint is shown in the Appendix C.

Additionally, we impose a minimum performance requirement on the communication rate:

$$\mathbf{r}^T\mathbf{t} \geq \frac{1+\chi}{L} \cdot \mathbf{r}^T\mathbf{1}, \tag{4.17}$$

where $(1+\chi)$ defines the minimum acceptable rate increase over the uniform baseline.

With these constraints, the resulting optimization problem in Eq. (4.14) is convex, as it maximizes a concave objective under convex constraints, completing the proof. □

4.6 Numerical Results

In this section, the performance gains achieved through the optimized space–time resource allocation across the L TSSAs are evaluated in terms of the time-averaged sum rate and the CRLB of the target AoA and AoD. This optimization problem was introduced in Section 4.5 and aims to efficiently allocate the available space-time resources among the L TSSAs. It was shown that this problem is convex and was solved using the sequential linear-quadratic programming (SLSQP) algorithm. This algorithm was selected due to practical limitations of standard convex solvers in expressing the constraint defined in (4.16) as a convex constraint.

For simulation purposes, it is assumed that the sensing Rx node is positioned at the point $(0,0)$, while the Tx node is positioned at the point $(L,0)$, where $L = 250\,\mathrm{m}$. The position of the passive target is drawn from a set of uniformly distributed points within a sector of a ring with an inner radius of $30\,\mathrm{m}$ and an outer radius of $50\,\mathrm{m}$, delimited by an angular range comprising the angles between 90° and 270°. Similarly, the position of the UEs is drawn from a

set of uniformly distributed points within a sector of a ring with an inner radius of 100 m and an outer radius of 150 m, delimited by an angular range varying from 90° to 270°.

As discussed previously, it is assumed that the Tx beam is steered toward the central angles of $L = 6$, equal-width angular TSSAs. For this simulation setup, the central angles are chosen to be $\{-75°, -45°, -15°, 15°, 45°, 75°\}$. Additionally, a summary of the parameter setup is presented in Table 4.

Tabela 4 – SIMULATION PARAMETER SETUP.

Parameter	Value
Rx node position	$(0,0)$
Tx node position	$(250\text{ m}, 0)$
Target distance from Tx [m]	Uniform in $[30, 50]$
UE distance from Tx [m]	Uniform in $[100, 150]$
Number of angular TSSAs L	6
TSSA central angles [deg]	$\{-75, -45, -15, 15, 45, 75\}$
Total number of time instants T_s	540
Tx antenna array size M	8
Rx antenna array size N	4
Tx transmit power P_{tx} [dBm]	60
Carrier frequency f_c [GHz]	1.9
Bandwidth [MHz]	20
Noise figure [dB]	9
Target RCS [m^2]	1
Path loss model	Two-way bistatic radar equation
Antenna radiation pattern	3GPP TR 38.901

Source: Elaborated by the author.

We compare the performance proposal against two benchmark scenarios. In the first, *equal time allocation*, the space–time resources are uniformly distributed among all TSSAs. In the second, *random beam*, equal time is assigned to each TSSAs, while within each sector the sensing beam is steered towards a random direction at every time instant.

In the first set of results, all parameters were fixed except for the number of UEs. 100 Monte Carlo simulations were performed by varying the target positions, and for each target position, an additional 100 simulations varied the UEs positions. In each run, the time-averaged sum rate and the CRLB were computed, averaged over the inner simulations, and then across the 100 outer simulations.

The results of the Monte Carlo simulations for the CRLB and time-averaged sum rate are shown in Figure 35 and Figure 36, respectively. As seen in Figure 35, the CRLB increases nearly linearly with the number of UEs, reflecting degraded AoA/AoD estimation due to stronger interference. Moreover, the proposal outperforms the benchmarks, highlighting the

Figura 35 – CRLB curves

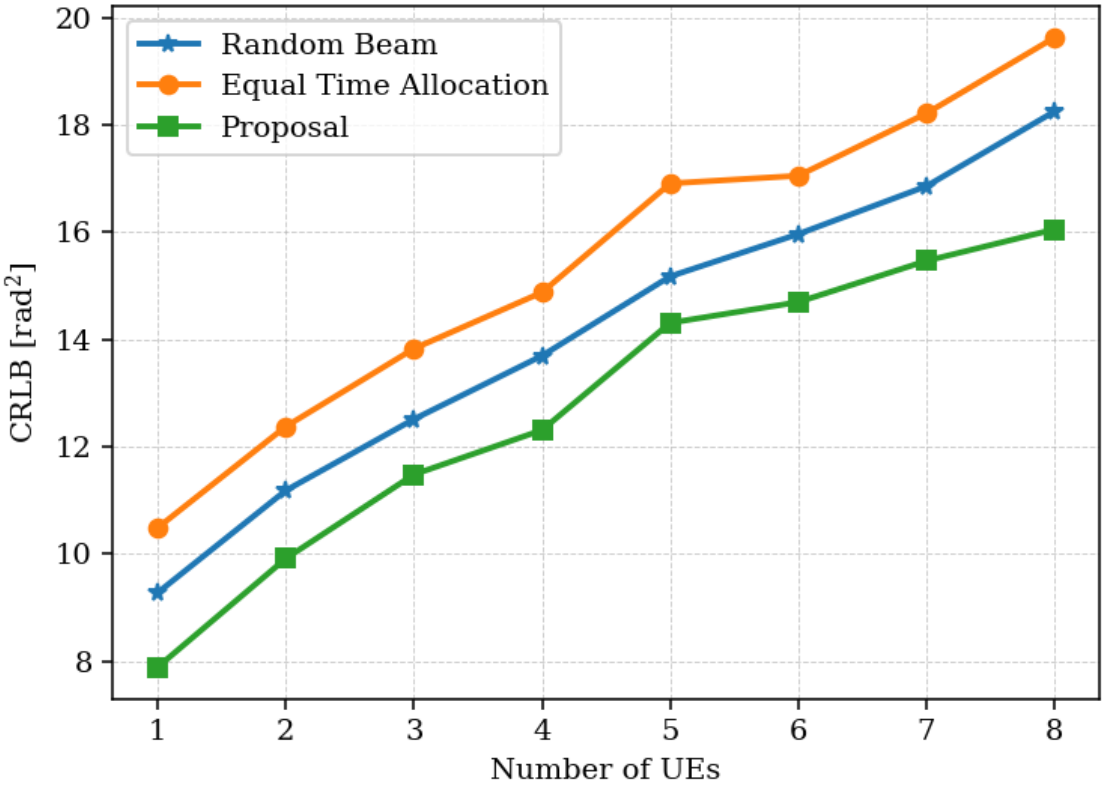

Source: Made by de author.

benefits of optimized space–time resource allocation.

Figure 36 shows that the time-averaged sum rate increases with the number of UEs until reaching a maximum at 6 UEs, after which it declines rapidly. This trend is explained by two opposing effects. Initially, multi-user diversity enhances channel utilization. However, as the number of UEs continues to grow, resource constraints and increased interference become predominant, leading to a reduction in performance. As it can also be seen, the proposal has outperformed the benchmarks, leading to the highest time-averaged sum rate values.

These numerical results show that the *random beam* technique yields the lowest time-averaged sum rate, since the sensing beam is steered to random angles within each TSSA at every instant, causing unpredictable interference with communication beams and degrading performance. In contrast, with regard to the CRLB, the numerical results exhibit an intermediate performance when compared to the two other solutions. This can be explained by the fact that the sensing beam may occasionally align with directions that improve estimation accuracy. Furthermore, the *equal time allocation* technique leads to an intermediate performance in terms of time-averaged sum rate, while leading to the worst performance in terms of the CRLB.

Figura 36 – Time-averaged sum rate curves.

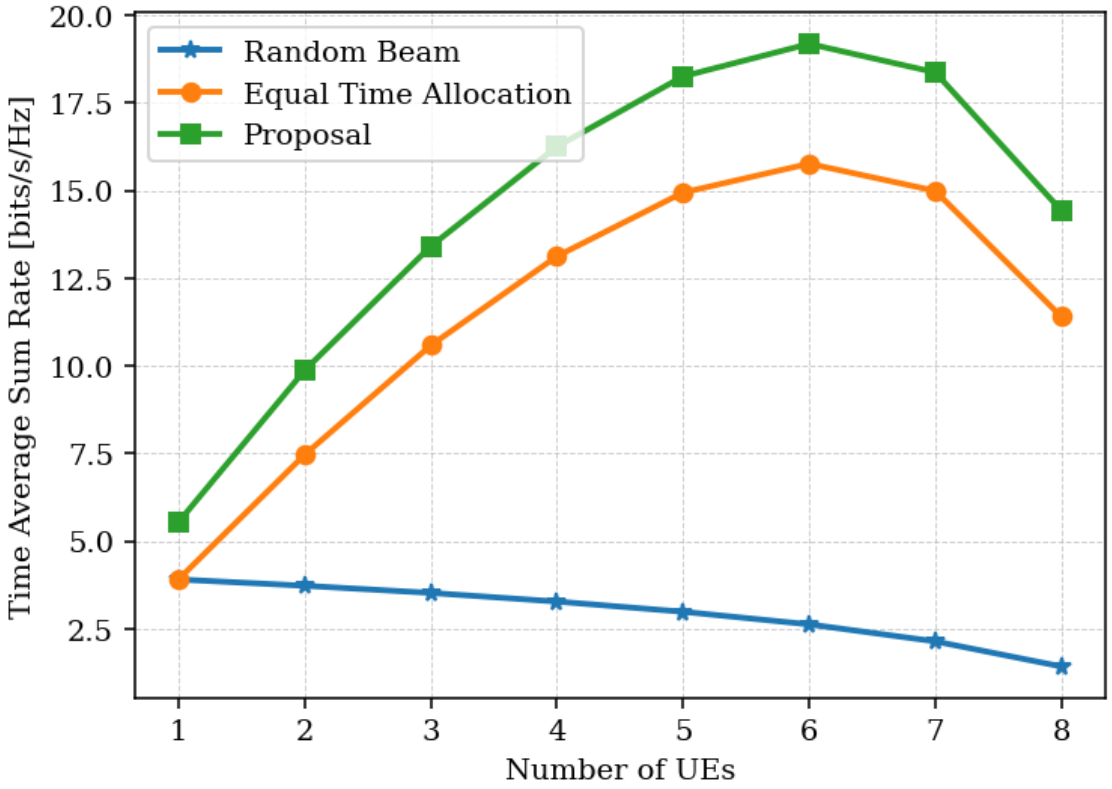

Source: Made by de author.

4.7 Conclusions

This work revisited the estimation of a target's AoA and AoD in a bistatic ISAC network serving multiple UEs while sensing a single passive target in the downlink, analyzing its impact on the communication time-averaged sum rate. To enhance both sensing and communication performance, the search area was sectorized into TSSAs, and an optimization problem was formulated to maximize the sum rate under a CRLB constraint through optimized space–time resource allocation.

Monte Carlo simulations were conducted to evaluate the CRLB and the time-averaged sum rate under the proposed allocation method and two benchmark scenarios, while varying the number of UEs. The numerical results highlight the performance gains of the proposed method. and shed light on the practical aspects imposed by an increasing number of UEs.

Future work will extend this framework to a multistatic setting to exploit angle estimation from multiple perspectives within the proposed optimization problem. In addition, we plan to relax the LOS assumption by incorporating clutter, enabling more realistic modeling

of the propagation environment.

5 CONCLUSIONS

As the title of this PhD thesis suggests, this document proposes to study and evaluate the problem of AoA estimation from three distinct yet complementary perspectives, namely: a purely communication perspective, a purely sensing perspective, and an ISAC perspective. In this context, Chapter 1 provided a detailed overview of the fundamental concepts necessary for a comprehensive understanding of the main theme of this thesis. This chapter was structured to trace the lineage from statistical foundations to the consolidation of estimation theory; subsequently, it introduced the basics of array signal processing and, finally, discussed the concept of user-centric cell-free networks.

The first of these perspectives, namely the purely communication perspective, was addressed in Chapter 2. Considering a MIMO communication system composed of a Tx/Rx pair operating in high-frequency bands, a novel AoA estimation method was proposed by exploiting diversity in the polarization domain. To this end, the proposed algorithm requires only a single polarization-multiplexed transmission, which makes it an attractive alternative to existing methods. Simulation results indicate that the proposed method achieves performance comparable to an 8-long beam-sweeping procedure, while requiring eight times less signaling.

In Chapter 3, the AoA estimation problem was examined from a purely sensing perspective. Considering both bistatic and multistatic sensing networks, this chapter discussed and evaluated the joint estimation of AoA and Doppler frequency, assuming a single passive target. The individual CRLB expressions were derived for both architectures, with the goal of providing a visualization tool to assess the asymptotic behavior of the estimator performance when varying the number of Rx APs and the number of available time samples. The numerical results indicate significant performance improvements as these parameters increase; however, such improvements tend to saturate beyond a certain point. Furthermore, empirical results obtained using the ML algorithm confirmed that the theoretical behavior predicted by the CRLB was indeed satisfied.

Finally, in Chapter 4, the AoA estimation problem is discussed from an ISAC perspective. Assuming a bistatic ISAC network that serves multiple UEs while simultaneously sensing a single passive target, a strategy was proposed to enhance both sensing and communication performance. This chapter introduces an approach to maximize the communication time-averaged sum rate under a CRLB-based constraint, where the CRLB is computed in terms of the AoA and AoD estimates, through optimized space–time resource allocation. To this

end, the search area was vectorized into TSSAs, and the key idea was to efficiently assign space–time resources to each TSSA to achieve performance improvements. Furthermore, the numerical results obtained through Monte Carlo simulations highlight the performance gains of the proposed method and shed light on the practical limitations imposed by an increasing number of UEs.

5.1 Future Works

In light of the discussions presented throughout this document, particularly in the context of ISAC, there are several directions for possible future investigation. Some of these directions can be summarized as follows:

- The scenarios evaluated in the previous chapters assumed that both the Tx and Rx nodes were equipped with ULAs. Consequently, due to the inherent structure of the ULA, only one angular dimension, either the zenith or the azimuth, can be estimated, depending on the array's orientation. In this context, extending these works to consider uniform rectangular arrays (URAs) can significantly enhance target localization capabilities by enabling the joint estimation of both zenith and azimuth angles.
- Angle estimation, and consequently, target localization, does not need to be interpreted as a final product. Instead, these estimates can be leveraged to generate detailed 3D representations of the environment. Therefore, extending this work to consider imaging as the final product appears to be a natural next step.
- Machine learning and artificial intelligence represent promising tools, in the context of ISAC. In terms of applicability, they can be employed not only for target localization but also for target detection. Moreover, sensing-oriented imaging applications can benefit from well-established solutions from the machine learning and computer vision literature, like visual transformers, and convolutional neural network architectures.

These directions represent of course a sample, among a large gamma of exciting possibilities for future ISAC networks.

REFERENCES

3GPP. *TR 38.901: Study on channel model for frequencies from 0.5 to 100 GHz*. [S.l.], 2019. Disponível em: <https://www.3gpp.org/ftp/Specs/archive/38_series/38.901/38901-h00.zip>.

3GPP. *TS 38.211: NR; Physical channels and modulation*. [S.l.], 2022. Disponível em: <https://www.3gpp.org/ftp/Specs/archive/38_series/38.211/38211-h10.zip>.

3GPP. *TR 22837: "Feasibility Study on Integrated Sensing and Communication"*. [S.l.], 2024.

AHMED, I.; KHAMMARI, H.; SHAHID, A. Resource allocation for transmit hybrid beamforming in decoupled millimeter wave multiuser-MIMO downlink. **IEEE Access**, v. 5, p. 170–182, 2017.

AHMED, I.; KHAMMARI, H.; SHAHID, A.; MUSA, A.; KIM, K. S.; POORTER, E. D.; MOERMAN, I. A survey on hybrid beamforming techniques in 5G: Architecture and system model perspectives. **IEEE Communications Surveys Tutorials**, v. 20, n. 4, p. 3060–3097, 2018.

AL-HOURANI, A. On the probability of line-of-sight in urban environments. **IEEE Wireless Communications Letters**, v. 9, n. 8, p. 1178–1181, 2020.

ALI, E.; ISMAIL, M.; NORDIN, R.; ABDULAH, N. F. Beamforming techniques for massive MIMO systems in 5G: overview, classification, and trends for future research. **Frontiers of Information Technology & Electronic Engineering**, Springer, v. 18, n. 6, p. 753–772, 2017.

AMMAR, H. A.; ADVE, R. Power delay profile in coordinated distributed networks: User-centric v/s disjoint clustering. In: **2019 IEEE Global Conference on Signal and Information Processing (GlobalSIP)**. [S.l.: s.n.], 2019. p. 1–5.

AMMAR, H. A.; ADVE, R.; SHAHBAZPANAHI, S.; BOUDREAU, G.; SRINIVAS, K. V. User-centric cell-free massive MIMO networks: A survey of opportunities, challenges and solutions. **IEEE Communications Surveys Tutorials**, v. 24, n. 1, p. 611–652, 2022.

ANSELMI, N.; GOUDOS, S.; OLIVERI, G.; POLI, L.; ROCCA, P.; SALUCCI, M.; MASSA, A. Unconventional array architectures for next generation wireless communications. In: ____. **Sparse Arrays for Radar, Sonar, and Communications**. [S.l.: s.n.], 2024. p. 423–454.

ANTONIOLI, R. P.; BRAGA, I. M.; FODOR, G.; SILVA, Y. C.; FREITAS, W. C. Mixed coherent and non-coherent transmission for multi-CPU cell-free systems. In: **ICC 2023 - IEEE International Conference on Communications**. [S.l.: s.n.], 2023. p. 1068–1073.

ASPLUND, H.; KARLSSON, J.; KRONESTEDT, F.; LARSSON, E.; ASTELY, D.; BUTOVITSCH, P. von; CHAPMAN, T.; FRENNE, M.; GHASEMZADEH, F.; HAGSTRÖM, M. *et al.* **Advanced antenna systems for 5G network deployments: bridging the gap between theory and practice**. [S.l.]: Academic Press, 2020.

BAIG, M. U.; VINOGRADOVA, J.; FODOR, G.; MOLLEN, C. Joint communication and sensing beamforming for passive object localization. In: **WSA & SCC 2023; 26th International ITG Workshop on Smart Antennas and 13th Conference on Systems, Communications, and Coding**. [S.l.: s.n.], 2023. p. 1–6.

BALANIS, C. A. **Advanced engineering electromagnetics**. [S.l.]: John Wiley & Sons, 2012.

BEHDAD, Z.; DEMIR, T.; SUNG, K. W.; BJöRNSON, E.; CAVDAR, C. Power allocation for joint communication and sensing in cell-free massive MIMO. In: **GLOBECOM 2022 - 2022 IEEE Global Communications Conference**. [S.l.: s.n.], 2022. p. 4081–4086.

BEHDAD, Z.; DEMIR, T.; SUNG, K. W.; BJöRNSON, E.; CAVDAR, C. Multi-static target detection and power allocation for integrated sensing and communication in cell-free massive MIMO. **IEEE Transactions on Wireless Communications**, p. 1–1, 2024.

BERGER, C. R.; DEMISSIE, B.; HECKENBACH, J.; WILLETT, P.; ZHOU, S. Signal processing for passive radar using OFDM waveforms. **IEEE Journal of Selected Topics in Signal Processing**, v. 4, n. 1, p. 226–238, 2010.

BJORNSON, E.; JALDEN, N.; BENGTSSON, M.; OTTERSTEN, B. Optimality properties, distributed strategies, and measurement-based evaluation of coordinated multicell OFDMA transmission. **IEEE Transactions on Signal Processing**, v. 59, n. 12, p. 6086–6101, 2011.

BROOKNER, E. Phased array radars-past, present and future. In: **RADAR 2002**. [S.l.: s.n.], 2002. p. 104–113.

BROOKNER, E. Developments and breakthroughs in radars and phased-arrays. In: **2016 IEEE Radar Conference (RadarConf)**. [S.l.: s.n.], 2016. p. 1–6.

BUZZI, S.; I, C.-L.; KLEIN, T. E.; POOR, H. V.; YANG, C.; ZAPPONE, A. A survey of energy-efficient techniques for 5G networks and challenges ahead. **IEEE Journal on Selected Areas in Communications**, v. 34, n. 4, p. 697–709, 2016.

CRAMÉR, H.; LEADBETTER, M. R. **Stationary and related stochastic processes: Sample function properties and their applications**. [S.l.]: Courier Corporation, 2013.

CUI, Z.; POLLIN, S. Extracting the communication channel from monostatic sensing channels: From propagation to impact analysis. **IEEE Transactions on Antennas and Propagation**, v. 73, n. 8, p. 6193–6198, 2025.

DAHLMAN, E.; PARKVALL, S.; SKOLD, J. **4G: LTE/LTE-advanced for mobile broadband**. [S.l.]: Academic press, 2013.

DAHLMAN, E.; PARKVALL, S.; SKOLD, J.; BEMING, P. **3G evolution: HSPA and LTE for mobile broadband**. [S.l.]: Academic press, 2010.

DRAMPALOU, S. F.; UZUNIDIS, D.; VETSOS, A.; MIRIDAKIS, N. I.; KARKAZIS, P. A user-centric perspective of 6g networks: A survey. **IEEE Access**, v. 12, p. 190255–190294, 2024.

ELBIR, A. M.; MISHRA, K. V.; VOROBYOV, S. A.; HEATH, R. W. Twenty-five years of advances in beamforming: From convex and nonconvex optimization to learning techniques. **IEEE Signal Processing Magazine**, v. 40, n. 4, p. 118–131, 2023.

FENG, Z.; FANG, Z.; WEI, Z.; CHEN, X.; QUAN, Z.; JI, D. Joint radar and communication: A survey. **China Communications**, v. 17, n. 1, p. 1–27, 2020.

FISHLER, E.; HAIMOVICH, A.; BLUM, R.; CHIZHIK, D.; CIMINI, L.; VALENZUELA, R. MIMO radar: an idea whose time has come. In: **Proceedings of the 2004 IEEE Radar Conference (IEEE Cat. No.04CH37509)**. [S.l.: s.n.], 2004. p. 71–78.

GIRNYK, M. A.; PETERSSON, S. O. Efficient cell-specific beamforming for large antenna arrays. **IEEE Transactions on Communications**, v. 69, n. 12, p. 8429–8442, 2021.

GUO, F.; YU, F. R.; ZHANG, H.; LI, X.; JI, H.; LEUNG, V. C. M. Enabling massive IoT toward 6G: A comprehensive survey. **IEEE Internet of Things Journal**, v. 8, n. 15, p. 11891–11915, 2021.

GUO, Y.; ZHANG, Y.; WANG, Z.; LIU, Y. Wideband beamforming for near-field communications with circular arrays. **IEEE Transactions on Wireless Communications**, v. 23, n. 12, p. 19065–19082, 2024.

GURUACHARYA, S.; CHALISE, B. K.; HIMED, B. MAP ratio test detector for radar system. **IEEE Transactions on Signal Processing**, v. 69, p. 573–588, 2021.

HAYKIN, S. **Communication systems**. [S.l.]: John Wiley & Sons, 2008.

HIDA, T. **Stationary stochastic processes**. [S.l.]: Princeton University Press, 2015. v. 8.

ISHTEYAQ, I.; MUZAFFAR, K. Multiple input multiple output (MIMO) and fifth generation (5G): An indispensable technology for sub-6 GHz and millimeter wave future generation mobile terminal applications. **International Journal of Microwave and Wireless Technologies**, Cambridge University Press, v. 14, n. 7, p. 932–948, 2022.

JABEEN, N.; LEI, H.; MUHAMMAD, A.; ALI, A.; KHAN, Z. U.; PAN, G. Localization in ISAC: A review. **IEEE Internet of Things Journal**, v. 12, n. 22, p. 46526–46552, 2025.

JIANG, T.; SONG, L.; ZHANG, Y. **Orthogonal frequency division multiple access fundamentals and applications**. [S.l.]: CRC Press, 2010.

JIANG, W.; ZHOU, Q.; HE, J.; HABIBI, M. A.; MELNYK, S.; EL-ABSI, M.; HAN, B.; RENZO, M. D.; SCHOTTEN, H. D.; LUO, F.-L.; EL-BAWAB, T. S.; JUNTTI, M.; DEBBAH, M.; LEUNG, V. C. M. Terahertz communications and sensing for 6G and beyond: A comprehensive review. **IEEE Communications Surveys Tutorials**, v. 26, n. 4, p. 2326–2381, 2024.

KAY, S. M. **Fundamentals of statistical signal processing: estimation theory**. [S.l.]: Prentice-Hall, Inc., 1993.

KIM, S.; HAN, H.; KIM, N.; PARK, H. Robust beam tracking algorithm for mmWave MIMO systems in mobile environments. In: **2019 IEEE 90th Vehicular Technology Conference (VTC2019-Fall)**. [S.l.: s.n.], 2019. p. 1–5.

KOBAYASHI, H.; MARK, B. L.; TURIN, W. **Probability, random processes, and statistical analysis: applications to communications, signal processing, queueing theory and mathematical finance**. [S.l.]: Cambridge University Press, 2011.

KUTTY, S.; SEN, D. Beamforming for millimeter wave communications: An inclusive survey. **IEEE Communications Surveys Tutorials**, v. 18, n. 2, p. 949–973, 2016.

LI, H.; CHENG, Z. Angle-of-arrival estimation using difference beams in localized hybrid arrays. **Sensors**, v. 21, n. 5, 2021. ISSN 1424-8220. Disponível em: <https://www.mdpi.com/1424-8220/21/5/1901>.

LI, L.; CHEN, W.; CHEN, Z.; HU, T.; MEI, W.; NING, B. Enhancing terahertz communications coverage with ISAC-assisted beam management. **IEEE Wireless Communications**, v. 31, n. 1, p. 34–40, 2024.

LI, R.; XIAO, Z.; ZENG, Y. Toward seamless sensing coverage for cellular multi-static integrated sensing and communication. **IEEE Transactions on Wireless Communications**, v. 23, n. 6, p. 5363–5376, 2024.

LIU, A.; HUANG, Z.; LI, M.; WAN, Y.; LI, W.; HAN, T. X.; LIU, C.; DU, R.; TAN, D. K. P.; LU, J.; SHEN, Y.; COLONE, F.; CHETTY, K. A survey on fundamental limits of integrated sensing and communication. **IEEE Communications Surveys & Tutorials**, v. 24, n. 2, p. 994–1034, 2022.

LIU, D.; HAN, S.; YANG, C.; ZHANG, Q. Semi-dynamic user-specific clustering for downlink cloud radio access network. **IEEE Transactions on Vehicular Technology**, v. 65, n. 4, p. 2063–2077, 2016.

LIU, R.; SWINDLEHURST, A. L.; LI, M. Crb optimization using a parametric scattering model for extended targets in ISAC systems. **arXiv preprint arXiv:2411.00145**, 2024.

LU, S.; LIU, F.; LI, Y.; ZHANG, K.; HUANG, H.; ZOU, J.; LI, X.; DONG, Y.; DONG, F.; ZHU, J.; XIONG, Y.; YUAN, W.; CUI, Y.; HANZO, L. Integrated sensing and communications: Recent advances and ten open challenges. **IEEE Internet of Things Journal**, v. 11, n. 11, p. 19094–19120, 2024.

LUO, X.; LIN, Q.; ZHANG, R.; CHEN, H.-H.; WANG, X.; HUANG, M. ISAC – a survey on its layered architecture, technologies, standardizations, prototypes and testbeds. **IEEE Communications Surveys Tutorials**, p. 1–1, 2025.

LUO, X.; LIN, Q.; ZHANG, R.; CHEN, H.-H.; WANG, X.; HUANG, M. ISAC—a survey on its layered architecture, technologies, standardizations, prototypes, and testbeds. **IEEE Communications Surveys Tutorials**, v. 28, p. 485–526, 2026.

MISHRA, A. R. **Fundamentals of cellular network planning and optimisation: 2G/2.5G/3G... evolution to 4G**. [S.l.]: John Wiley & Sons, 2004.

NGO, H. Q.; INTERDONATO, G.; LARSSON, E. G.; CAIRE, G.; ANDREWS, J. G. Ultradense cell-free massive MIMO for 6G: Technical overview and open questions. **Proceedings of the IEEE**, v. 112, n. 7, p. 805–831, 2024.

NGO, H. Q.; TRAN, L.-N.; DUONG, T. Q.; MATTHAIOU, M.; LARSSON, E. G. On the total energy efficiency of cell-free massive MIMO. **IEEE Transactions on Green Communications and Networking**, v. 2, n. 1, p. 25–39, 2018.

PAPOULIS, A. **Random variables and stochastic processes**. [S.l.]: McGraw Hill, 1965.

PARZEN, E. On Estimation of a Probability Density Function and Mode. **The Annals of Mathematical Statistics**, Institute of Mathematical Statistics, v. 33, n. 3, p. 1065–1076, 1962. ISSN 00034851. Disponível em: <http://www.jstor.org/stable/2237880>.

PATEL, J. K.; READ, C. B. **Handbook of the normal distribution**. [S.l.]: CRC Press, 1996. v. 150.

PROAKIS, J. G.; SALEHI, M. **Digital communications**. [S.l.]: McGraw-hill New York, 2001. v. 4.

QIN, C.; ZHANG, J. A.; HUANG, X.; WU, K.; GUO, Y. J. Fast angle-of-arrival estimation via virtual subarrays in analog antenna array. **IEEE Transactions on Wireless Communications**, v. 19, n. 10, p. 6425–6439, 2020.

RAHMAN, M. L.; ZHANG, J. A.; HUANG, X.; GUO, Y. J.; HEATH, R. W. Framework for a perceptive mobile network using joint communication and radar sensing. **IEEE Transactions on Aerospace and Electronic Systems**, v. 56, n. 3, p. 1926–1941, 2020.

ROBEY, F.; FUHRMANN, D.; KOERBER, M. Array calibration and modeling of steering vectors. In: **Conference Record of Thirty-Fifth Asilomar Conference on Signals, Systems and Computers (Cat.No.01CH37256)**. [S.l.: s.n.], 2001. v. 2, p. 1121–1126 vol.2.

ROZANOV, Y. A. Stationary processes. **Fizmatgiz., Moskva.(English translation by A. Feinstein (1967), Holden-Day, San Francisco.)**, Springer, 1963.

SAKHNINI, A.; GUENACH, M.; BOURDOUX, A.; SAHLI, H.; POLLIN, S. A target detection analysis in cell-free massive MIMO joint communication and radar systems. In: **ICC 2022 - IEEE International Conference on Communications**. [S.l.: s.n.], 2022. p. 2567–2572.

SAQIB, N. U.; PARK, K.; SONG, H.-G.; JEON, S.-W. 3D hybrid beamforming with 2D planar antenna arrays for downlink massive MIMO systems. In: **2021 International Conference on Information and Communication Technology Convergence (ICTC)**. [S.l.: s.n.], 2021. p. 616–620.

SHAYEA, I.; ERGEN, M.; AZMI, M. H.; ÇOLAK, S. A.; NORDIN, R.; DARADKEH, Y. I. Key challenges, drivers and solutions for mobility management in 5G networks: A survey. **IEEE Access**, v. 8, p. 172534–172552, 2020.

SKOLNIK, M. I. (Ed.). **Radar Handbook**. 3rd. ed. New York, NY, USA: McGraw-Hill, 2008. Disponível em: <https://www.accessengineeringlibrary.com/content/book/9780071485470>.

SLOANE, W.; GENTILE, C.; SHAFI, M.; SENIC, J.; MARTIN, P. A.; WOODWARD, G. K. Measurement-based analysis of millimeter-wave channel sparsity. **IEEE Antennas and Wireless Propagation Letters**, v. 22, n. 4, p. 784–788, 2023.

SOHRABI, F.; YU, W. Hybrid digital and analog beamforming design for large-scale antenna arrays. **IEEE Journal of Selected Topics in Signal Processing**, v. 10, n. 3, p. 501–513, 2016.

SONG, H.-L.; NAM, S. S.; KO, Y.-C. Angle-of-arrival estimation technique for fast beamforming using monopulse signal in the antenna array systems. **IEEE Access**, v. 9, p. 95346–95359, 2021.

STOICA, P.; NEHORAI, A. Music, maximum likelihood, and Cramér-Rao bound. **IEEE Transactions on Acoustics, Speech, and Signal Processing**, v. 37, n. 5, p. 720–741, 1989.

SUN, G.; HOU, H.; WANG, Y.; WANG, W.; XU, W.; JIN, S. Beam-sweeping design for mmwave massive grant-free transmission. **IEEE Journal of Selected Topics in Signal Processing**, IEEE, 2024.

TABASSUM, H.; SALEHI, M.; HOSSAIN, E. Fundamentals of mobility-aware performance characterization of cellular networks: A tutorial. **IEEE Communications Surveys Tutorials**, v. 21, n. 3, p. 2288–2308, 2019.

TAN, J.; LUAN, T. H.; GUAN, W.; WANG, Y.; PENG, H.; ZHANG, Y.; ZHAO, D.; LU, N. Beam alignment in mmwave V2X communications: A survey. **IEEE Communications Surveys & Tutorials**, IEEE, v. 26, n. 3, p. 1676–1709, 2024.

TANG, X.; ZHANG, Z.; QIN, Y. On-road object detection and tracking based on radar and vision fusion: A review. **IEEE Intelligent Transportation Systems Magazine**, v. 14, n. 5, p. 103–128, 2022.

TATARIA, H.; SHAFI, M.; MOLISCH, A. F.; DOHLER, M.; SJöLAND, H.; TUFVESSON, F. 6g wireless systems: Vision, requirements, challenges, insights, and opportunities. **Proceedings of the IEEE**, v. 109, n. 7, p. 1166–1199, 2021.

TEZUKA, S. **Uniform random numbers: Theory and practice**. [S.l.]: Springer Science & Business Media, 2012. v. 315.

TREES, H. L. V. **Optimum array processing: Part IV of detection, estimation, and modulation theory**. [S.l.]: John Wiley & Sons, 2002.

TREES, H. L. V. **Detection, estimation, and modulation theory, part I: detection, estimation, and linear modulation theory**. [S.l.]: John Wiley & Sons, 2004.

VEEN, B. V.; BUCKLEY, K. Beamforming: a versatile approach to spatial filtering. **IEEE ASSP Magazine**, v. 5, n. 2, p. 4–24, 1988.

VINOGRADOVA, J.; FODOR, G. On target detection in the presence of clutter in joint communication and sensing cellular networks. In: **2023 16th International Conference on Signal Processing and Communication System (ICSPCS)**. [S.l.: s.n.], 2023. p. 01–10.

WANG, C.-X.; YOU, X.; GAO, X.; ZHU, X.; LI, Z.; ZHANG, C.; WANG, H.; HUANG, Y.; CHEN, Y.; HAAS, H.; THOMPSON, J. S.; LARSSON, E. G.; RENZO, M. D.; TONG, W.; ZHU, P.; SHEN, X.; POOR, H. V.; HANZO, L. On the road to 6G: Visions, requirements, key technologies, and testbeds. **IEEE Communications Surveys & Tutorials**, IEEE, v. 25, n. 2, p. 905–974, 2023.

WEI, Z.; QU, H.; WANG, Y.; YUAN, X.; WU, H.; DU, Y.; HAN, K.; ZHANG, N.; FENG, Z. Integrated sensing and communication signals toward 5G-A and 6G: A survey. **IEEE Internet of Things Journal**, v. 10, n. 13, p. 11068–11092, 2023.

WEI, Z.; ZHANG, F.; CHANG, S.; LIU, Y.; WU, H.; FENG, Z. Mmwave radar and vision fusion for object detection in autonomous driving: A review. **Sensors**, v. 22, n. 7, 2022. ISSN 1424-8220. Disponível em: <https://www.mdpi.com/1424-8220/22/7/2542>.

XIAO, Z.; CHEN, S.; ZENG, Y. Simultaneous multi-beam sweeping for mmwave massive MIMO integrated sensing and communication. **IEEE Transactions on Vehicular Technology**, v. 73, n. 6, p. 8141–8152, 2024.

XIONG, Y.; LIU, F.; CUI, Y.; YUAN, W.; HAN, T. X.; CAIRE, G. On the fundamental tradeoff of integrated sensing and communications under gaussian channels. **IEEE Transactions on Information Theory**, v. 69, n. 9, p. 5723–5751, 2023.

YAN, X.; AN, X.; YE, W.; ZHAO, M.; XI, Y.; WU, J. User-centric network architecture design for 6g mobile communication systems. In: **2023 Joint European Conference on Networks and Communications 6G Summit (EuCNC/6G Summit)**. [S.l.: s.n.], 2023. p. 305–310.

YEN, J. Array signal processing. Prentice-Hall, Inc., Englewood Cliffs, NJ, 1985.

YIN, M.; IANNELLI, A.; SMITH, R. S. Maximum likelihood estimation in data-driven modeling and control. **IEEE Transactions on Automatic Control**, v. 68, n. 1, p. 317–328, 2023.

ZHANG, J.; CHEN, S.; LIN, Y.; ZHENG, J.; AI, B.; HANZO, L. Cell-free massive MIMO: A new next-generation paradigm. **IEEE Access**, v. 7, p. 99878–99888, 2019.

ZHANG, J. A.; RAHMAN, M. L.; WU, K.; HUANG, X.; GUO, Y. J.; CHEN, S.; YUAN, J. Enabling joint communication and radar sensing in mobile networks—a survey. **IEEE Communications Surveys Tutorials**, v. 24, n. 1, p. 306–345, 2022.

ZHANG, J. A.; RAHMAN, M. L.; WU, K.; HUANG, X.; GUO, Y. J.; CHEN, S.; YUAN, J. Enabling joint communication and radar sensing in mobile networks—a survey. **IEEE Communications Surveys & Tutorials**, v. 24, n. 1, p. 306–345, 2022.

ZHANG, J. A.; WU, K.; HUANG, X.; GUO, Y. J. Beam alignment for analog arrays based on Gaussian approximation. **IEEE Transactions on Vehicular Technology**, v. 72, n. 6, p. 8152–8157, 2023.

Appendix A – PROOF OF PROPOSITION 3.3.1

As previously mentioned, the observation vector described in (3.3) is a Gaussian random vector. Keeping this fact in mind, we may refer to (KAY, 1993), where the author presents a closed-form equation to calculate the entries of the FIM for non-zero mean Gaussian signals, in which given an observation vector $\mathbf{y}$ and a set of deterministic unknown parameters ξ, the matrix entries are calculated as follows,

$$[\mathbf{I}(\xi)]_{i,j} = \text{tr}\left[\mathbf{C}_\mathbf{y}^{-1}\frac{\partial \mathbf{C}_\mathbf{y}}{\partial \xi_i}\mathbf{C}_\mathbf{y}^{-1}\frac{\partial \mathbf{C}_\mathbf{y}}{\partial \xi_j}\right] + 2Re\left[\frac{\partial \mu_\mathbf{y}^H}{\partial \xi_i}\mathbf{C}_\mathbf{y}^{-1}\frac{\partial \mu_\mathbf{y}}{\partial \xi_j}\right]. \tag{A.1}$$

Moreover, if the covariance matrix of the observation vector does not depend on the set of unknown parameters, (A.1) is therefore reduced to

$$[\mathbf{I}(\xi)]_{i,j} = 2Re\left[\frac{\partial \mu_\mathbf{y}^H}{\partial \xi_i}\sigma_z^{-2}\mathbf{I}_{NM_R}\frac{\partial \mu_\mathbf{y}}{\partial \xi_j}\right]. \tag{A.2}$$

In this work, we assume that the unknown parameters are $\xi = \begin{bmatrix} f_{D,0} & \theta_0 \end{bmatrix}$. Furthermore, we have that $\mu_\mathbf{y} = \mu_0$ and $\mathbf{C}_\mathbf{y} = \sigma_z^2\mathbf{I}_{NM_R}$. Therefore, it follows that,

$$\frac{\partial [\mu_y]_i}{\partial f_{D,0}} = j2\pi n T_s [\mu_0]_i, \tag{A.3}$$

$$\frac{\partial [\mu_y]_i}{\partial \theta_0} = j\pi p \cos\theta_0 [\mu_0]_i, \tag{A.4}$$

for $i = 1, \ldots, NM_R$. Thus, by substituting (A.3) in (A.1)

$$[\mathbf{I}(\xi)]_{f_{D,0},f_{D,0}} = 2(2\pi T_s)^2 \sum_{n=0}^{N-1} n^2 \frac{\|\mu_0[n]\|^2}{\sigma_z^2},$$

$$[\mathbf{I}(\xi)]_{f_{D,0},\theta_0} = \frac{(2\pi)^2 T_s \cos\theta_0}{2}(M_R - 1)\sum_{n=0}^{N-1} n \frac{\|\mu_0[n]\|^2}{\sigma_z^2},$$

$$[\mathbf{I}(\xi)]_{\theta_0,\theta_0} = \frac{(\pi\cos\theta_0)^2(2M_R-1)(M_R-1)}{3}\sum_{n=0}^{N-1}\frac{\|\mu_0[n]\|^2}{\sigma_z^2}.$$

We have used the fact that $\|\mu_0[n]\|^2 = M_R|\alpha_0 \mathbf{a}_T^T \mathbf{s}[n]|^2$. Once we have calculated the FIM, the CRLB is given by the inverse of this matrix.

Appendix B – PROOF OF PROPOSITION 3.3.2

We refer to (A.1) to calculate the FIM since the observation vector regarding the multistatic architecture is a non-zero mean Complex Gaussian random vector. It should be noted that the covariance matrix of the observation vector does not depend on the set of unknown parameters $\begin{bmatrix} f_{D,r} & \theta_r \end{bmatrix}$. Thus, (A.1) is reduced to (A.2), similar to what was observed for the bistatic architecture.

Regarding the considered architecture, we have that $\mu_y = \mu$ and $\mathbf{C_y} = \sigma_z^2 \mathbf{I}_{KNM_R}$.

Moreover, the key idea here is to consider the parameters concerning each Rx AP in their respective local coordinate system as a function of the reference set of parameters, as described in (3.8). Thus, it follows that

$$\begin{aligned} \frac{\partial [\mu_{\mathbf{y}}]_i}{\partial f_{D,r}} &= j2\pi n T_s [\mu_r]_i, \\ \frac{\partial [\mu_y]_i}{\partial \theta_r} &= j\pi p \cos\theta_k [\mu_y]_i, \end{aligned} \tag{B.1}$$

for $i = r, \ldots, KNM_R$. Thus, by substituting (B.1) in (A.2) it follows that,

$$[\mathbf{I}(\xi)]_{f_{D,r},f_{D,r}} = 2(2\pi T_s)^2 \sum_{k=r}^{K-1} \sum_{n=r}^{N-1} n^2 \frac{\|\mu_k[n]\|^2}{\sigma_z^2},$$

$$[\mathbf{I}(\xi)]_{f_{D,r},\theta_r} = \frac{(2\pi)^2 T_s}{2} (M_R - 1) \sum_{k=r}^{K-1} \cos\theta_k \sum_{n=r}^{N-1} n \frac{\|\mu_k[n]\|^2}{\sigma_z^2},$$

$$[\mathbf{I}(\xi)]_{\theta_r,\theta_r} = \frac{\pi^2 (2M_R - 1)(M_R - 1)}{3} \sum_{k=r}^{K-1} \cos^2\theta_k \sum_{n=r}^{N-1} \frac{\|\mu_k[n]\|^2}{\sigma_z^2}.$$

where, $\|\mu_k[n]\|^2 = M_R |\alpha_k \mathbf{a}_T^T \mathbf{s}[n]|^2$. Thus, once we have found the FIM for the set of unknown parameters, we may calculate the CRLB by calculating the inverse of this matrix.

Appendix C – PROOF OF THE CONVEXITY OF (4.16)

To prove the convexity of the constraint described in (4.16), it is necessary to show that the Hessian matrix of the function $\text{tr}\{\mathbf{F}^{-1}\}$ is positive semidefinite. To this end, we exploit the following derivative identities:

$$\begin{aligned}\frac{\partial \text{tr}\{\mathbf{A}\}}{\partial t} &= \text{tr}\left\{\frac{\partial \mathbf{A}}{\partial t}\right\},\\ \frac{\partial \mathbf{A}^{-1}}{\partial t} &= -\text{tr}\left\{\mathbf{A}^{-1}\frac{\partial \text{tr}\{\mathbf{A}\}}{\partial t}\mathbf{A}^{-1}\right\},\end{aligned} \tag{C.1}$$

where $\mathbf{A}$ is an invertible square matrix, which is a function of t. Therefore, differentiating $\text{tr}\{\mathbf{F}^{-1}\}$ with respect to $T_{s,i}$,

$$\begin{aligned}\frac{\partial \text{tr}\{\mathbf{F}^{-1}\}}{\partial T_{s,i}} &= \text{tr}\left\{\frac{\partial \text{tr}\{\mathbf{F}^{-1}\}}{\partial T_{s,i}}\right\}\\ &= -\text{tr}\left\{\mathbf{F}^{-1}\mathbf{F}_i\mathbf{F}^{-1}\right\}.\end{aligned} \tag{C.2}$$

As a consequence, to calculate the (i,j)-th element of the Hessian matrix of $\text{tr}\{\mathbf{F}^{-1}\}$, we further take the derivative of (C.2) with respect to $T_{s,j}$ as follows:

$$\begin{aligned}[\nabla^2\text{tr}\{\mathbf{F}^{-1}\}]_{i,j} = \frac{\partial^2\text{tr}\{\mathbf{F}^{-1}\}}{\partial T_{s,j}\partial T_{s,i}} &= -\frac{\partial}{\partial T_{s,i}}\left(\text{tr}\left\{\mathbf{F}^{-1}\mathbf{F}_i\mathbf{F}^{-1}\right\}\right)\\ &= -\text{tr}\left\{\frac{\partial}{\partial T_{s,i}}\left(\mathbf{F}^{-1}\mathbf{F}_i\mathbf{F}^{-1}\right)\right\}\\ &= -\text{tr}\left\{-\mathbf{F}^{-1}\mathbf{F}_j\mathbf{F}^{-1}\mathbf{F}_i\mathbf{F}^{-1}-\mathbf{F}^{-1}\mathbf{F}_i\mathbf{F}^{-1}\mathbf{F}_j\mathbf{F}^{-1}\right\}\\ &= \text{tr}\left\{\mathbf{F}^{-1}\mathbf{F}_j\mathbf{F}^{-1}\mathbf{F}_i\mathbf{F}^{-1}\right\}+\text{tr}\left\{\mathbf{F}^{-1}\mathbf{F}_i\mathbf{F}^{-1}\mathbf{F}_j\mathbf{F}^{-1}\right\}\\ &= 2\text{tr}\left\{\mathbf{F}^{-1}\mathbf{F}_i\mathbf{F}^{-1}\mathbf{F}_j\mathbf{F}^{-1}\right\}.\end{aligned} \tag{C.3}$$

To demonstrate that the Hessian matrix is positive semidefinite, consider an arbitrary vector $\mathbf{u}$, such that

$$\begin{aligned}\mathbf{u}^T\nabla^2\text{tr}\{\mathbf{F}^{-1}\}\mathbf{u} &= \sum_{i=1}^{L}\sum_{j=1}^{L}u_iu_j2\text{tr}\left\{\mathbf{F}^{-1}\mathbf{F}_i\mathbf{F}^{-1}\mathbf{F}_j\mathbf{F}^{-1}\right\}\\ &= 2\text{tr}\left\{\mathbf{F}^{-1}\left(\sum_{i=1}^{L}u_i\mathbf{F}_i\right)\mathbf{F}^{-1}\left(\sum_{j=1}^{L}u_j\mathbf{F}_j\right)\mathbf{F}^{-1}\right\}.\end{aligned} \tag{C.4}$$

Therefore, since the FIM is positive semidefinite , it is possible to define $\mathbf{B} \triangleq \mathbf{F}^{-\frac{1}{2}}\left(\sum_{i=1}^{L}u_i\mathbf{F}_i\right)\mathbf{F}^{-\frac{1}{2}}$, such that

$$\mathbf{u}^T\nabla^2\text{tr}\{\mathbf{F}^{-1}\}\mathbf{u} = 2\text{tr}\left\{\mathbf{F}^{-\frac{1}{2}}\mathbf{B}^2\mathbf{F}^{-\frac{1}{2}}\right\} = 2\text{tr}\left\{\mathbf{B}^2\mathbf{F}^{-1}\right\}. \tag{C.5}$$

Moreover, since all of the $\mathbf{F}_l$ matrices are Hermitian, $\mathbf{B}^2$ is Hermitian, and consequently semidefinite positive as well. Thus,

$$\begin{aligned} \mathbf{u}^T \nabla^2 \mathrm{tr}\{\mathbf{F}^{-1}\}\mathbf{u} &= \mathrm{tr}\left\{\mathbf{B}^2\mathbf{F}^{-1}\right\} \geq 0, \\ \nabla^2 &\succeq \mathrm{tr}\{\mathbf{F}^{-1}\}, \end{aligned} \tag{C.6}$$

which implies that $\mathrm{tr}\{\mathbf{F}^{-1}\}$ is convex in the domain of $\mathbf{F}$.